Master Thesis

Lowering the IceCube Detection Threshold by Wavelength-shifting Optical Modules

Author:
Simon De Rijck

Promotor:
Prof. Dr. Dirk Ryckbosch

Thesis ingediend tot het behalen van de academische graad van Master in de Fysica en Sterrenkunde

in the

IceCube Group
Department of Physics and Astronomy

June 2013

"Detectors can be classified into three categories - those that don't work, those that break down, and those that get lost."

Anonymous

Acknowledgements

Thank God it is over! But mostly, I would like to thank my promoter, Prof. Dr. Dirk Ryckbosch, for giving me the opportunity to start an experiment from scratch. I very much appreciate the freedom I was given, making plenty of room for mistakes, but more importantly allowing me to learn from those mistakes. I would also like to thank Mathieu Labare, Matthias Vraeghe, Sam De Ridder, and the other people of the Ghent IceCube group for the numerous interesting discussions we had, for reading parts of my thesis, and simply for tolerating my presence in their offices[1]. A special thanks goes to the people from the Physikalisches Institut der Universität Bonn, for lending us the wavelength shifter. A second thank you to Matthias and Sam for giving me a ride to Bonn to pick up that same wavelength shifter. I also want to thank Michael Tytgat and Simon Cauwenbergh for helping me out with choosing and programming the readout modules of my setup.

I would also like to thank my two fellow master students of the first floor, Sander and Isabelle, who helped me out when needed and made my time here at the INW a lot more fun! Not to forget my fellow master students of the second floor, who made the late nights at the INW a lot more bearable. Most importantly, I want to thank all my friends from Nerdwana, who made the past five years unforgettable!

Finally, I would like to thank my parents, brother, and girlfriend who supported me through thick and thin, albeit mostly from a distance (respectively 30 km, everything from 30 km up to 12,000 km depending on where he is working, and 5279 miles).

[1] Adding a footnote in the acknowledgement: mission accomplished.

Contents

List of Figures

List of Tables

Introduction

Neutrinos are undoubtedly the most elusive of all the known elementary particles. Although they are present in large numbers in the Universe, with hundreds of trillions of them crossing the Earth every single second, it is very difficult to catch one of them. This is because neutrinos are nearly massless and electrically neutral elementary particles which only interact very weakly with matter. Although they were discovered more than half a century ago, it is still not known whether neutrinos are their own antiparticles or not and what their masses are. However, because of their intrinsic properties neutrinos appear to be a useful tool to probe the Universe for interesting physics.

The past few decades a new field in astrophysics emerged, called neutrino astrophysics, in which neutrinos rather than photons are used to study the Universe. Because of their aforementioned properties, neutrinos propagate virtually unhindered through the cores of their astrophysical sources and through the Universe. The challenge is then to detect these neutrinos on Earth, with so-called neutrino telescopes.

The IceCube Neutrino Observatory is a giant neutrino telescope embedded in the Antarctic ice at the geographical South Pole, detecting atmospheric and extraterrestrial neutrinos, with energies from 10 GeV to several PeV, through the Cherenkov effect. When a neutrino interacts with a nucleon in the ice, the charged leptonic partner of this neutrino is produced, carrying a large fraction of the original neutrino energy and travelling in almost the same direction as the initial neutrino. When these leptons travel faster than the speed of light in ice, they cause the medium to emit UV/blue light in a typical cone wave front, the Cherenkov cone. These Cherenkov photons are detected by optical sensors called Digital Optical Modules, mounted on strings in a one cubic kilometer grid structure in the ice.

An upgrade for the IceCube detector is proposed to lower the energy threshold down to a few GeV. New concepts for optical sensors are being investigated as part of the R&D for PINGU and possible future upgrades of the IceCube detector. The goal of this master thesis research was to start up a working experimental setup to test the feasibility of using wavelength shifting materials as the active part of a Cherenkov detector.

In Chapter 1 of this thesis report, an extensive introduction on the neutrino is given, both from the perspective of particle physics and astroparticle physics. Chapter 1 also introduces the concept of neutrino detection through the Cherenkov effect. The IceCube Neutrino Observatory is discussed in Chapter 2. Chapter 3 describes the experimental setup designed and constructed for this thesis. The physics happening inside the different parts of the detector, such as the relevant properties of a wavelength shifter, are explained. A Monte Carlo simulation of the detection principle is described in Chapter 4. The results of the measurements are shown in Chapter 5. Finally, Chapter 6 summarizes the current status of the research and provides an outlook.

Chapter 1

Neutrinos

In the first section of this introductory chapter neutrinos are discussed from the viewpoint of particle physics. Subsections 1.1.1 to 1.1.3 deal with the Standard Model of particle physics (SM) and the physics beyond this model. The role of the neutrino in and beyond this model is discussed separately in Section 1.1.4, where we look at the phenomena of neutrinoless double beta decay ($0\nu\beta\beta$) and neutrino oscillations. Section 1.2 and Section 1.3 address neutrinos as cosmological messengers and how they can be detected. This provides the basic information needed to discuss the IceCube Neutrino Observatory in Chapter 2.

1.1 Neutrinos in particle physics

Neutrinos are nearly massless and electrically neutral elementary particles which only interact through the weak interaction (WI). Although neutrinos were discovered more than half a century ago, it is still not known whether they are their own antiparticles or not and what their masses are. In this section, the characteristics of the neutrino, both in the Standard Model and beyond, are described.

1.1.1 Particle physics: a historic overview

It is hard to imagine now how the physics community in the early 1900s believed they were close to a complete understanding of the laws of nature, knowing that they had only discovered one elementary particle at that time, the electron[1].

[1] Discovered in 1987 by J.J. Thomson [1].

In 1905, Albert Einstein published four papers which had a major influence on modern physics, including the field of particle physics. In his paper on the photoelectric effect [2], he proposed the idea of energy quanta, building further on the theoretical findings of Max Planck on black body radiation. The concept of light quantization contradicts the wave theory of light which follows the well-established Maxwell equations. These light quanta were baptized photons in 1926, and the consequent particle-wave duality lies at the heart of quantum mechanics. Einstein also proposed a stochastic model on the Brownian motion[2] [3], giving extra support to the idea of atoms being real physical objects, which was still under debate in the beginning of the 20$^{\text{th}}$ century. In his two other papers written that same year, Einstein introduced special relativity [4] and the mass-energy equivalence [5]. It is the combination of the principles of quantum mechanics and special relativity, quantum field theory, which is the language of present day particle physics theories.

The history of elementary particle physics can be divided in four major periods [6], starting with "the birth of modern particle physics" in the 1930s and 1940s, followed by the period of "particle explosion" in the 1950s and 1960s, and "the rise of the Standard Model" from the mid '60s until 1979, to a period of "normal science"[3] from the '80s on. The road to the SM was long and bumpy, but serves as a great example of the importance of a continuous interplay between experiment and theory.

In 1911 Lise Meitner and Otto Hahn found that the energy spectrum of the electrons emitted by beta (β) decay was continuous rather than discrete, implying a non-conservation of energy[4]. In a desperate attempt to save the conservation laws of energy, momentum, and angular momentum in β decays, Wolfgang Pauli postulated in 1930 the existence of a new electrically neutral, spin $\frac{1}{2}$, and nearly massless particle which interacts very weakly (hence why it was not observed) in order to explain the continuous energy spectrum [10]. Enrico Fermi was the first to successfully describe the β decay theoretically in 1934 [11], assuming the existence of this new particle, which he baptized the neutrino. Because neutrinos interact so weakly, it was not until 1956 that they were discovered by Fred Reines and Clyde Cowan [12]. They detected electron antineutrinos ($\bar{\nu}_e$) coming from a nuclear reactor.

In 1933 Carl David Anderson discovered the positron, the antiparticle of the electron, by examining cosmic rays (see also Section 1.2.2.1) [13]. Its existence was predicted by

[2] The random movement of particles in a liquid or gas due to consecutive collisions with fast-moving atoms or molecules in that same liquid or gas.

[3] As coined by Thomas Kuhn in *The Structure of Scientific Revolutions*, referring to a period where the focus of particle physics was to test the predictive power of the Standard Model.

[4] At that time the nuclear beta decay was modelled as: $(A, Z) \rightarrow (A, Z+1) + e^-$, where Z (A) is the atomic number (mass number) of the decaying nucleus. Note that the atomic nucleus was discovered that same year and that the proton and neutron were only discovered in 1919 and 1932 respectively [7–9].

Paul Dirac one year earlier[5] and Anderson's discovery was a great triumph for the developing discipline of quantum mechanics. Further studies of cosmic rays[6] led in 1937 to the discovery of the muon [16], a heavy brother of the electron, and to the discovery of the pion [17] and kaon [18] in 1947[7]. Especially the discovery of the muon was surprising to many physicists, as it had no evident role in the structure of matter[8]. Also the pion and kaon were a bit special, since they were the first known strongly interacting particles (hadrons) aside from the nucleons.

Passing the GeV energy barrier with particle accelerators and with the arrival of more sensitive visual detectors such as the high-pressure diffusion cloud chamber [19] and the bubble chamber [20], the '50s and '60s revealed the existence of many new particles. Following the spectacular success of quantum electrodynamics (QED) in the early 1950s, big steps forward were taken in the theories on the strong and weak interactions.

With the discovery of many new hadrons such as the delta (Δ) and sigma (Σ) particle, the list of particles rapidly increased and the search for an underlying structure was at full speed. Up to then, all particles were still believed to be elementary, but this idea gradually changed over the following years. In 1955, the first experimental hint for a proton substructure was given by Robert Hofstadter, using electron-proton scattering [21]. In 1961, Murray Gell-Mann and Yuval Ne'eman classified the known strongly interacting particles (baryons and mesons separately) in a scheme based on the mathematical symmetry group SU(3) [22, 23]. Their scheme required the existence of another particle, the omega minus baryon Ω^-, which was discovered in 1964 [24]. In the meanwhile, Gell-Mann and George Zweig explained the quantum numbers of these hadrons in terms of quarks (up, down, and strange quark), massive spin $\frac{1}{2}$ particles with fractional electric charge [25, 26]. Originally introduced as a mathematical concept to create order in the hadron zoo, deep inelastic electron-proton scattering experiments at the Stanford Linear Accelerator Center (SLAC) showed in 1969 that quarks are real physical entities [27, 28]. Hadrons are made of (valence) quarks and thus do not appear to be elementary. Mesons are composed of a quark and an antiquark, while baryons consist of three quarks. More specifically, the proton (neutron) is made up by two (one)

[5] In 1928, Dirac introduced the Dirac equation allowing electrons to have both positive and negative energy solutions [14]. However, he did not explicitly predict the existence of an antielectron yet. For most other particles the antiparticle was discovered almost simultaneously with the particle itself. The proton is another exception, for which the antiproton was only discovered in 1955 [15].

[6] Particle accelerators did not reach high enough energies yet, so cosmic rays were the only source of high-energy subatomic particles at that point. Cosmic rays are discussed in Section 1.2.2.1.

[7] The pion's existence was predicted by Hideki Yukawa in 1935 in his model of the strong nuclear force, where they play a role as force carriers.

[8] And it still does not. Although three lepton families are required to explain CP violation in the lepton sector, this does not explain the reason of existence of the muon (or the tau lepton).

up quarks and one (two) down quark[9]. In 1964, an additional quark quantum number, color charge, was introduced to achieve an antisymmetric wavefunction (required by the Pauli principle) for the Ω^- and Δ^{++} hadrons [29]. The foundation of quantum chromodynamics (QCD) was laid.

During that same period, the theory of the weak interaction slowly evolved into what it is right now. Although the Fermi theory of the weak interaction reproduced the available experimental data at low energies rather well, it runs into trouble at higher energies, predicting an ever increasing cross section. In 1957, Julian Schwinger and others took the first step to solving this problem by including an intermediate vector boson (IVB) to the story [30]. The β decay is assumed to be mediated by a massive W boson[10]. In 1957, C.S. Wu and her colleagues found a clear violation of parity conservation in the β decay of cobalt-60 [31, 32], showing that the weak interaction is not a pure vector interaction, but involves an axial vector part too. In 1962, a team of physicists including Leon Lederman, verified at the Alternating Gradient Synchrotron (AGS) in Brookhaven that the neutrinos accompanying muons are distinct from those accompanying electrons, as inferred earlier from theoretical considerations [33]. The leptons could then be organized in two families, the electron and electron neutrino being the first one, and the muon and muon neutrino the second one. In 1963, Nicola Cabibbo introduced the Cabibbo angle to preserve the universality of the weak interaction[11]. The Cabibbo angle is related to the relative probability that down and strange quarks decay into up quarks and it was the first hint towards mixing in the quark sector [34].

The attempts towards a theory for the weak interaction eventually culminated in a unification of the electromagnetic and weak interaction, proposed by Sheldon Glashow, Steven Weinberg, and Abdus Salam in the late 1960s [35–37]. Apart from the already introduced W bosons $W^{\pm}$, the unified theory also included a new intermediate vector boson, the neutral Z boson. These bosons are described by an $SU(2)_W \times U(1)_Y$ gauge theory, where this symmetry is spontaneously broken down to the $U(1)_{EM}$ symmetry by the Higgs mechanism, independently proposed in 1964 by Robert Brout and Francois Englert, Peter Higgs, and Gerald Guralnik, C. R. Hagen, and Tom Kibble [38–40]. This symmetry breaking is necessary in order to give the weak vector bosons a mass (as inferred from experiments), while keeping the electromagnetic vector boson (the photon) massless (as known from experiments).

[9] Note that it was not until the end of the '70s that the consensus was reached that hadrons are composed of quarks, held together by the strong interaction through gluon exchange, rather than being elementary particles. The name gluon refers to its function of holding quarks inside a hadron, acting as a sort of glue.

[10] It needs to be massive to account for the short range of the weak interaction.

[11] The transitions between up and down quarks in particles and between lepton and lepton neutrino had similar amplitudes, suggesting a universal coupling in weak interactions. However, the coupling constant for strange quarks, e.g. in the beta decay of a Λ, turned out to be about four times smaller.

During the '70s, the SM[12] evolved into its final form. To account for the apparent suppression of the flavor-changing neutral currents (FCNC), and more specifically the strangeness-changing neutral currents[13], Sheldon Glashow, John Iliopoulos, and Luciano Maiani came up with the GIM mechanism in 1970 [35]. This mechanism requires the existence of a fourth quark, the charm quark, in order to have mixing between two quark families ((u,d) and (c,s)). An extra quark family, containing the top and bottom quark, was added by Makoto Kobayashi and Toshihide Maskawa in 1973 to explain the CP (Charge conjugation and Parity) violation in weak interactions [41], observed by James Cronin and Val Fitch in kaon decay in 1964 [42]. Meanwhile, David Gross, Frank Wilczek, and David Politzer discovered the phenomenon of asymptotic freedom in the strong interaction in 1973, restoring the faith in quantum field theory as the language of particle physics[14] [44, 45]. With the discovery of the charm quark in 1974, the tau lepton in 1975 (adding a third family to the lepton sector), the bottom quark in 1977, the gluon in 1978[15], the W and Z boson in 1983, the top quark in 1995, the tau neutrino in 2000, and very recently the detection of a Higgslike scalar boson[16] in 2012 at the Large Hadron Collider (LHC), the Standard Model has repeatedly proven its predictive strength and consistency [46–56].

Although the Standard Model has booked success after success, still numerous questions remain unanswered, suggesting that this model is only a low-energy limit of a more general theory.

Originally, neutrinos were included in the SM as massless particles (see also Section 1.1.4.1). In the late 1960s, the Homestake experiment in South Dakota was the first of many experiments to observe a systematically lower solar neutrino flux than expected from theoretical models of the solar interior. This was the beginning of the so-called solar neutrino problem, which is now ascribed to neutrino oscillations (see also Section 1.1.4.2 and 1.3.3). Neutrino oscillations imply non-zero masses for at least two of the three known neutrino flavors. The long-awaited proof for neutrino oscillations only came in 1998 (atmospheric muon neutrino deficit at SuperKamiokande [57]) and 2001 (solar electron neutrino deficit at Sudbury Neutrino Observatory [58]). The absolute values of these neutrino masses are not known yet and are currently being looked for. Knowing that neutrinos must have a mass, the question of whether these masses are

[12] The combination of the Electroweak theory and the Strong Interaction theory.

[13] These are interactions that change the flavor of a fermion current without altering its electric charge.

[14] Up to then, it was thought that field theory failed to give a correct description because the interactions became infinitely strong at short distances. At larger distances the strong interaction is governed by the confinement principle, introduced by Kenneth Wilson in 1974 [43]. This implies that two quarks cannot be separated as the attractive force between them increases with distance. Hence why quarks are never observed as free particles.

[15] Observed indirectly as jets at the DESY accelerator.

[16] The particle associated with the Higgs field which gives mass to the weak gauge bosons and all other massive elementary particles.

Dirac masses (like all the other masses in the SM) or Majorana masses arises (see also Section 1.1.4.1).

Other problems of the SM include the fact that thus far one has not been able to write down a quantum field theory for the gravitational interaction that can be incorporated in the SM. Furthermore, the Higgs mechanism gives rise to the hierarchy problem[17]. The SM also does not provide any explanation on why there is more matter than antimatter in the Universe (baryon excess problem), nor can it account for all the (expected) dark matter in the Universe. These and other problems are currently being looked at both theoretically and experimentally, and it is not unlikely that we are at the verge of a new particle physics era, a "beyond the Standard Model" period.

1.1.2 The Standard Model of particle physics

The SM is the most successful attempt so far to describe the properties of elementary particles and their interactions. All known matter in the Universe can be decomposed in terms of the 24 elementary particles, the quarks and leptons (listed in Table 1.1 together with their antiparticles), and the three fundamental interactions between them[18], which are mediated by so-called gauge bosons (also listed in Table 1.1) [59].

Particle properties

Every elementary particle is described by a unique set of quantum numbers[19]:

– The electric charge quantum number Q is the charge of QED and determines how a particle couples to an electromagnetic field. The electric charge q is quantized and comes in integer multiples of the elementary charge $e = 1.602 \times 10^{-19} C$, so $q = Qe$. Leptons have charge multiples -1, 0, or $+1$, while quarks have charge multiples $-2/3$, $-1/3$, $+1/3$, or $+2/3$[20]. Q is a conserved quantity in all four fundamental interactions, meaning that in a certain interaction between particles the total charge of the initial particles equals the total charge of the final particles.

[17] Due to radiative corrections, the Higgs mass blows up in the SM, in conflict with the observed Higgs mass of about 125 GeV/c^2. This can be avoided by introducing supersymmetric partners for the SM particles, which is the starting point for supersymmetry theories.

[18] The gravitational interaction (GI) is not incorporated in the SM. At extremely high energies, near the Planck scale, quantum gravitation will play a role and a gravitational quantum field theory is necessary at these scales.

[19] Note that the mass of a particle is not a quantum number in the SM. It is put in the model by hand, i.e. from measurements.

[20] Such that hadrons also have an integer electric charge number.

– The color charge is the charge of QCD and determines how quarks interact with gluons and other quarks. Three different color charges exist, namely red, green and blue. Quarks carry one color, antiquarks carry one anticolor, and gluons carry a combination of a color and an anticolor. All hadrons have no overall color, and are said to be white[21]. Color charge is conserved in all four fundamental interactions.

– The strong isospin I is a quantum number related to the strong interaction and was initially introduced because up and down quarks are identical particles, apart from a different electric charge and a slightly different mass. The isospin projection I_3 for a certain particle is given by $I_3 = 1/2 \times [(n_u - n_{\bar{u}}) - (n_d - n_{\bar{d}})]$, where n_u is the number of up valence quarks, n_d is the number of down valence quarks, etc. I is conserved in the strong interactions. I_3 is not conserved in the charged weak interaction.

– The weak isospin T is a quantum number related to the weak interaction. It is similar to the strong isospin concept. The third component T_3 is conserved in all four fundamental interactions.

– The spin S is the intrinsic angular momentum of a particle. It is similar to the orbital angular momentum L of a particle, which is the quantum mechanical counterpart of the angular momentum $\bar{L} = m\bar{r} \times \bar{p}$. It was originally introduced to explain the observed angular momentum of particles that could not be accounted for by rotational angular momentum alone [60]. The total angular momentum $\bar{J} = \bar{L} + \bar{S}$ is a conserved quantity in all four fundamental interactions.

– P is the intrinsic parity of a particle. The parity operator acts as a mirror in configuration space. Parity is conserved in the electromagnetic and strong interaction, but not in the weak interaction. This parity violation implies that charged weak currents only couple to left-handed fermions and right-handed antifermions[22]. Because the photon has a negative intrinsic parity ($\bar{E} \mapsto -\bar{E}$ under P[23]), electron-positron annihilation implies that the electron and positron have opposite parity. By convention the electron, and more generally all the fermions, have $P = +1$. Antifermions have $P = -1$. Bosons and antibosons have the same parity.

– C is the charge conjugation quantum number which is related to the charge conjugation operator that mirrors in charge space, and thus converts particles in antiparticles and the other way around. C is only defined for particles which are

[21] Similar to the case of light where red, green, and blue together form white light. e.g. each valence quark of a proton carries one of the three color charges in such a way that the proton is white.

[22] Handedness or chirality is related to the more easy-interpretable concept of helicity. The helicity of a particle is defined as the sign of the projection of its spin onto its momentum vector.

[23] In one dimension: $F = m\frac{d^2x}{dt^2}$ and $F = qE$. Knowing that x changes under parity operation, while q, m, and t do not, one can deduce that E is mapped onto $-E$ by the parity operator.

their own antiparticles, such as the photon, the gluons, and the π^0. It is conserved in the electromagnetic and strong interaction, but not in the weak interaction. The combined CP parity is conserved in almost all weak interactions.

– L is the lepton number of a particle. It is $+1$ (-1) for a (anti)lepton, and 0 for non-leptonic particles. Every lepton family also has its own lepton flavor number, e.g. the electron lepton number L_e for the first lepton generation. The total lepton number is thought to be conserved in all interactions, while the flavor lepton numbers are not conserved in the weak interaction due to neutrino oscillations.

– B is the baryonic counterpart of the lepton number. Baryons have $B = +1$, antibaryons $B = -1$, and all other particles have $B = 0$. Since baryons are made up of three valence quarks, quarks are assigned $B = +1/3$. The different quark flavors also have a corresponding flavor quantum number, such as strangeness S for the strange quark and topness T for the top quark. These are not included in Table 1.1. By convention, the strange quark has $S = -1$, while the strange antiquark has $S = +1$. All the other quarks have $S = 0$. Similar rules apply for the other quark flavor quantum numbers. In the SM, the baryon number is conserved in almost all interactions.

Particle interactions

The four known forces in nature are gravitation, the electromagnetic interaction, the weak interaction, and the strong interaction. Formally, these interactions are described by gauge theories, which are field theories in which the Lagrangian[24] is invariant under a continuous group of local transformations[25], the gauge transformations. These transformations together form a symmetry group, $U(1)$, $SU(2)$, and $SU(3)$ being the ones present in the Standard Model. Every group has its own algebra of group generators[26], and for each generator of a group a corresponding vector field, the gauge field, can be defined. These gauge fields are included in the Lagrangian expression of the field theory to ensure gauge invariance. Just like the quanta of a particle field are particles, the quanta of the gauge fields are the gauge bosons. These gauge bosons are the mediators of the corresponding interaction.

[24] The concept of Lagrangians originates from classical mechanics, where it is defined as the difference of kinetic and potential energy $L = T - V$ for a certain dynamical system.

[25] A local transformation is a transformation which depends on the coordinates of the space in which this transformation is performed. e.g. a local transformation of a field in configuration space depends on the position coordinates, and thus acts differently in every space point.

[26] This is either an abelian or a non-abelian algebra. In the end, the difference between both expresses itself in the gauge charge of the gauge bosons. Abelian gauge theories produce uncharged gauge bosons, while non-abelian gauge theories produce charged gauge bosons.

TABLE 1.1: Elementary particles in the Standard Model. The different quantum numbers are explained in the text. Only if a quantum number is different for the antiparticle than for the particle, this is explicitly shown.

Sector	Gen./Int.	Particle	M [MeV/c^2]	Quantum Numbers						
				Q	Color	I,I_3	T,T_3[a]	$J^{P,C}$	L	B
Leptons	1st gen.	e^- (e^+)	0.511	-1 (+1)	–	0,0	$\frac{1}{2}$,$-\frac{1}{2}$ ($+\frac{1}{2}$)	$\frac{1}{2}^{+1(-1),-}$	+1 (-1)	0
		ν_e ($\bar{\nu}_e$)	0[b]	0	–	0,0	$\frac{1}{2}$,$+\frac{1}{2}$ ($-\frac{1}{2}$)	$\frac{1}{2}^{+1(-1),-}$	+1 (-1)	0
	2nd gen.	μ^- (μ^+)	105.66	-1 (+1)	–	0,0	$\frac{1}{2}$,$-\frac{1}{2}$ ($+\frac{1}{2}$)	$\frac{1}{2}^{+1(-1),-}$	+1 (-1)	0
		ν_μ ($\bar{\nu_\mu}$)	0	0	–	0,0	$\frac{1}{2}$,$+\frac{1}{2}$ ($-\frac{1}{2}$)	$\frac{1}{2}^{+1(-1),-}$	+1 (-1)	0
	3rd gen.	τ^- (τ^+)	1776.82	-1 (+1)	–	0,0	$\frac{1}{2}$,$-\frac{1}{2}$ ($+\frac{1}{2}$)	$\frac{1}{2}^{+1(-1),-}$	+1 (-1)	0
		ν_τ ($\bar{\nu_\tau}$)	0	0	–	0,0	$\frac{1}{2}$,$+\frac{1}{2}$ ($-\frac{1}{2}$)	$\frac{1}{2}^{+1(-1),-}$	+1 (-1)	0
Quarks	1st gen.	u ($\bar{u}$)	2.3	$+\frac{2}{3}$ ($-\frac{2}{3}$)	r,g,b ($\bar{r}$, $\bar{g}$, $\bar{b}$)	$\frac{1}{2}$,$+\frac{1}{2}$ ($-\frac{1}{2}$)	$\frac{1}{2}$,$+\frac{1}{2}$ ($-\frac{1}{2}$)	$\frac{1}{2}^{+1(-1),-}$	0	$+\frac{1}{3}$,$-\frac{1}{3}$
		d ($\bar{d}$)	4.8	$-\frac{1}{3}$ ($+\frac{1}{3}$)	r,g,b ($\bar{r}$, $\bar{g}$, $\bar{b}$)	$\frac{1}{2}$,$-\frac{1}{2}$ ($+\frac{1}{2}$)	$\frac{1}{2}$,$-\frac{1}{2}$ ($+\frac{1}{2}$)	$\frac{1}{2}^{+1(-1),-}$	0	$+\frac{1}{3}$,$-\frac{1}{3}$
	2nd gen.	c ($\bar{c}$)	1275	$+\frac{2}{3}$ ($-\frac{2}{3}$)	r,g,b ($\bar{r}$, $\bar{g}$, $\bar{b}$)	$\frac{1}{2}$,$+\frac{1}{2}$ ($-\frac{1}{2}$)	$\frac{1}{2}$,$+\frac{1}{2}$ ($-\frac{1}{2}$)	$\frac{1}{2}^{+1(-1),-}$	0	$+\frac{1}{3}$,$-\frac{1}{3}$
		s ($\bar{s}$)	95	$-\frac{1}{3}$ ($+\frac{1}{3}$)	r,g,b ($\bar{r}$, $\bar{g}$, $\bar{b}$)	$\frac{1}{2}$,$-\frac{1}{2}$ ($+\frac{1}{2}$)	$\frac{1}{2}$,$-\frac{1}{2}$ ($+\frac{1}{2}$)	$\frac{1}{2}^{+1(-1),-}$	0	$+\frac{1}{3}$,$-\frac{1}{3}$
	3rd gen.	t ($\bar{t}$)	173.5×10^3	$+\frac{2}{3}$ ($-\frac{2}{3}$)	r,g,b ($\bar{r}$, $\bar{g}$, $\bar{b}$)	$\frac{1}{2}$,$+\frac{1}{2}$ ($-\frac{1}{2}$)	$\frac{1}{2}$,$+\frac{1}{2}$ ($-\frac{1}{2}$)	$\frac{1}{2}^{+1(-1),-}$	0	$+\frac{1}{3}$,$-\frac{1}{3}$
		b ($\bar{b}$)	≈ 4000	$-\frac{1}{3}$ ($+\frac{1}{3}$)	r,g,b ($\bar{r}$, $\bar{g}$, $\bar{b}$)	$\frac{1}{2}$,$-\frac{1}{2}$ ($+\frac{1}{2}$)	$\frac{1}{2}$,$-\frac{1}{2}$ ($+\frac{1}{2}$)	$\frac{1}{2}^{+1(-1),-}$	0	$+\frac{1}{3}$,$-\frac{1}{3}$
Gauge bosons	EMI	γ (γ)	0	0	–	0	0	$1^{-1,-1}$	0	0
	SI	g (g)	0	0	color octet[c]	0	0	$1^{-1,-}$	0	0
	WI	W^- (W^+)	80.385×10^3	-1(+1)	–	0	1,-1 (+1)	$1^{-,-}$	0	0
		Z (Z)	91.1876×10^3	0	–	0	0	$1^{-,-}$	0	0
Higgs boson	Higgs scalar	H	$\approx 125 \times 10^3$	0	–	0	0	1^{+1}	0	0

[a] The fermions in this table are left-handed particles, while the antifermions are right-handed, as they are organized in the electroweak theory. The massive (anti)particles have also a right(left)-handed component, but these are singlets and thus have $T = 0$.

[b] The masses of the Standard Model neutrinos are zero. See also Section 1.1.4.1.

[c] There are 8 independent gluon color states: $1/\sqrt{2}(r\bar{b}+b\bar{r})$, $1/\sqrt{2}(r\bar{g}+g\bar{r})$, $1/\sqrt{2}(b\bar{g}+g\bar{b})$, $1/\sqrt{2}(r\bar{b}+b\bar{r})$,$1/\sqrt{2}(r\bar{b}+b\bar{r})$, $1/\sqrt{2}(r\bar{r}-b\bar{b})$, $-i/\sqrt{2}(r\bar{b}-b\bar{r})$, $-i/\sqrt{2}(r\bar{g}-g\bar{r})$, $-i/\sqrt{2}(b\bar{g}-g\bar{b})$, $1/\sqrt{6}(r\bar{r}+g\bar{g}-2b\bar{b})$.

– **The electromagnetic interaction** is among other responsible for the binding of electrons around a nucleus in an atom. All particles with a non-zero electric charge undergo electromagnetic interactions. It is described by quantum electrodynamics, which is an abelian gauge theory with the symmetry group $U(1)$. QED has one gauge boson, the photon, which is massless, has spin 1, and carries no electric charge. Following the Heisenberg uncertainty relations, this zero mass implies an infinite range for the electromagnetic interaction. An example of the electromagnetic interaction is given in Figure 1.1(a).

– **The weak interaction** is the force responsible for processes like radioactive decay of subatomic particles, such as the β decay. All fermions interact weakly. It is mediated by three massive, spin 1 intermediate vector bosons, the W^+, W^-, and Z, explaining its short range ($< 10^{-3}$ fm). In terms of quantum field theory, the weak interaction is described by the $SU(2)$ symmetry. However, the weak vector bosons get their mass from spontaneous symmetry breaking of the unified electroweak interaction below the weak energy scale $v_{weak} = 246$ GeV. The electroweak interaction is described by a non-abelian gauge theory with the symmetry group $SU(2)_W \times U(1)_Y$. The Higgs mechanism breaks this group down to the $U(1)_{EM}$ group of QED, hereby leaving the photon massless and giving mass to the weak vector bosons. Note the difference between $U(1)_{EM}$ and $U(1)_Y$. The former has the electric charge Q as generator, while this is the weak hypercharge Y for the latter. Q and Y are related by the relation $Q = Y/2 + T_3$, with T_3 the third component of the weak isospin. The weak interactions, mediated by the W bosons, transform quark flavors into each other, as well as lepton flavors into each other. An example of the weak interaction is given in Figure 1.1(b).

– **The strong interaction** is what keeps quarks bound into hadrons, such as the nucleons. It is described by Quantum Chromodynamics. QCD is an abelian gauge theory with the symmetry group $SU(3)$ and thus has 8 gauge bosons, the gluons. Gluons are massless particles, carrying strong charge (colour), but no electric charge. Despite gluons being massless, the strong interaction is short-ranged (though much stronger than the weak interaction, hence its name) because gluons interact strongly among themselves. This manifests itself in two opposite phenomena, confinement and asymptotic freedom. The former implying that quarks cannot exist as free particles. At distances of the order of 1 fm (which is the size of a nucleon), the energy of the color field has increased sufficiently to create real quark-antiquark pairs. Asymptotic freedom means that quarks behave as almost independent particles at very short distances inside hadrons. An example of the strong interaction is given in Figure 1.1(c).

The Higgs mechanism

The Higgs mechanism in the SM is the process that gives mass to the elementary particles (including the weak gauge bosons). The Higgs field spontaneously breaks three of the four generators of the electroweak symmetry group, causing the weak vector bosons to be massive, while the photon stays massless. The quanta of the Higgs field, are Higgs bosons, massive scalar (spin 0) particles. The elementary fermions also acquire their mass through coupling to the Higgs field. A candidate for the SM Higgs boson was observed in 2012 at the LHC in Geneva. One of the observed interactions is displayed in Figure 1.1(d).

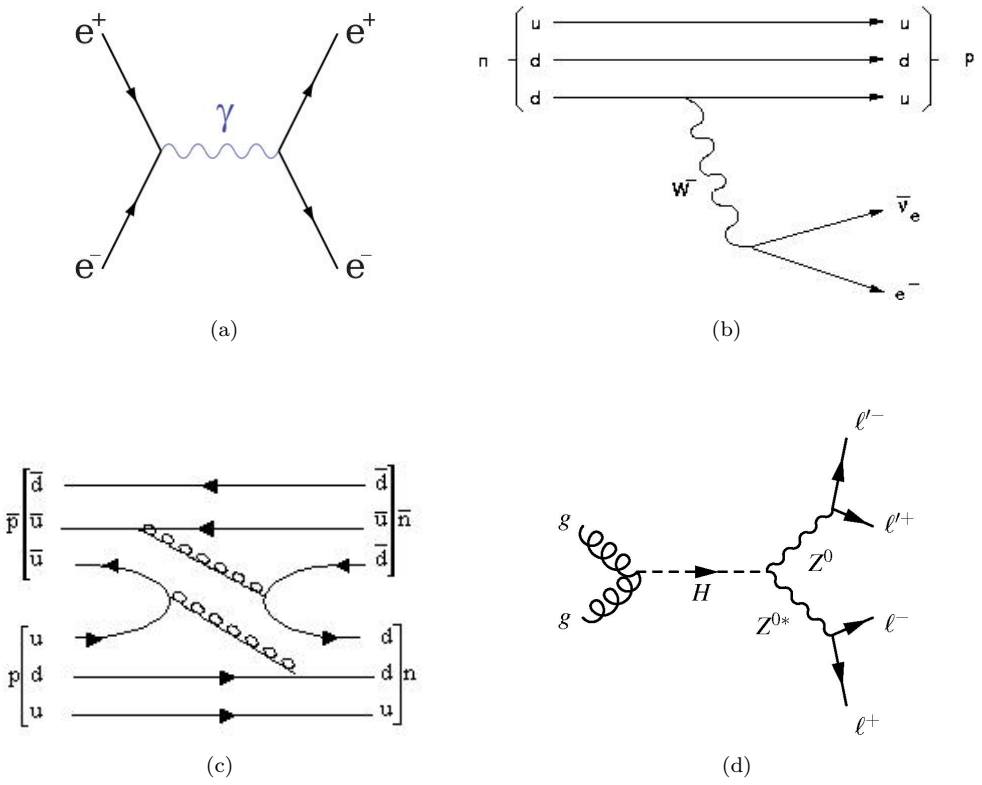

FIGURE 1.1: (a) Feynman diagram for electron-positron annihilation [61]. (b) Feynman diagram for β decay [62]. (c) Feynman diagram of a proton-antiproton collision producing a neutron and antineutron [63]. (d) Feynman diagram of a Higgs scalar boson decaying into four leptons [64].

1.1.3 Particle physics beyond the Standard Model

The ultimate goal of theoretical elementary particle physics is to find one theory unifying the four fundamental interactions, sometimes referred to as the Theory of Everything (TOE). As already mentioned in Section 1.1.1, it is clear that the Standard Model is not this TOE. Apart from 'physics' problems like the Higgs hierarchy problem, or the

inability to explain all the dark matter in the Universe, a lot of theoretical physicists also see an aesthetic problem with the SM. The SM contains 19 free parameters (including the masses of the leptons, quarks, and Higgs boson) and has three disconnected gauge symmetries, not really living up to the expectations of the average particle physics theorist. However, its success cannot be ignored and the SM is nowadays seen as the low-energy limit of a more general theory. Similar to how the electroweak theory breaks down into the electromagnetic theory and the weak theory, one expects this TOE to be a theory based on one big symmetry group which breaks down to the SM symmetry group at SM energy scales. Many candidates for such beyond the SM theories have been developed over the years, some more successful than others, but so far one has not yet found a theory addressing all the problems of the SM at a satisfactory level.

Two popular beyond the SM scenarios are the Grand Unified Theories (GUT) and Supersymmetry (SUSY) theories [59]. A Grand Unified Theory is a model in which the electromagnetic, weak, and strong interaction are unified at a high-energy scale (the so-called GUT scale). At high energies this GUT is described by one gauge symmetry. The one condition these models, and every beyond the SM model, must meet is that they need to reproduce the results of the SM at lower energies. A few candidates, such as a GUT based on the $SO(10)$ symmetry group, are promising. On of the difficulties accompanying GUT theories is that they involve new physics at this GUT scale, which is currently far from being in experimental reach for testing. Supersymmetry theories, such as the Minimal Supersymmetric Standard Model (MSSM), are more appealing because they predict new physics at the TeV energy scale. The hunt for supersymmetric particles is currently one of the main goals at the LHC. The idea of supersymmetry (adding bosonic/fermionic partners for all the SM fermions/bosons), combined with a GUT model has great potential, as it solves the Higgs hierarchy problem (as mentioned in Section 1.1.1) and also unifies the fundamental interactions (apart from gravitation) at higher energies.

1.1.4 Neutrino physics

In the following two subsections the focus is laid on the role of neutrinos in particle physics. Two phenomena are discussed, the neutrinoless double beta decay and neutrino oscillations [59], both of which are currently of very high interest in experimental particle physics.

1.1.4.1 Neutrinoless double beta decay

Up to now, it is still unknown whether neutrinos are their own antiparticles or not, or in other words whether they are Dirac particles or Majorana particles. If they are Dirac-like, neutrinos and antineutrinos are distinct particles with the same mass. A Majorana nature means that neutrinos and antineutrinos are the two helicity states of the same particle, i.e. Majorana neutrinos are their own antiparticles. Observation of neutrinoless double beta decay would imply Majorana nature.

Dirac vs. Majorana

It is important to stress the precise meaning of Majorana particles [65]. As seen earlier, the weak interaction does not conserve C parity, implying that C parity is not a useful concept to define Majorana particles. They can be defined by their transformation properties under CPT (where T stands for time reversal), which is presumably completely conserved. One can then say for a neutrino $|\nu(\bar{p}, h)\rangle$, where $\bar{p}$ is the neutrino momentum and h the neutrino helicity

$$CPT|\nu(\bar{p}, h)\rangle = \eta^h_{CPT}|\bar{\nu}(\bar{p}, -h)\rangle. \tag{1.1}$$

The helicity reversal is a consequence of the P operation, and the phase factor η^h_{CPT} is helicity dependent. We can now distinguish between Dirac and Majorana neutrinos:

- **Dirac neutrinos**: if the neutrino is not its own antiparticle, then the particle $\nu(\bar{p}, h)$ and the particle $\bar{\nu}(\bar{p}, h)$ interact differently with matter. In its rest frame, such a neutrino is described by a Dirac spinor, consisting of four independent states, namely the two spin states for both the neutrino and the antineutrino: $\nu_D(\bar{p}, \pm h)$, $\bar{\nu}_D(\bar{p}, \pm h)$.
- **Majorana neutrinos**: if the neutrino is its own antiparticle, then the particle $\nu(\bar{p}, h)$ and the particle $\bar{\nu}(\bar{p}, h)$ interact identically with matter. In its rest frame, such a neutrino is described by a Weyl spinor, consisting of only two independent states, namely its two spin states: $\nu_M(\bar{p}, \pm h) = \bar{\nu}_M(\bar{p}, \pm h)$.

All charged elementary fermions are by definition not their own antiparticles, and are thus described by Dirac spinors. If we look e.g. at a free electron, its dynamics is then described by the free Dirac Lagrangian

$$\mathcal{L}^D_{\text{free}} = \bar{\psi}(\partial\!\!\!/ - m^D_e)\psi, \tag{1.2}$$

where the second term is the mass term[27]. However, there is another possible mass term fulfilling the Lorentz invariance requirement for the Lagrangian, and including the kinetic energy term the alternative Lagrangian looks like

$$\mathcal{L}^{M}_{\text{free}} = \bar{\psi}\partial\!\!\!/\psi - \frac{1}{2}m_e^M \psi^T C^{-1}\psi, \tag{1.3}$$

where C is the matrix representation of the charge conjugation operator. Equation (1.3) is however not a valid Lagrangian for a free electron, or any other charged elementary fermion, as it is not invariant any more under the global $U(1)$ transformation $\psi \to e^{i\alpha}\psi$. Invariance under such a global phase transformation implies a conserved charge, e.g. electric charge Q. Knowing that Q is a conserved quantity, an electron cannot be described by the Lagrangian in Equation (1.3), also called the free Majorana Lagrangian. The Majorana mass term is thus only applicable to uncharged particles[28]. Furthermore, this Lagrangian describes fermions which are their own antiparticles (which cannot be the case for charged particles anyway, giving us a second reason why only Equation (1.2) works for the charged fermions). This follows from the fact that the Dirac mass term reduces itself to the Majorana mass term for self-charge conjugate particles, for which

$$\psi = \psi^c \equiv C\bar{\psi}^T. \tag{1.4}$$

Note that neutrinos are the only uncharged elementary fermions, so the "Dirac vs Majorana" question only applies to them[29].

Neutrino masses in and beyond the SM

It can be shown that neutrinos need to be massless in the SM[30]. In a Lagrangian theory for the elementary fermions, where fermions are left-handed and antifermions are right-handed particles and not assuming the SM symmetries such as charge and lepton number conservation yet, the most general mass term (put in by hand) is a Majorana term[31].

[27] That this is a mass term can be deduced from dimensional analysis. Knowing that the action $S = \int dtd^3x\mathcal{L}$ is dimensionless in natural units, one can infer that Lagrangians have a dimension of $[E]^4$, and Fermion fields have a dimension $[E]^{3/2}$. Also note that this mass term would explicitly break the gauge invariance of the SM, and thus cannot be added to the SM Lagrangian by hand. It only appears in the SM Lagrangian after symmetry breaking, i.e. through interaction with the Higgs field.

[28] Note that this charge is not limited to the electric charge, but can also be baryonic charge, leptonic charge, etc. Here we are dealing with fermions, so B does not matter, but L will not be a conserved quantity in a theory based on the Majorana Lagrangian.

[29] Note once more the problem with lepton number conservation. However, it is not even sure if lepton number is really a conserved quantum number.

[30] See Reference [59], pp. 227–231, for a beautiful and comprehensible derivation of this conclusion.

[31] This involves a Majorana mass matrix of the form $\begin{pmatrix} m_M & m_D \\ m_D & m_M \end{pmatrix}$ multiplied by a bilinear term (a Lorentz invariant term) involving the left and right-handed fermion fields. The subscripts M and D refer to Majorana and Dirac respectively. The off-diagonal elements are called m_D because these terms are the only one that survive in the SM, leading to the well-known Dirac mass terms.

Imposing the SM structure on this, using the SM doublets and assuming charge and lepton number conservation, the Majorana masses need to be put equal to zero for the charged fermions. This is not necessary for the uncharged fermions, namely the neutrinos (assuming that lepton number conservation is not strict). However, in order to generate these mass terms through the Higgs mechanism rather than putting them in by hand the Majorana bilinear needs to couple to a Higgs triplet. Knowing that the SM Higgs mechanism contains a Higgs doublet, Majorana neutrino masses cannot be generated. Adding an extra effective term to the Lagrangian[32] which can couple to the SM Higgs doublet is not an option as long as total lepton number conservation is a requirement.

In order to have massive neutrinos, the SM can be extended in two ways. The first way preserves total lepton number L and leads to Dirac masses for the neutrinos at the cost of adding right-handed neutrino singlets to the SM[33]. The second way assumes neutrino masses of both Dirac and Majorana type. It comes down to adding Majorana mass terms for the right-handed singlets of the first model to the Lagrangian. This goes at the cost of breaking total lepton number L, but has the beautiful consequence of providing a natural explanation for the fact that neutrinos appear to have much lighter masses than their charged leptonic partners (something that is not provided by the first model)[34]. It also addresses the baryon excess problem (the sphaleron mechanism [67]).

To go really beyond the SM, one can argue what the nature of neutrinos is in GUTs. In all GUT models, the elementary fermions, including the neutrinos, are placed in one big multiplet (because at high energies all the fundamental interactions are unified into one interaction, to which all the particles answer in the same way). Knowing that the charged leptons are massive, it would be very unlikely for a unifying theory that the neutrinos are not massive either. The question then remains (just like in the case of the two extensions of the SM discussed in the previous paragraph) why the neutrinos at SM energy scales have masses that are much smaller than the masses of the other particles. Again the most popular candidate in GUTs is the see-saw mechanism, which implies neutrinos to be Majorana particles, as we saw before. In conclusion, most GUTs include massive Majorana particles [65].

[32] The SM is only an effective theory, so adding non-renormalizable terms to the Lagrangian is actually not a problem. An explanation in laymen's terms of the role of renormalization in gauge theories can be found at [66].

[33] Note that such singlets are not protected by the SM, they do not couple to the weak bosons, and can thus not be observed through SM interactions.

[34] This is also referred to as the see-saw mechanism. See [59], pp. 234–239. In short: the small SM neutrino masses are a consequence of the extremely high masses of the right-handed Majorana neutrinos. Since these are singlets in the SM, they cannot be observed by studying SM interactions. They are also referred to as sterile neutrinos

Neutrinoless double beta decay

In order to experimentally check the particle nature of the nature, we need to compare the behavior of e.g. $\nu_\mu(\bar{p}, -h)$ and $\bar{\nu}_\mu(\bar{p}, -h)$. The experimentally available neutrinos are always polarized, the neutrinos always being left-handed and the antineutrinos always right-handed. Thus, we rather compare the interaction with matter of $\nu_\mu(\bar{p}, -h)$ and $\bar{\nu}_\mu(\bar{p}, +h)$. Different results do not necessarily imply that the ν_μ is a Dirac particle, since this outcome might also merely be the consequence of the different polarizations. If helicity reversal were experimentally feasible, the neutrino nature could simply be tested by examining the neutrino/antineutrino-nucleon scattering [59].

The most promising experiment to test the neutrinos nature is the $0\nu\beta\beta$ decay experiment. $0\nu\beta\beta$ decay is the process where a nucleus (A,Z) decays into the nucleus $(A,Z+2)$ by the transition of two neutrons into two protons with the emission of two electrons

$$(A,Z) \longrightarrow (A,Z+2) + 2e^-.$$

The diagram of this decay is displayed in Figure 1.2. A pair of virtual W bosons is emitted by the parent nucleus, which then exchange a Majorana neutrino of mass M_M to produce the two outgoing electrons. At the emission vertex, the virtual neutrino is created together with an electron and thus needs to act as an antineutrino, while at the absorption vertex the virtual neutrino is absorbed, creating another electron, and thus it now needs to act as a neutrino. The interaction is only suppressed by a factor of order M_M/E_{ν_M} for the neutrino to be emitted as a left-handed particle at the first vertex. A zero neutrino mass ($M_M = 0$) thus implies that $0\nu\beta\beta$ decay cannot exist[35]. Since the neutrino is a Majorana particle, this left-handed "antineutrino" acts exactly the same as a left-handed "neutrino", and it can be absorbed at the second vertex without any problem. Even for very small Majorana masses M_M, this $0\nu\beta\beta$ decay can still be observed because competing decays are highly suppressed. Two consecutive single beta decays could mimic a $0\nu\beta\beta$ signal, but this background source can be suppressed by choosing the appropriate nucleus. The regular double beta decay is another possible background process, but this is highly suppressed due to phase-space considerations and has only been observed for a few isotopes.

The amplitude for the $0\nu\beta\beta$ decay can be written as

$$A\,[0\nu\beta\beta] = M_{\text{eff}} \times N, \tag{1.5}$$

[35] Remember from the SM that only for massive fermions both the left and right-handed particle and antiparticle states exist.

where N is the nuclear matrix element corresponding to the transition and M_{eff} is the effective neutrino mass for this process. N can be calculated from theoretical models but suffers from large theoretical uncertainties. M_{eff} can be expressed in terms of the Majorana masses M_M, and observation or non-observation of the $0\nu\beta\beta$ decay implies limits on the neutrino masses[36].

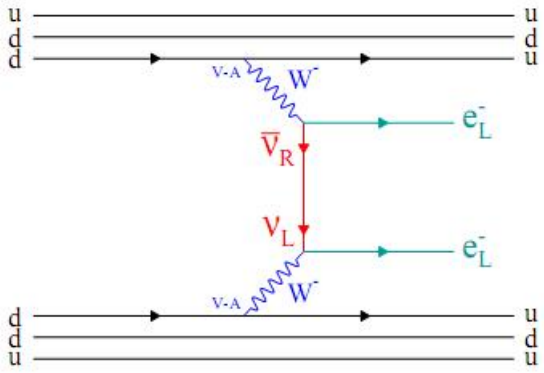

FIGURE 1.2: Feynman diagram of the $0\nu\beta\beta$ decay process in the case of the exchange of a virtual Majorana neutrino [69].

1.1.4.2 Neutrino oscillations

The fact that neutrinos must have non-zero mass is a consequence of the observation of neutrino oscillations.

Just like there is mixing in the quark sector (charged weak currents convert quark flavors into each other), which is quantified by the CKM mixing matrix, also mixing in the lepton sector exists. Depending on the nature of neutrinos, the mixing phenomenology is different. From the previous subsection we know that there are three cases for the neutrinos: pure Dirac particles, pure Majorana particles, and a mixture of both (meaning that the mass term in the Lagrangian is a mixture of both a Dirac and Majorana term). One can show that the physics of neutrino oscillations is independent of the nature of the neutrino[37]. Therefore, for simplicity reasons only the case of pure Dirac neutrinos is given[38].

The neutrino Dirac mass term is of the form (generated through the Higgs mechanism)

$$\mathcal{L}_D = -\bar{\nu}'_R M \nu'_L + h.c., \tag{1.6}$$

[36] If right-handed currents, and/or beyond the SM weak bosons exist, then these could lead to extra mechanism contributing to the total amplitude $A\,[0\nu\beta\beta]$, making the analysis much more complicated. However, according to the Schechter-Valle theorem, observation of $0\nu\beta\beta$ decay would still imply a non-zero neutrino mass, even if more exotic diagrams are responsible for it [68].

[37] Hence, neutrino oscillations do not provide any information on the nature of neutrinos.

[38] Note that this discussion is actually the first extension of the SM to accommodate for neutrino masses, as already mentioned briefly in the previous section.

where *h.c.* denotes the hermitian conjugate. M is complex-valued 3×3 matrix[39], which is in general non-diagonal, and ν'_L and ν'_R are the neutrino fields

$$\nu'_L = \begin{pmatrix} \nu_{eL} \\ \nu_{\mu L} \\ \nu_{\tau L} \end{pmatrix}, \tag{1.7}$$

and a similar expression holds for the right-handed field. If we work out the Lagrangian, non-diagonal 'mass' terms appear. To retrieve the physical mass terms, the mass matrix M needs to be diagonalized

$$M_{\text{diag}} = U^{-1}MU = U^{+}MU = \begin{pmatrix} m_1 & 0 & 0 \\ 0 & m_2 & 0 \\ 0 & 0 & m_3 \end{pmatrix}, \tag{1.8}$$

where U is a unitary 3×3 matrix. U rotates the neutrinos from one base to another, just like a rotation matrix in configuration space rotates the configuration frame. Here we go from the flavor base to the mass base. This has no net effect on the Lagrangian, and thus no physical consequences[40]

$$\mathcal{L}_D = -\bar{\nu}'_R M \nu'_L + h.c. = -\bar{\nu}'_R U M_{\text{diag}} U^{+} \nu'_L + h.c. = -\bar{\nu}_R M_{\text{diag}} \nu_L + h.c., \tag{1.9}$$

where we used $\bar{\nu}_R = \bar{\nu}'_R U$ and $\nu_L = U^{+}\nu'_L$. Using $\nu = \nu_L + \nu_R$ and writing down the components, this becomes

$$\mathcal{L}_D = -\bar{\nu} M_{\text{diag}} \nu = -\sum_{j=1}^{3} m_j \bar{\nu}_j \nu_j. \tag{1.10}$$

From this we can conclude that the neutrinos observed in weak interactions are actually superpositions of the neutrino mass eigenstates, and thus have no definite mass. Note that this formalism can easily be generalized to the case of n lepton families.

From quantum mechanics it follows that this mixing implies neutrino oscillation phenomena. The state vector of a flavor neutrino ν_l ($l = e, \nu, \tau$) with momentum p produced in a weak interaction at a certain time $t_0 \equiv 0$ is given by the superposition of the neutrino eigenstates ν_j ($j = 1, 2, 3$) with momentum p, negative helicity (we are

[39] Assuming only the three known lepton families. Electroweak precision measurements at the Large Electron Positron Collider (LEP) at CERN and at the Stanford Linear Collider (SLC) at SLAC constrain the number of light neutrinos in the standard model to exactly three [70].

[40] Think of it as changing spectacles. With the first spectacles we did not see the different neutrino mass states, everything was a little blurry, while they are clearly visible with our new spectacles.

looking at left-handed neutrinos) and definite masses m_j.

$$|\nu_l\rangle = \sum_j U_{lj}^* |\nu_j\rangle. \tag{1.11}$$

The energy E_j for the state $|\nu_j\rangle$ is given by

$$E_j = \sqrt{m_j^2 + p^2} \approx p + \left(\frac{m_j^2}{2p}\right), \tag{1.12}$$

if we assume that the momentum p is much higher than the mass m_j. Using the evolution operator, the particle state at time t is given by

$$|\nu_l\rangle_t = \sum_j e^{-iE_j t} U_{lj}^* |\nu_j\rangle. \tag{1.13}$$

Expanding the mass states in the flavor base in the right-hand side of Equation (1.13) gives

$$|\nu_l\rangle_t = \sum_{l'} A_{\nu_{l'},\nu_l}(t) |\nu_{l'}\rangle, \tag{1.14}$$

where $A_{\nu_{l'},\nu_l}(t) = \sum_j U_{l'j} e^{-iE_j t} U_{lj}^*$ is the probability amplitude at a time t for the transition $\nu_l \to \nu_{l'}$. The probability that after a time t the neutrino has oscillated to the flavor l' is given by

$$P(\nu_l \to \nu_{l'}; t) = |A_{\nu_{l'},\nu_l}(t)|^2. \tag{1.15}$$

Assuming the neutrinos are extremely relativistic one can substitute the (travel) time t by L/c, with L the distance travelled by the neutrino during this time. A straightforward calculation then gives (in natural units)

$$P(\nu_l \to \nu_{l'}; L, E) = \delta_{ll'} - 4 \sum_{j>i}^{j=3} \sum_{i=1}^{3} U_{li} U_{l'i} U_{lj}^* U_{l'j}^* \sin^2\left(\frac{1.27 \Delta m_{ij}^2 L}{E}\right), \tag{1.16}$$

where $\Delta m_{ij}^2 = m_i^2 - m_j^2$. Note first of all that the probability $P(\nu_l \to \nu_l; t)$ is not necessarily equal to 1, but depends on the distance L (which from an experimental point of view is the distance between the neutrino source and the neutrino detector), the energy of the neutrino, and the amount of mixing in the lepton sector expressed by the matrix U. The quadratic mass differences are constant, but it is important to realize that the second term in (1.16) becomes zero if all the neutrino mass eigenstates have equal mass. The observation of neutrino oscillations thus implies that at least one of the three neutrinos has a non-zero mass.

There are two types of neutrino oscillation experiments: if one is studying e.g. a ν_e source, then one can either look only for ν_e's and check whether there is a deficit of

detected ν_e's, or one can look at the other flavors and check whether these appear in the detector. The former experiment looks at the ν_e survival probability $P(\nu_e \to \nu_e; L, E)$, while the latter experiment looks at the ν_e disappearance probability $P(\nu_e \to \nu_\mu; L, E) + P(\nu_e \to \nu_\tau; L, E) = 1 - P(\nu_e \to \nu_e; L, E)$.

Neutrino oscillation experiments can also shed more light on CP violation in the lepton sector. The mixing matrix for three families connects the flavor base with the mass base

$$\begin{pmatrix} \nu_e \\ \nu_\mu \\ \nu_\tau \end{pmatrix} = \begin{pmatrix} U_{e1} & U_{e2} & U_{e3} \\ U_{\mu 1} & U_{\mu 2} & U_{\mu 3} \\ U_{\tau 1} & U_{\tau 2} & U_{\tau 3} \end{pmatrix} \begin{pmatrix} \nu_1 \\ \nu_2 \\ \nu_3 \end{pmatrix}. \tag{1.17}$$

A unitary matrix in three dimensions can be written as three consecutive rotations, a real rotation around the 'third mass eigenstate axis', followed by an imaginary rotation around the 'second mass eigenstate axis', and finally a real rotation around the 'first mass eigenstate axis'. This involves three mixing angles θ_{12}, θ_{13}, and θ_{23}, and one CP violating phase δ

$$U = \begin{pmatrix} 1 & 0 & 0 \\ 0 & \cos\theta_{23} & \sin\theta_{23} \\ 0 & -\sin\theta_{23} & \cos\theta_{23} \end{pmatrix} \begin{pmatrix} \cos\theta_{13} & 0 & \sin\theta_{13} e^{-i\delta} \\ 0 & 1 & 0 \\ -\sin\theta_{13} e^{i\delta} & 0 & \cos\theta_{13} \end{pmatrix} \begin{pmatrix} \cos\theta_{12} & \sin\theta_{12} & 0 \\ -\sin\theta_{12} & \cos\theta_{12} & 0 \\ 0 & 0 & 1 \end{pmatrix}. \tag{1.18}$$

Why this phase δ expresses CP violation can be understood as follows. If the unitary matrix U would be real, which is the case if $e^{\pm i\delta} = 1$ or $\delta = 0$, then one can see from (1.16) that $P(\nu_l \to \nu_{l'}; L, E) = P(\nu_{l'} \to \nu_l; L, E)$, which implies invariance under time reversal (T). Assuming CPT as a universal symmetry, this implies that CP is also conserved. Thus for $\delta \neq 0$ one can conclude that neutrino oscillation processes violate CP conservation. Note that an extremely small θ_{13} could make it impossible to detect this CP violation.

A few remarks to end the discussion on the neutrino oscillation phenomenon:

- The expressions for the oscillation probability between the antineutrinos are derived in a similar fashion.
- To simplify the mathematics one can also look at oscillations between only two families. This is often a very good approximation in experimental situations. In this case, CP violation is not possible anymore. The survival probability for ν_e is plotted in Figure 1.3(a) for the case of two families.
- Oscillations between active (left-handed) and sterile (right-handed) neutrinos (and analogously for the antineutrino case) is also possible. It complicates the discussion

a little bit more, since the dimension of the mixing matrix increases by one unit for every sterile neutrino that is added to the story. Since sterile neutrinos do not interact through the SM weak interaction, they cannot be detected with the regular techniques, and one could only look for a deficit of active neutrinos.

– In the case of Majorana neutrinos, the unitary matrix U is multiplied by a diagonal matrix $P = \text{diag}(1, e^{i\frac{\alpha_{21}}{2}}, e^{i\frac{\alpha_{31}}{2}})$ containing two additional Majorana phases. This does not influence the oscillation formulas, though it does have an impact on the decay rate of the $0\nu\beta\beta$ decay.

– So far, only neutrino oscillations in vacuum have been discussed. The presence of matter influences neutrino oscillations. It is theoretically described by the Mikheyev-Smirnov-Wolfenstein effect (MSW) and needs to be accounted for in a.o. solar neutrino oscillation experiments as the neutrinos from the Sun have to travel through the Sun first (it is only significant for high-energy neutrinos) [71].

– Depending on the nature of neutrinos, extending the SM to account for neutrino oscillations adds 7 or 9 parameters to the list of 19 parameters (3 mixing angles, 1 or 3 CP-violating phases, and 3 neutrino masses).

– The three neutrino mass states expressed in terms of the weak eigenstates give the following flavor combinations:

  – Mass state m_1: dominated by the electron neutrino flavor.
  – Mass state m_2: almost equal contributions from all three flavors.
  – Mass state m_3: almost no contribution from the electron neutrino flavor.

  To this date, the relative order of these mass states is still not determined. There are two possibilities, normal hierarchy and inverted hierarchy, depicted in Figure 1.3(b). This is called the neutrino mass hierarchy problem (NMH). NMH could be solved by determining the sign of Δm^2_{13} in atmospheric neutrino oscillations. It can be shown that two-neutrino flavor oscillations in vacuum are insensitive to the sign of the relevant Δm^2. However, due to the MSW effect in the atmosphere, atmospheric neutrino oscillations between muon neutrinos and electron neutrinos could reveal the true neutrino mass hierarchy, provided that θ_{13} is not too small. The normal and inverted mass hierarchy make significantly different predictions for the survival probabilities of the muon neutrino for various energies and baselines. PINGU, the proposed upgrade for the IceCube detector (both discussed in Chapter 2), is aimed to be sensitive to the NMH through this channel.

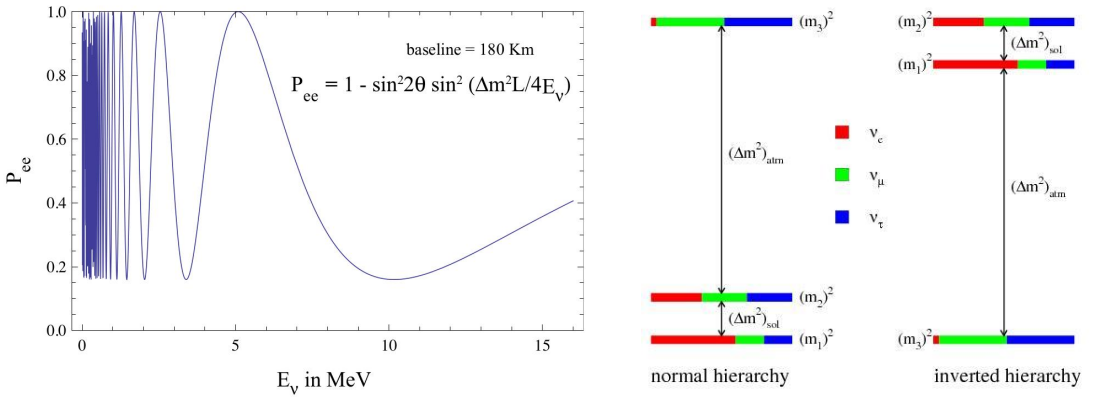

(a) (b)

FIGURE 1.3: (a) The ν_e survival probability as a function of the neutrino energy E_ν for a $L = 180$ km, $\Delta m^2 = 7.0 \times 10^{-5}$ eV^2 and $\sin^2 2\theta = 0.84$ in a two family model [72]. (b) The neutrino mass hierarchy problem: normal versus inverted hierarchy [73].

1.2 Neutrinos in astroparticle physics

Because of their specific intrinsic particle properties, neutrinos can be used to probe the Universe, as an alternative to photons. In this section, we look at the neutrino from the viewpoint of astroparticle physics.

1.2.1 Neutrinos as messengers

Human kind has always been intrigued by the beauty and mystery of the night sky. A girl watching the stars lying on her back in the middle of an open field, an amateur astronomer spending his nights behind a telescope, and an astrophysicist sitting behind a computer analyzing the data from an infrared telescope mounted on a satellite all have one thing in common. They all study the Universe using the electromagnetic spectrum, albeit the one more systematic than the other. Astrophysicists have been mostly using the photon as source of information in order to explain the physics behind objects such as stars, galaxies, and interstellar gas clouds, and phenomena such as supernovae and the expansion of the Universe. Where originally only the optical window[41] could be studied, one can now study the whole electromagnetic spectrum, ranging from the low-energetic radio waves in radio astronomy to the high-energetic gamma rays in gamma-ray spectroscopy (Figure 1.4). Besides that, astrophysicists also study the Universe by looking at cosmic rays. Cosmic radiation or cosmic ray particles consists of all the stable charged particles and nuclei[42] that are accelerated at astrophysical sources and then reach the Earth's atmosphere.

[41] From about 400 nm to about 800 nm.
[42] From hydrogen to iron.

Unfortunately, there is one problem with both photons and cosmic rays as cosmic messengers. The interesting physics for the various objects ranging from stars and supernovae to Active Galactic Nuclei (AGN) and Gamma-Ray Bursts (GRB) happens inside their cores. However, these inner regions are unreachable by optical means due to constant interactions of photons with matter. E.g. it takes a photon of the order of 30000 years to escape the center of the Sun or photons emitted. Furthermore, photons might also be stopped on their way to the Earth due to interaction with e.g. interstellar gas. Charged cosmic ray particles on the other hand have the downside that they interact with the electromagnetic fields that they encounter on their journey to the Earth, altering their energetic and directional properties and thus providing us with 'false' information on their origin and/or leading to attenuated fluxes.

The past few decades a new field in astrophysics emerged, neutrino astrophysics. Neutrinos are (almost) perfect messengers from astrophysical objects. Because they have no electric charge and they interact only very weakly with matter they propagate virtually unhindered through the cores of their sources and through the Universe and thus still carry their initial information from their creation. However, the downside is that they are very difficult to detect (because they interact very weakly) and extremely large detectors[43] are needed to actually observe them (see also Section 1.3 and Chapter 2).

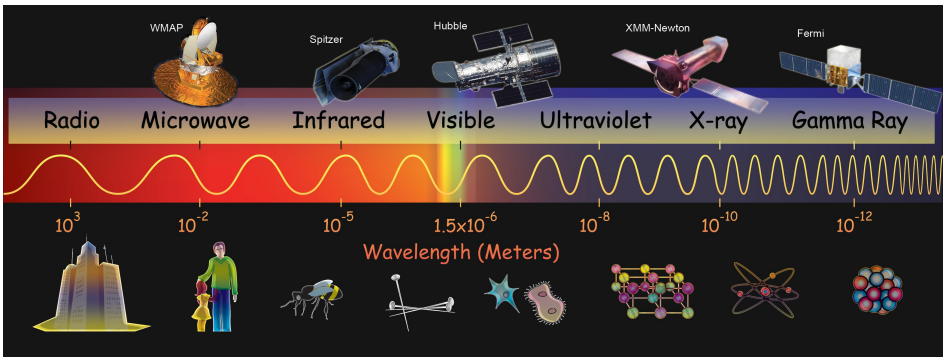

FIGURE 1.4: Electromagnetic spectrum and the corresponding astrophysics fields [74].

1.2.2 Astrophysical neutrino sources

Several astrophysical neutrino sources exist, most of them related to cosmic rays. One can distinguish between neutrinos produced inside and outside the atmosphere, where the sources outside the atmosphere range from the Sun to galactic and extragalactic sources. Figure 1.5 shows the neutrino flux over a very broad energy range, together

[43] Typically referred to as neutrino telescopes.

with the (expected) sources. Sources vary from the cosmic neutrino background[44] at meV energies and below, to GZK neutrinos (see further) at the opposite end of the energy spectrum. Up to very recently, only two extraterrestrial neutrino sources had been identified, namely the Sun and supernovae. In May 2013, IceCube was the first experiment to identify extragalactic neutrinos. These neutrinos had an energy of about 10^{15} eV (1 PeV) [75]. Their exact origin is still a mystery.

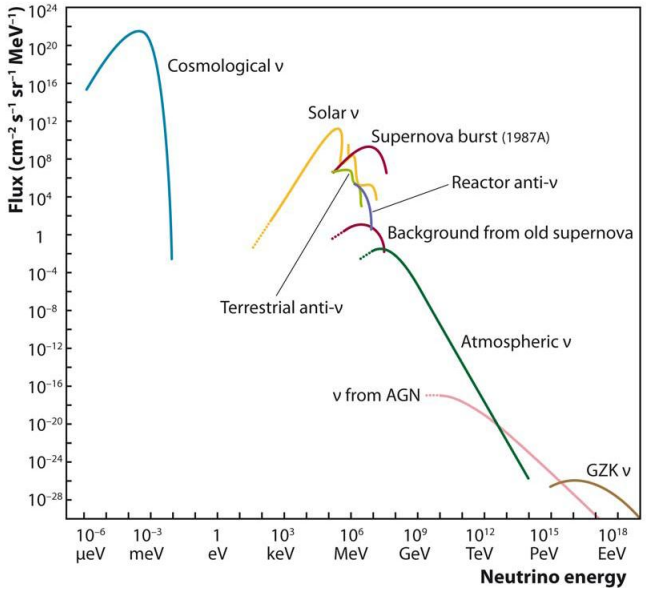

FIGURE 1.5: Neutrino flux as a function of the neutrino energy. The various known and anticipated astrophysical sources are indicated on the figure [76].

1.2.2.1 Atmospheric neutrinos

Cosmic rays

The Earth's atmosphere is under constant bombardment of charged particles from outer space. These particles are mostly protons (86%) and He-nuclei (11%), but can also be electrons (2%) or heavier nuclei (1%). One also distinguishes between primary and secondary cosmic radiation, where the former are accelerated at astrophysical sources, while the latter are produced by interactions of the primary particles with interstellar gas. The small contribution of nuclei such as lithium and beryllium, as well as antiparticles like antiprotons and positrons are mostly secondary cosmic ray particles. The cosmic ray spectrum is approximately isotropic for energies below 1 PeV and it barely

[44]The cosmic neutrino background is the Universe's background particle radiation composed of neutrinos, stemming from a so-called freeze-out (or decoupling) a few seconds after the Big Bang. After this freeze-out neutrinos were not anymore in thermal equilibrium with the baryons. The cosmic neutrino background is similar to the cosmic microwave background, which is thermal radiation filling the observable Universe almost uniformly. Because these cosmological neutrinos have very low energies, they are extremely hard to detect [65].

varies with time[45]. The energy spectrum of the nuclear part of the primary cosmic rays is given in Figure 1.6(a). Except for the lowest energies, the spectrum follows a power law up to 1 PeV [77]

$$\Phi(E) = \frac{dN}{dE dA d\Omega dt} \propto E^{-2.7}, \tag{1.19}$$

where Φ is the flux, N is the number of cosmic ray particles, A is the active surface of the cosmic ray detector, and Ω is the solid angle covered by the detector. Above 1 PeV, the spectrum steepens and follows a power law $\Phi(E) \propto E^{-3}$ up to 10^{18} eV (1 EeV). This change in slope is referred to as the knee of the spectrum. It is linked to a change in acceleration mechanisms and/or propagation effects for the charged particles in our galaxy. In this part of the spectrum the cosmic ray particles are energetic enough to escape the galactic magnetic field, causing a decrease in the flux[46]. At 10^{18} eV the spectrum flattens out again, probably due to ultra-high energy cosmic rays from unknown extragalactic accelerators. This change in slope is called the ankle. At an energy of 6×10^{19} eV a cut-off is expected, the GZK cut-off, due to proton interactions with the cosmic microwave background, producing pions and thus decreasing the proton energy [78, 79][47]. These pions can then decay into neutrinos, which are referred to as GZK neutrinos.

Atmospheric neutrinos

Cosmic rays impinging on the Earth's atmosphere lead to atmospheric neutrinos. Figure 1.6(b) shows a drawing of a primary cosmic ray particle interacting with an atmospheric nucleus at the top of the atmosphere, initiating a cosmic air shower[48]. A large number of hadrons is created, mostly pions, which at their turn either interact with atmospheric nuclei or decay. Neutral pions decay in photons which then induce an electromagnetic shower, while charged pions can decay in muons and muon neutrinos. The neutrinos easily reach the Earth's surface and can even penetrate the Earth. Looking at Figure 1.6(b), one naively expects twice as many muon neutrinos coming from the atmosphere than electron neutrinos. However, the ratio is found to be different from 2, which is now attributed to neutrino oscillations (for which the MSW effect is also relevant) [57].

[45] It has been approximately constant over a period of about one billion years.

[46] The magnetic rigidity R quantifies the influence of a uniform magnetic field B on a charged particle with momentum p and charge number Q through $R = B\rho$, where $\rho = p/QB$ is the gyroradius or bending radius of the particle. An increase in momentum causes an increase in bending radius, or in other words less bending. The galactic magnetic field is assumed to be smaller than 1 nT. Note that the magnetic rigidity also depends on electric charge, such that for particles with different charge numbers the knee is at slightly different energies.

[47] It is however also possible that this cut-off is magnetic rigidity dependent and actually implies that no sources exist which can accelerate cosmic ray particles to energies above this cut-off.

[48] Also referred to as an extensive air shower.

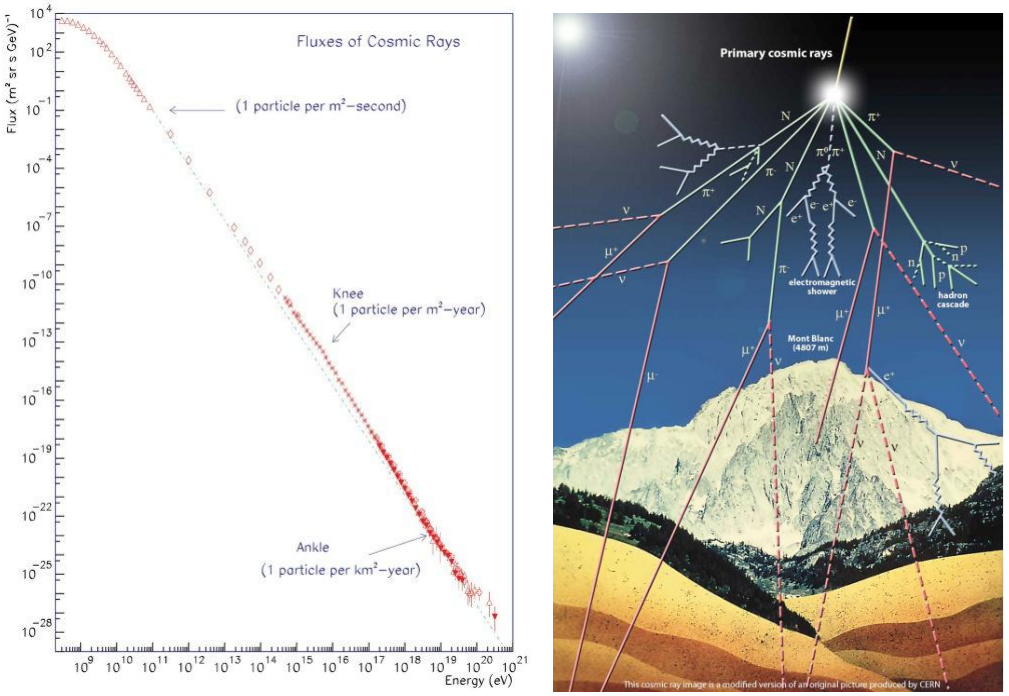

(a) (b)

FIGURE 1.6: (a) Energy spectrum of the primary cosmic rays [80]. (b) A cosmic ray particle hitting the top of the Earth's atmosphere hereby inducing a cascade shower [81].

The question still remains what these cosmic ray sources are. The production of cosmic neutrinos is also expected to happen at some of the cosmic ray sources, also referred to as cosmic accelerators. Neutrinos from such cosmic accelerators are called extrasolar neutrinos.

Before addressing the solar and extrasolar neutrinos, we take a closer look at the cosmic ray muon flux, because this flux is used as the input flux for the Cherenkov detector, designed and constructed for this thesis.

Cosmic ray muons at sea level

At sea level muons are the most abundant charged particles, with a flux of the order of 1 muon per cm^2 and per minute for horizontal detectors [82]. They are typically produced high in the atmosphere ($\sim$ 15 km) and lose about 2 GeV due to ionization before reaching the ground (2 MeV per g cm^{-2}). The muon energy and angular spectrum is a convolution of the production spectrum, the energy losses in the atmosphere, and the decay probability. It is almost flat below 1 GeV and then decreases roughly by a factor of 10 at 10 GeV, after which it follows the primary cosmic ray flux until 100 GeV. In the TeV range the flux decreases even more rapidly, as the pions from which the muons originate interact in the atmosphere, and thus lose energy, before they decay to muons.

Figure 1.7(a) shows the muon flux as a function of momentum. Figure 1.7(b) shows the angular distribution for muons of different energies. The overall angular distribution of muons is given by

$$I = I_0 \cos^2 \theta, \tag{1.20}$$

where I is the muon intensity and θ is the zenith angle[49]. This is characteristic for muons with an energy of approximately 3 GeV. At larger zenith angles, the muon flux is lower since muons with a large zenith angle need to travel a longer distance before reaching the surface of the Earth, and thus have a greater probability to decay along this track. At high muon energies ($\sim$ 1 TeV) the angular distribution approaches a $1/\cos\theta$ relation [82].

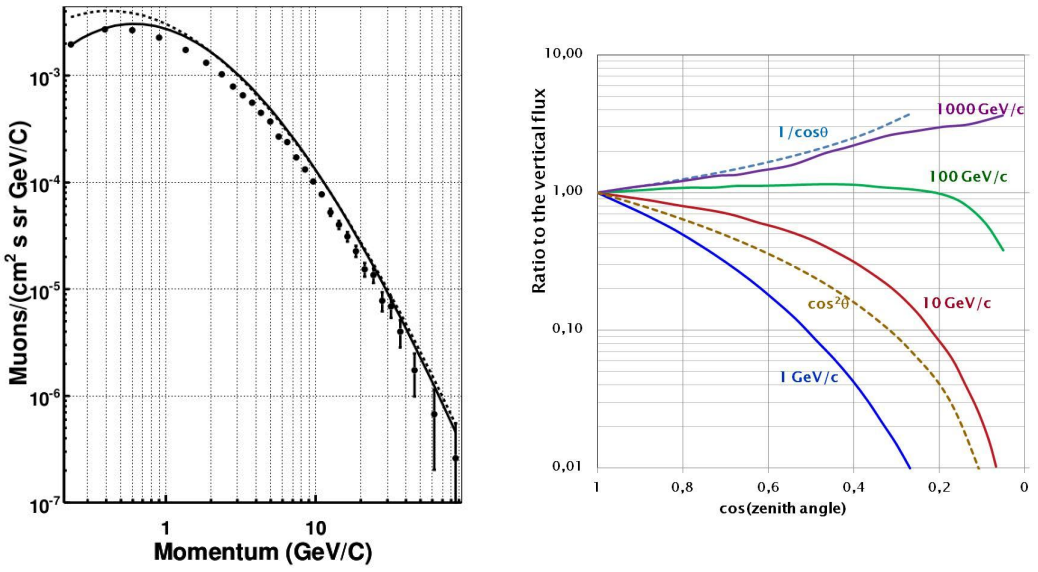

(a) (b)

FIGURE 1.7: (a) Cosmic ray muon flux as a function of muon momentum at sea level. The dashed line represents measurements from Allkofer *et al.* [83], while the solid line represents measurements from Rastin [84]. The points are simulated using GEANT4 [85]. (b) Angular distribution of cosmic ray muons at sea level for different muon energies [86].

Cosmic ray muons underground

Besides neutrinos, muons are the only particles penetrating the Earth to significant depths, causing tertiary fluxes of photons, electrons, and hadrons. The muon energy loss in a certain medium (e.g. rock, water, or ice) can be parametrized as

$$\frac{dE_\mu}{dX} = -a - bE_\mu, \tag{1.21}$$

[49] $\theta = 0$ corresponds to a downgoing muon, perpendicular to the surface of the Earth.

where X is the distance travelled in the medium expressed in g/cm^2, a is the ionization loss[50], and b accounts for the fractional energy loss due to radiation processes (Brehmstrahlung[51], pair production[52], and photonuclear reactions[53]). Cherenkov radiation[54] and transition radiation[55] are not important for energy loss. The parameters a and b depend slightly on energy and on the composition of the medium ($a \propto Z/A$ and $b \propto Z^2/A$). Below ∼500 GeV, ionization losses are more important than radiative losses. This is also shown in Figure 1.8(a) ($E_{\mu c}$), where the stopping power for antimuons in copper is displayed. A typical value for a is around 2 MeV g^{-1} cm^2. Figure 1.8(b) shows the different contributions to b in iron as a function of the muon energy. The underground muon flux can be estimated from the muon flux in the atmosphere and the rate of muon energy loss.

1.2.2.2 Solar neutrinos

Neutrino flux from nuclear fusion chains

During the Sun's stable period on the main sequence, nuclear fusion chains inside its core generate luminous energy (making life on Earth as we know it possible) together with low-energy electron neutrinos. The electron neutrinos easily escape the Sun (as opposed to the photons) and reach the Earth's surface quickly after. Measuring the solar neutrino flux and comparing it with Standard Solar Model predictions has led to the discovery of neutrino oscillations [65].

The two nuclear fusion chains responsible for the energy generation in the Sun are the so-called proton-proton chain and *CNO*-cycle [87]. The former is the main solar neutrino source (∼ 98.4%). Figure 1.9(a) displays the three possible proton-proton cycles: ppI, $ppII$, and $ppIII$. The net reaction is each time

$$4H \rightarrow {}^4He + 2e^+ + 2\nu_e + 26.73\ MeV. \tag{1.22}$$

The released energy of 26.73 MeV per cycle is a consequence of the famous $E = mc^2$ relation. The two electron neutrinos together have 0.59 MeV on average. The reactions inside the proton-proton chain producing neutrinos are referred to as the pp reaction,

[50] Described by the Bethe-Bloch formula [82].
[51] Radiation due to the deceleration of a charged particle when deflected by another charged particle [82].
[52] Radiation due to annihilation of a charged particle and its antiparticle [82].
[53] Electromagnetic interaction with a nucleus.
[54] Radiation emitted when a charged particle travels faster than the speed of light in a certain medium [82]. See Section 1.3.2.
[55] Radiation emitted when a charged particle crosses the border between two media with different optical properties [82].

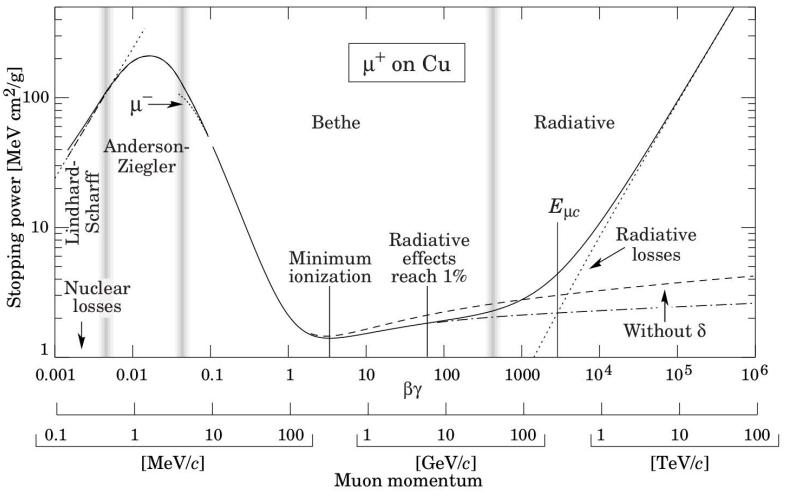

(a)

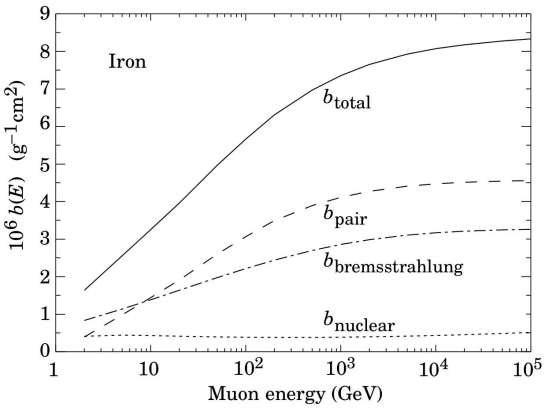

(b)

FIGURE 1.8: (a) Stopping power ($\langle -dE/dx \rangle$) for antimuons in copper as a function of $\beta\gamma = p_\mu/m_\mu c$ and muon momentum p_μ [82]. (b) Contributions to the fractional muon energy loss in iron due to the different radiation processes [82].

the *pep* reaction, the *hep* reaction, the ^7Be reaction, and the ^8B reaction. Figure 1.9(b) shows the calculated solar neutrino spectrum for the different sources. Note that the ^7Be and *pep* spectra are line spectra, while the other spectra are continuous.

Neutrino flux from WIMP annihilations in the Sun

Another possible neutrino flux coming from the Sun could be an indicator of beyond the SM physics, related to the dark matter problem. From simulations it appears that the observed galaxy mass distribution is best reproduced using a cold dark matter assumption [90]. This implies that we should be looking for very massive, electrically neutral, weakly interacting particles. The particles need to have a large mass, such that they are slow and hence "cold". Furthermore, they cannot interact through the electromagnetic nor strong interaction, as they would not be dark matter particles in that case.

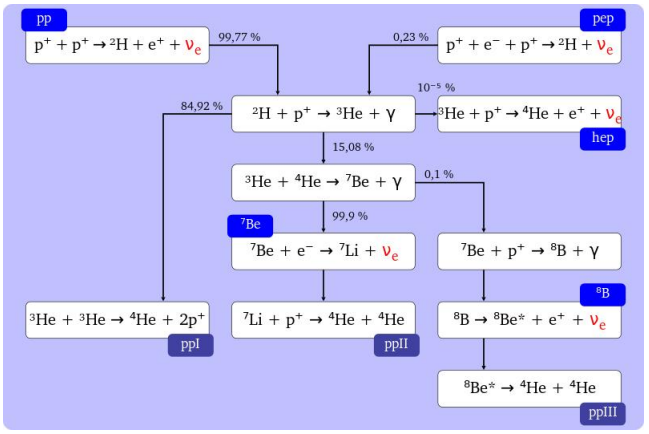

(a)

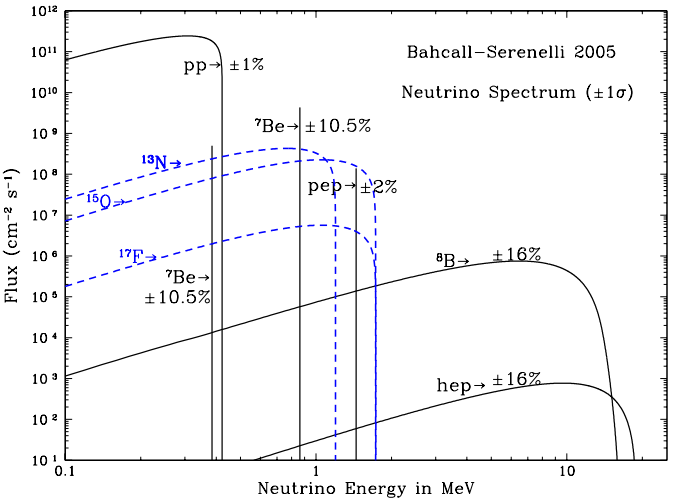

(b)

FIGURE 1.9: (a) Reactions in the proton-proton chain. The percentages are the corresponding branching ratios [88]. (b) Calculated solar neutrino spectrum for the different processes [89].

A candidate for such particles are the so-called weakly interacting massive particles or WIMPs. Note that, besides their large mass, they are very similar to the SM neutrinos. The supersymmetric partners of the neutrinos in SUSY models, the neutralinos, are possible candidates for WIMPs if they are Majorana particles. These WIMPs could be captured gravitationally in the Sun, where they then thermalize and accumulate. It is then possible for them to annihilate with each other, forming SM model particles such as neutrinos, gamma rays, positrons, or antiprotons. Again, the neutrinos have the advantage of easily escaping the Sun's interior and leave for the Earth, hopefully to be captured by a neutrino telescope. Similarly, neutrinos coming from the Earth's center or originating from the galactic center, could have their origin in WIMP annihilations. The mass of neutralinos is expected to be in the GeV-TeV range [91, 92].

1.2.2.3 Extrasolar neutrinos

The origin of most extrasolar neutrinos is similar to the creation of atmospheric neutrinos through interaction of cosmic rays with nuclei in the atmosphere. A proton is accelerated by an astrophysical source and interacts with matter in the outer-layers of this source or on its way to the Earth, leading to pions, for which the charged ones decay to charged leptons accompanied by their neutrino partners. In terms of energy, one can distinguish between neutrinos created inside or outside our galaxy [93]. A few of such astrophysical sources which are currently being investigated are listed below:

- **Active Galactic Nuclei (AGN)** are the most powerful radiation sources in the Universe. These are located at the center of a galaxy and presumably create cosmic rays through mass accretion by a supermassive black hole ($\sim 10^8$ M_{Sun}). The generated cosmic ray particles then interact with matter or radiation in the accretion disk, or with photons from the associated jets, generating the pions that eventually decay to neutrinos. The recently observed PeV neutrinos at IceCube, could possibly be the first hint of AGN neutrinos [75].

- **Gamma-Ray Bursts (GRBs)** is a collective name for phenomena causing very short and intense gamma ray explosions in the Universe. Many of them have been observed in distant galaxies, but the diversity among them, both in spectra and duration, is so big that it is hard to model GRBs. One model suggests that these bursts are related to the collapse of a massive star (supernova), possibly together with the formation of a black hole [94]. It is believed that matter is ejected at high speeds during such a burst, hereby accelerating protons to very high energies, which again produce neutrinos through charged pions. Ideally, after a GRB is observed with a neutrino telescope, one should wait for the optical flash that is a consequence of the supernova debris hitting material around the star a bit later. This optical flash should be proceeded by a flux of neutrinos if GRBs are astrophysical neutrino sources. However, no such neutrinos have been observed so far[56].

- **Supernovae of type II** are the spectacular events by which massive stars come to their end. Neutrinos play a key role in these violent explosions and the optical observation of a type II supernova is usually preceded by a huge burst of neutrinos. The first supernova to be observed in this manner was the supernova SN1987A, named after the year of observation [96]. Supernova neutrinos have an average energy of ~ 10 MeV. A process responsible for neutrino production in supernovae

[56] In April 2013, GRB 130427A was the brightest GRB to be observed on Earth so far. No high-energy neutrinos in spatial and temporal coincidence with this GRB were detected at the IceCube detector [95].

is

$$p + e^- \rightarrow n + \nu_e, \tag{1.23}$$

which converts the star core to a neutron star. Other processes producing neutrinos are

$$e^+ + e^- \rightarrow \nu_i + \bar{\nu}_i, \tag{1.24}$$

with $i = e, \nu, \tau$ [65].

1.3 Detecting neutrinos

From the previous two sections it is clear that knowing how to detect neutrinos is of crucial importance to gain more insight into its intrinsic properties and behaviour, such as its nature, mass and the process of oscillations, as well as to learn more about the Universe, as the neutrino appears to be the ideal cosmic messenger.

1.3.1 Neutrino interaction with matter

Neutrinos only undergo weak interactions with the nucleons and electrons constituting the matter through which they travel[57]

$$\nu_l + N \rightarrow l^- + X, \tag{1.25}$$

$$\bar{\nu}_l + N \rightarrow l^+ + X, \tag{1.26}$$

$$\nu_l + N \rightarrow \nu_l + X, \tag{1.27}$$

$$\bar{\nu}_l + N \rightarrow \bar{\nu}_l + X, \tag{1.28}$$

$$\nu_l + e^- \rightarrow \nu_l + e^-, \tag{1.29}$$

where N is a nucleon and X represents a hadronic cascade. The first two interactions are charged current (CC) interactions[58], while the final two are neutral current (NC) interactions[59]. In CC interactions, the neutrino is converted into its corresponding charged lepton, while the kinetic energy transferred to the nucleon generates a hadronic cascade. In NC reactions, the neutrino scatters off the nucleon, again causing a hadronic cascade. The hadronic cascade typically carries 20% of the initial neutrino energy. Neutrino-electron interaction (1.25) is only relevant at very high energies (∼PeV), where its cross-section has a resonance[60].

[57] Remember that there is (unfortunately) no such thing as a block of muonic or tauonic matter.
[58] Take place through W exchange.
[59] Take place through Z exchange.
[60] Also known as the Glashow resonance [97].

Reaction (1.25) is shown schematically in Figure 1.10. The direction of the charged lepton forms an angle θ_s with the direction of the original neutrino. This angle is typically very small, and decreases with increasing energy. This is an important feature for neutrino detection (see *Neutrino detection with a Cherenkov detector*).

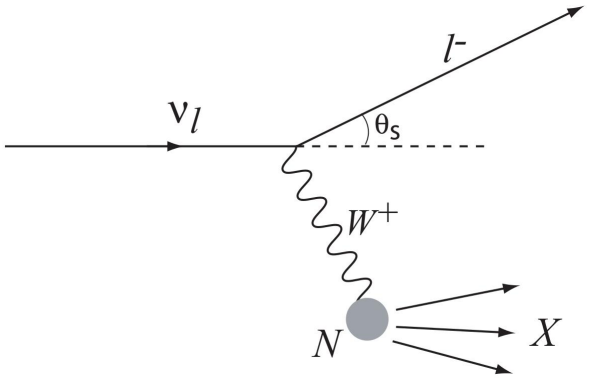

FIGURE 1.10: Schematic view of a neutrino scattering off a nucleon through the charged current weak interaction [98].

Figure 1.11 displays the total CC cross-section for muon neutrino and muon antineutrino scattering off nucleons over a broad range of energies. One sees a linear relationship between neutrino energy and the cross-section at high energies, as expected from point-like scattering from quarks (i.e. deep inelastic scattering). At lower energies ($E_\nu < 10$ GeV) this relation does not hold anymore due to quasi-electric scattering (where the neutrino sees a nucleon rather than a quark) and resonance production processes (inelastic scattering off a nucleon leading to resonances, such as the Δ particle, which then quickly decay in a nucleon and a pion). Notice in Figure 1.11 that the neutrino cross-section is roughly twice as large as the antineutrino cross-section. The NC cross-sections are generally smaller than their CC counterparts. The total neutrino interaction cross-section is given by the sum of the CC and NC cross-sections. To have an idea of the smallness of these cross-sections, one can compare with electromagnetic cross-sections, which are typically 6 orders of magnitude larger.

1.3.2 Neutrino detection: the Cherenkov effect

Technically, neutrinos are always detected indirectly[61]. However, one can distinguish between neutrinos detected "directly" through their reaction products in a certain medium, and neutrinos detected "indirectly" by looking at parameters expressing their absence, such as the missing transverse energy or momentum.

[61] This is actually true for all particles. The presence of a fundamental particle is inferred from its response to the properties of a certain medium or interaction field which consist the detector, provided that its experimental signature in that situation is either predicted or already known.

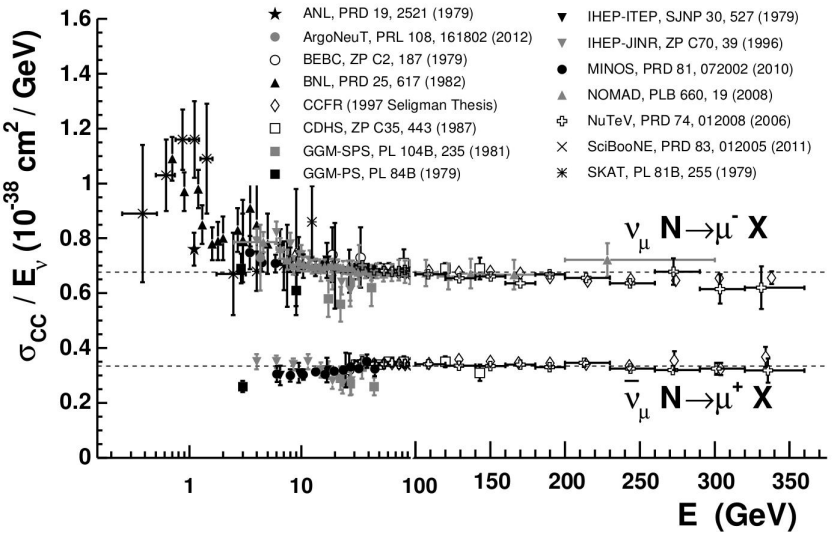

FIGURE 1.11: Charged current muon (anti)neutrino-nucleon scattering cross-section divided by the neutrino energy, as a function of the neutrino energy [82].

In what follows, only neutrino detection through the so-called Cherenkov effect is addressed, as this is of further interest in this thesis. This is an example of a "direct" measurement.

Cherenkov effect

The Cherenkov effect is the electromagnetic version of the sonic boom. It occurs when a charged particle travels through a dielectric medium, defined by its refractive index n, with a speed v greater than the speed of light c/n in that medium. This causes an electromagnetic shock wave along its track similar to the shock waves created by an aircraft going faster than the speed of sound in the atmosphere. Travelling through this medium, the highly relativistic charged particle loses energy polarizing the molecules of the medium and thus generating electric dipoles along its track. The excited dipoles rapidly decay back to their ground states, hereby emitting dipole radiation. As long as the charged particle satisfies the Cherenkov condition

$$v > \frac{c}{n}, \tag{1.30}$$

the electric dipole radiation interferes constructively, leading to a light cone co-moving with the charged particle and with a half opening angle θ satisfying

$$\sin\theta = \frac{1}{\beta n}, \tag{1.31}$$

where $\beta = v/c$. When $v < c/n$, the dipoles are positioned symmetrically along the muon track, giving rise to a vanishing global electric dipole field. This is displayed in Figure 1.12(a). From the point of view of a particle physics, the electric dipoles coherently send out photons under an angle θ_C which is determined by the particle speed and the dielectric properties of the medium

$$\cos\theta_C = \frac{1}{\beta n}, \tag{1.32}$$

as shown in Figure 1.12(b)[62]. Note that the azimuthal angle ϕ is uniformly distributed between 0 and 2π.

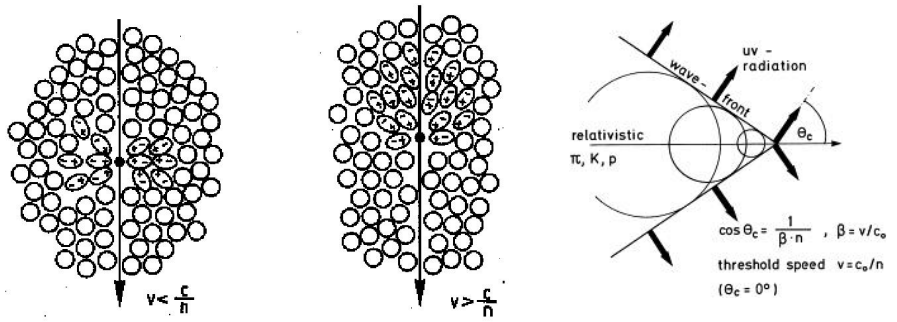

(a) (b)

FIGURE 1.12: (a) Electric dipole formation in a medium with refraction index n due to the passage of a highly relativistic charged particle satisfying the Cherenkov condition $v > c/n$ [99]. (b) Schematic view of the formation of the Cherenkov light cone [100].

The spectral distribution of Cherenkov radiation is described by the Frank-Tamm relation

$$\frac{dN}{d\lambda} = 2\pi\alpha Z^2 \int_{\lambda_0}^{\lambda_1} \left(1 - \frac{1}{n^2\beta^2}\right) \frac{d\lambda}{\lambda}, \tag{1.33}$$

where λ is the wavelength of the Cherenkov photon, α is the electromagnetic fine-structure constant, and Z is the atomic number of the charged particle. Note that it does not implicitly take the Cherenkov condition into account. Cherenkov radiation is only relevant in the optical region (including the UV region) because for other wavelengths either the refractive index is less than one (such that the Cherenkov condition cannot be fulfilled) or the absorption is too strong for the photons to propagate through the medium.

[62] A more precise treatment, taking into account the change in direction of the charged particle due to recoil, gives $\cos\theta_C = \frac{1}{\beta n} + \frac{\hbar k}{2p}\left(1 - \frac{1}{n^2}\right)$ [99].

Cherenkov detector

A Cherenkov detector is a detector that uses the Cherenkov effect to infer the presence of a particle in a medium and/or determine the properties of the particle. These detectors usually rely on photomultipliers (PMTs) to detect the Cherenkov photons. Photomultipliers have a high sensitivity and gain, a fast response time, they are relatively stable and have a low background. Together with the fact that they are compact and easy to operate, this is what makes the photomultiplier so popular. They are discussed in more detail in Chapter 3.

The Cherenkov effect is used for many purposes, a few of which are listed below [101]:

- Fast counting of charged particles. Because of the short response times (the excited dipoles rapidly decay back to their ground states), high counting rates are possible provided that the Cherenkov light is captured efficiently.
- Velocity measurements of charged particles. Note that $v_{\text{min}} = c/n$ puts a lower limit on the range of velocities. If the mass of the particle is known, the energy of the particle can also be extracted. Ring Imaging Cherenkov Detectors measure the Cherenkov angle, such that using (1.32) the particle velocity can be calculated.
- Neutrino detection. Upon interaction of the neutrino with the dielectric medium, a charged lepton is created according to (1.25)[63]. These leptons in their turn can then be detected through the Cherenkov effect. See *Neutrino detection with a Cherenkov detector*.
- Direction measurements. The Cherenkov cone is very distinct and allows to extract the direction of a charged particle passing through a dielectric medium.

Neutrino detection with a Cherenkov detector

Typical Cherenkov telescopes consist of very large volumes of water or ice[64](refraction index $n \approx 1.34$). The large volume is required to compensate for the extremely low cross-sections for neutrino interactions. The CC interactions of the three neutrino flavors have different experimental signatures in these Cherenkov media, allowing flavor identification [98]. This is shown schematically for water in Figure 1.13.

- An electron produced in interaction (1.25) quickly loses its energy through Brehmsstrahlung emission [82]. The photons decay into e^-e^+ pairs, which in their turn

[63] Similarly for an antineutrino through (1.26).
[64] E.g. IceCube.

again lose energy through Brehmsstrahlung emission. This process is repeated multiple times, creating an electromagnetic shower. As long as the energy is high enough such that the Cherenkov condition is satisfied, these electrons and positrons also emit Cherenkov light. The electromagnetic shower is however contained within a small volume, because the radiation length[65] for electrons (positrons) in water is only 36 cm. The electron is created together with a hadronic cascade or shower. If these hadrons are charged and satisfy the Cherenkov condition, they will also cause Cherenkov light production. This shower also provides a very local signal, as the hadronic interaction length[66] is typically low (about 80 cm in water). An electron neutrino thus only provides a local signal in a Cherenkov detector[67].

– A muon produced in interaction (1.25) loses energy much slower than an electron because the Brehmsstrahlung effect becomes negligible[68]. As mentioned in Section 1.2.2.1, the energy loss of the muon from the Cherenkov process is negligible compared to the energy loss due to ionization. Furthermore, because of its long lifetime and the phenomenon of time dilatation, the muon travels long distances in the detector. A muon thus typically leaves behind a long straight trace in the detector. The angle between the direction of the muon track and the direction of the original muon neutrino decreases from about 9 degrees at 10 GeV to almost 0 degrees at 1 TeV. The change in direction of the muon track due to multiple scattering is negligible (compared to the change in direction between neutrino and muon) at all energies. Reconstruction of the muon track thus gives a good indication of the original neutrino direction.

– A tau lepton produced in interaction (1.25) has a much shorter lifetime than a muon (∼3 ps) and thus has a much shorter track in the Cherenkov medium. It either decays in an electron or muon (each with a branching ratio of about 17% [82]), or hadronically. If the tau lepton decays in a muon, this will again follow a long track in the Cherenkov medium (if energetic enough). Decay in an electron or hadron, again results in a contained shower.

Note from the previous that if only one cascade is observed in the detector, this must either originate from a CC interaction with an electron, or from a NC interaction (Interactions (1.27) and (1.28))[69].

[65] Mean distance after which a particle loses 1/e of its energy by photon emission.
[66] Mean distance after which the number of particles in a bundle is reduced by a factor of 1/e, due to hadronic interactions.
[67] Note that the electromagnetic and hadronic cascade are inseparable.
[68] Due to the muons much higher mass compared to the electron mass.
[69] Assuming that the detector is 100% efficient.

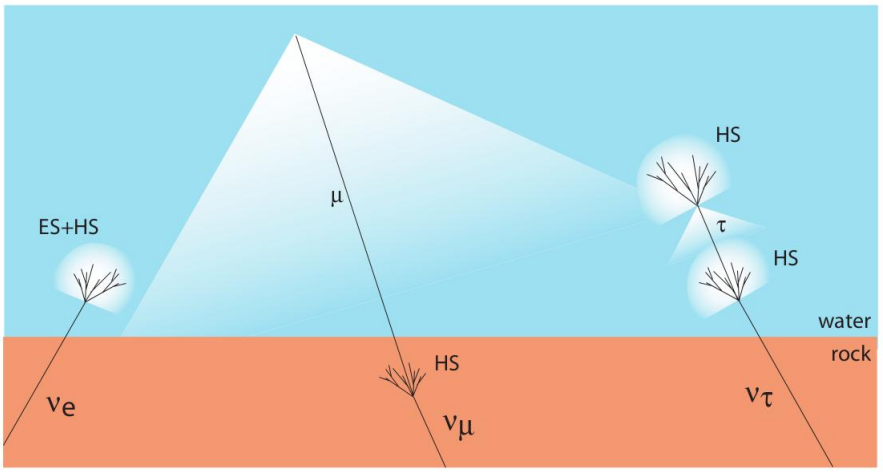

FIGURE 1.13: Schematic view of the different experimental signatures of the three lepton flavors in water. ES and HS stand for electromagnetic shower and hadronic shower respectively [98].

1.3.3 Experimental results and outlook

In Table 1.2, the best-fit values for the mixing angles in the weak sector are listed. There are numerous experiments investigating neutrino oscillations and these can be categorized into four different groups:

- **Solar neutrino experiments** study neutrinos coming from the Sun. The Sun produces electron neutrinos with energies below 20 MeV and the baseline (L in formula (1.16)) is simply the distance between the Sun and the Earth. Above 5 MeV, the oscillations are influenced by the solar matter (MSW effect). Examples of experiments studying solar neutrino oscillations are the Sudbury Neutrino Observatory [102], and the Super-Kamiokande observatory [103].

- **Atmospheric neutrino experiments** study neutrinos coming from the atmosphere. These neutrinos are products of the interaction of cosmic ray particles with the atmosphere, as discussed earlier. Atmospheric muon neutrinos with energies of the order of 1 GeV and more travel through the Earth (baseline) and oscillate. One also looks in the other direction, directly to the neutrinos created in the atmosphere above the detector. The former are long-baseline experiments, while the latter are short-baseline experiments. The Super-Kamiokande experiment provided the first experimental evidence for atmospheric neutrino oscillations in 1998 [57]. The IceCube Neutrino Observatory has announced the first statistically significant ($> 5\sigma$) detection of neutrino oscillations in the high-energy region (20-100 GeV) on May 17, 2013 [104].

– **Reactor neutrino experiments** use neutrinos produced in nuclear reactors to study oscillation phenomena. They produce neutrinos with energies similar to the solar neutrinos and have baselines ranging from a few tens of meters to over 100 km. They usually have a near detector, measuring the interaction rates, and a far detector looking for oscillations. The Daya Bay Reactor Neutrino Experiment studies the disappearance of electron antineutrinos along a baseline of approximately 1 km. In 2012 they announced with a significance of 7.7 standard deviations that the mixing angle θ_{13} has a non-zero value [105][70]. As discussed before, this is necessary in order to have CP violation due to mixing.

– **Beam line neutrino experiments** use neutrinos produced at particle accelerators. Usually muon neutrino beams are generated from pion decay. Just like in reactor neutrino experiments, a near detector controls the neutrino flux, while a far detector searches for signs of oscillations. They typically involve neutrinos of a few GeV of energy and have baselines of several hundred km. In 2010, the first observation of a muon to tau neutrino oscillation was observed at the OPERA detector in Italy, located 730 km away from its neutrino source at CERN in Geneva [107]. The currently-running T2K experiment uses a neutrino beam directed through 295 km of the Earth to measure θ_{13} with more precision [108].

Contrary to situation in the quark sector, mixing in the weak sector is strong. θ_{12} dominates the oscillations in solar and reactor experiments, while θ_{23} dominates in the atmospheric neutrino oscillation experiments.

At present there is no experimental information on the CP violating phases (neither Dirac or Majorana). Knowing that $\theta_{13} \neq 0$, CP violation effects could be seen in oscillation experiments provided that θ_{13} is large enough [82].

The search for the the neutrino masses is done in different ways, all giving complementary information.

– Neutrino oscillation experiments provide a measure for the squared mass differences $\Delta m_{j1} = m_j^2 - m_1^2$ with $j = 1, 2, 3$. The best-fit values for the solar and atmospheric squared mass differences, as reported by Particle Data Group in 2012, are also listed in Table 1.2. It is not possible with the present data to determine the sign of Δm_{atm}, leading to an undetermined neutrino mass hierarchy [82].

– β decay experiments provide direct information on the flavour neutrino masses from the kinematics of weak decays. Based on energy and momentum conservation

[70] Several other experiments did the same in the meantime [106].

only, these searches are model-independent. These flavor masses correspond to the weighted average of the neutrino mass eigenstates contributing to the given flavor

$$m_l^2 = \sum_j m_j^2 |U_{lj}^2|^2. \tag{1.34}$$

The most sensitive direct neutrino mass search is based on the study of the end-point of the electron energy spectrum in tritium β decay. Thus far, an upper limit of 2.05 eV (95% C.L.) is found for electron antineutrinos [109]. The upcoming KATRIN experiment should reach a sensitivity of $m_{\bar{\nu}_e} \approx 0.20$ eV [110]. Searches for the muon (tau) neutrino mass through muon (resp. tau) decay are also done, but have the downside that these neutrinos carry much more energy than the electron neutrinos produced in β decays.

– $0\nu\beta\beta$ decay experiments probe the effective Majorana mass, which is related to the mixing matrix elements and the neutrino mass eigenstates in the following way

$$|\langle m_{\text{eff}}^{\text{Maj}} \rangle| = |\sum_j m_j U_{ej}^2|^2. \tag{1.35}$$

Several experiments have been searching for $0\nu\beta\beta$ decay and many new detectors are under construction, such as the SuperNemo [111] and the MAJORANA experiment [112]. No $0\nu\beta\beta$ events have been observed so far.

– From cosmology, an upper limit on the sum of the neutrino masses can be determined [82]

$$\sum_j m_j < (0.3 - 1.3) \text{ eV (95\% C.L.)}. \tag{1.36}$$

TABLE 1.2: Best-fit values for the mixing angles in the weak sector and for the squared mass differences for the neutrinos measured in solar and atmospheric neutrino oscillation experiments [82].

Parameter	Best-fit value ($\pm 1\sigma$)
$\sin^2\theta_{12}$	$0.312^{+0.018}_{-0.015}$
$\sin^2\theta_{23}$	$0.42^{+0.08}_{-0.03}$
$\sin^2\theta_{13}$	$0.025^{+0.007}_{-0.008}$
Δm^2_{Sun}	$7.58^{+0.22}_{-0.26} \times 10^{-5}$ eV^2
$\lvert\Delta m^2_{\text{atm}}\rvert$	$2.35^{+0.12}_{-0.09} \times 10^{-3}$ eV^2

Chapter 2

The IceCube Neutrino Observatory

The IceCube Neutrino Observatory is a giant neutrino telescope mounted deep into the Antarctic ice at the geographical South Pole. The detector was completed in December 2010. It constitutes of two main parts: the in-ice component consisting of IceCube and DeepCore (Section 2.1), and IceTop located at the surface (Section 2.2). IceCube and DeepCore study extraterrestrial neutrinos with energies down to $\sim$ 100 GeV and $\sim$ 10 GeV respectively, while IceTop studies cosmic rays and also serves as a veto for IceCube.

The IceCube neutrino telescope is a Cherenkov detector (see Section 1.3): it uses the Cherenkov effect to detect neutrinos in IceCube and cosmic ray showers in IceTop. The optical sensors used in IceCube and IceTop are the so-called Digital Optical Module (DOM), discussed in Section 2.3.

Besides studying astrophysical neutrino and cosmic ray sources (see Section 1.2.2.3), IceCube also searches for dark matter (see also Section 1.2.2.2), and studies the neutrino properties itself, such as neutrino oscillations in the atmosphere (see also Section 1.1.4.2). To become sensitive to low-energy neutrinos, an upgrade of the detector is proposed, called PINGU (Section 2.4). This will lower the neutrino energy threshold of the detector down to a few GeV. The research undertaken in this thesis is part of the R&D for PINGU and/or possible future upgrades of the IceCube detector.

2.1 IceCube detector

The IceCube detector consists of one cubic kilometer of ice[1] instrumented with 5160 Digital Optical Modules (DOMs), which detect the Cherenkov light, indirectly caused by the passage of neutrinos through or close to the detector volume (see Section 1.3.2). The DOMs were deployed at depths between 1450 m and 2450 m below the surface, where the ice is very transparent, thus limiting Cherenkov light absorption by the ice. The properties of the ice surrounding the DOMs need to be very well-known, as both absorption and scattering of the Cherenkov photons are significant processes. Note that the 1450 m layer of ice above the detector serves as a background filter for cosmic ray particles coming from above. The IceCube DOMs are attached to 80 strings. The strings are organized on a triangular grid with a spacing of 125 m between adjacent strings. Each string has 60 DOMs, located 17 m apart from each other. A denser instrumented region of 6 strings, called DeepCore, makes up the center of the IceCube array. The DOMs are placed 8 m apart in Deepcore, such that lower energetic neutrinos can also be detected[2]. This is important if one wants to do atmospheric neutrino oscillation measurements in the 10-100 GeV region, as well as for the search for dark matter. Note that IceCube serves as a veto for DeepCore, as high energy signals seen by DeepCore are also seen by IceCube because of their relative geometry. The layout of the IceCube detector is shown in Figure 2.1.

The different topologies for the neutrinos in a large neutrino Cherenkov detector were already discussed in Section 1.3.2. At low energies, there are two basic topologies: long muon tracks ($\sim$ km), originating from CC muon neutrino interactions, and cascades (both electromagnetic and hadronic) from electrons and tau leptons, originating from CC electron and tau neutrino interactions, and all-flavor NC neutrino interactions. At PeV energies, an extra topology arises for tau neutrino CC interactions. The produced tau lepton may now have enough energy to travel a few hundred meters in the ice before decaying. The topology thus consists of a cascade at the tau creation vertex, followed by a detectable tau track, and a second cascade at the tau decay vertex. This topology is called a "double bang".

Figure 2.2 depicts the interaction of a muon neutrino in ice, causing signals in several adjacent DOMs. The time of arrival of the detected photons depends on the position of each DOM relative to the muon's path. Both the intensity and time of arrival of the Cherenkov light are used to reconstruct the track of the muon (or any other charged

[1] Note that the effective volume of the detector is larger than the active volume since neutrinos interacting close to the detector volume may also be detected.

[2] The lower the energy of the neutrino, the lower the energy of the corresponding charged lepton after interaction with the ice. The charged lepton will thus travel a shorter distance in the detector, causing less Cherenkov light emission.

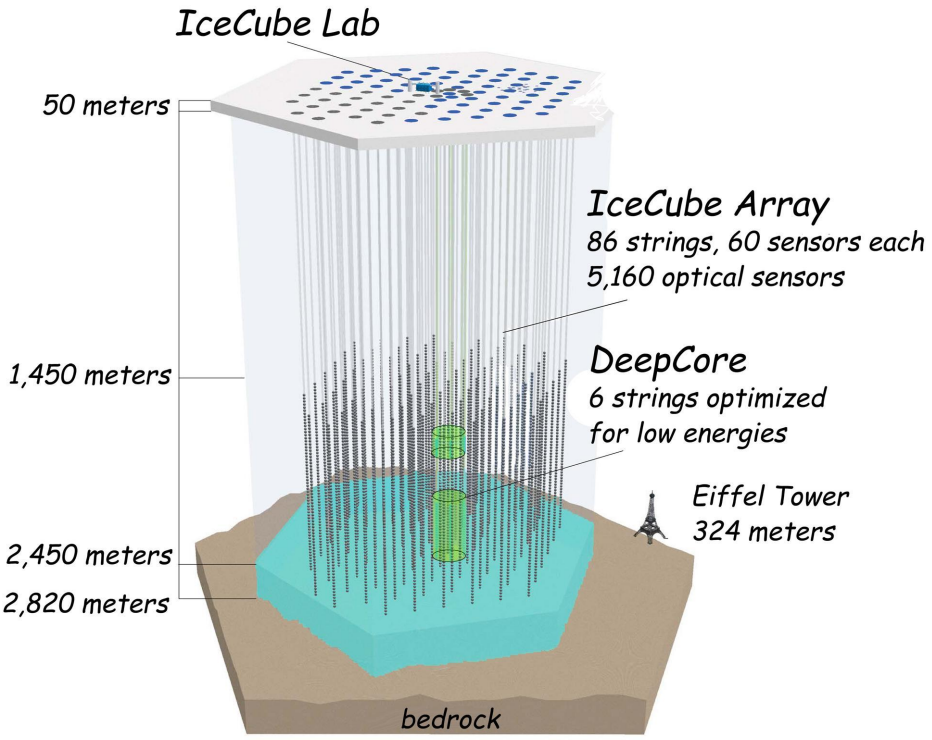

FIGURE 2.1: Drawing of the IceCube Neutrino Observatory showing its main parts IceTop, IceCube, and DeepCore [113].

particle causing Cherenkov light). These tracks are then used to extract information on the energy and direction of the original neutrino. Figure 2.3 shows the topology of three events in IceCube, one for each neutrino flavor. Each sphere represents a DOM which detected a Cherenkov signal. The color refers to the time of the firing of the DOM (from red to blue with increasing time), while the size of the sphere refers to the magnitude of the detected signal.

2.2 IceTop detector

IceTop is the surface component of the IceCube Neutrino observatory. It covers one square kilometer of surface area above the IceCube detector. IceTop is both a cosmic ray shower detector and a veto detector for IceCube. To achieve these goals it relies on the same detection principles as the IceCube detector. 81 stations are placed on the same triangular grid as the IceCube strings (Figure 2.4(a)). Each station contains two cylindrical tanks placed at a distance of 10 m from each other. The layout of an IceTop tank is shown in Figure 2.4(b). A tank consists of two DOMs embedded in an ice layer. One DOM is operated at high gain (HG), while the other is operated at low gain (LG),

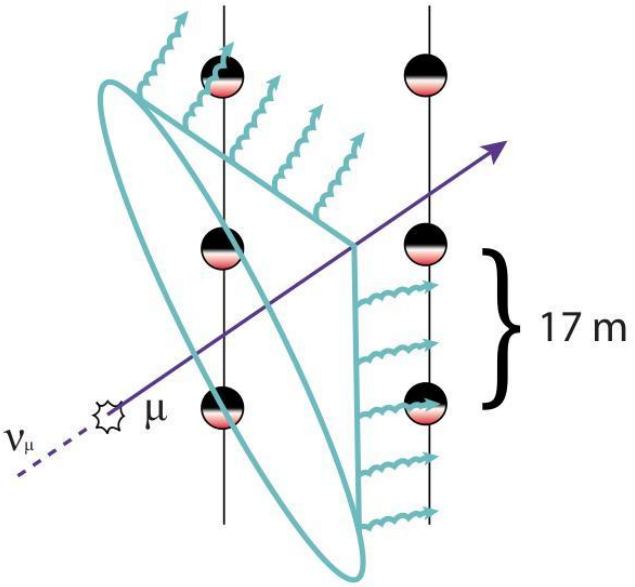

FIGURE 2.2: Drawing of a muon neutrino interaction in IceCube [113].

in order to enhance the dynamic range of the detector[3]. The inner surface of the tank is coated with a diffusive reflecting layer such that the Cherenkov light produced by cosmic ray particles crossing the tank is reflected towards the two DOMs.

Neutrinos produced in extensive air showers (see Section 1.2.2.1) constitute a large background for the IceCube detector, as they can mimic a signal of a cosmic neutrino. IceTop's ability to detect these air showers provides a way to get rid of this background. Apart from this veto function, the IceTop array also studies the intrinsic properties of the air showers, such as the composition of the shower [116].

2.3 Digital Optical Module

2.3.1 General description of a DOM

The DOM is the optical sensor used in IceCube, DeepCore, and IceTop for both the detection of Cherenkov light and the subsequent data acquisition [117]. A schematic view of a DOM is displayed in Figure 2.5. The active component of a DOM is a 25 cm diameter photomultiplier tube (PMT). A general discussion of PMTs is done in the next subsection. The PMT collects Cherenkov photons and converts this light signal into an electrical signal through the photoelectric effect. The DOM also contains the

[3]This refers to the gain of the photomultiplier tube inside the DOM. See Section 2.3.1 for a discussion on the DOM, and Section 2.3.2 for a general discussion on photomultiplier tubes.

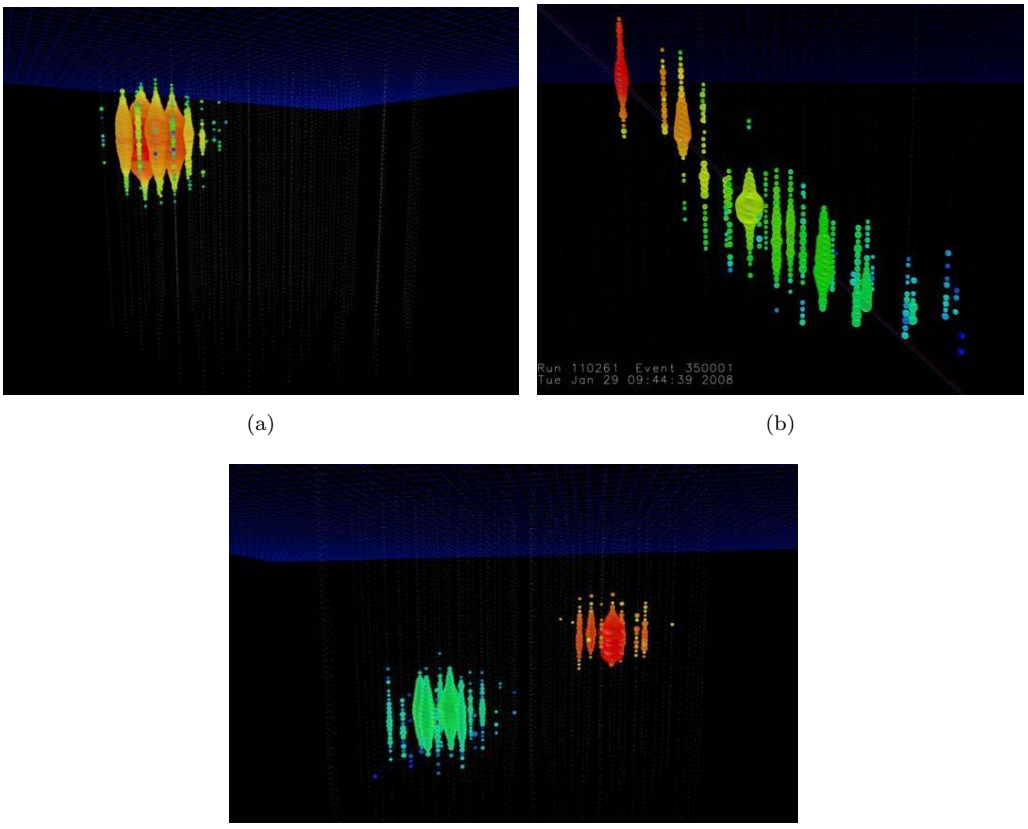

(a) (b)

(c)

FIGURE 2.3: (a) Simulated cascade signal of a ν_e [114]. (b) Measured track-like signal of a muon (or bundle of muons) [114]. (c) Simulated "double bang" signature of a high-energy tau neutrino [114].

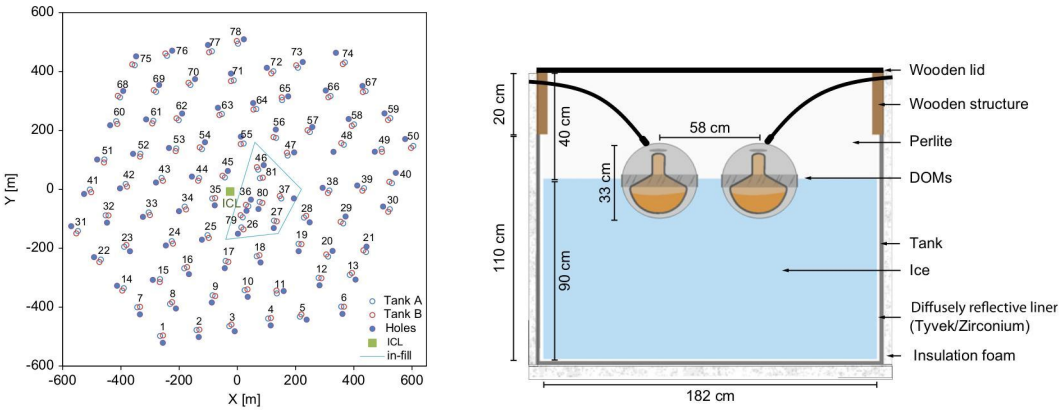

(a) (b)

FIGURE 2.4: (a) Configuration of the IceTop tanks [115]. (b) Layout of an IceTop tank, containing two DOMs embedded in an ice layer [115].

high voltage generator and divider circuit for the PMT, and the electronics to process and digitize the recorded signal. The link between the modules in the ice and the surface of the detector for both power supply and data transfer is provided by copper twisted-pair wires. The PMT is surrounded by a mu-metal grid to shield it from the terrestrial magnetic field. A LED[4] flasher board is present in every DOM for calibration purposes and to study the properties of the surrounding ice. All of this is housed within a 35.6 cm diameter pressure sphere made of glass. An optical gel is used to optimize the light coupling between the PMT and this glass sphere. The glass and gel together induce a short-wavelength cut-off of the DOM at 350 nm.

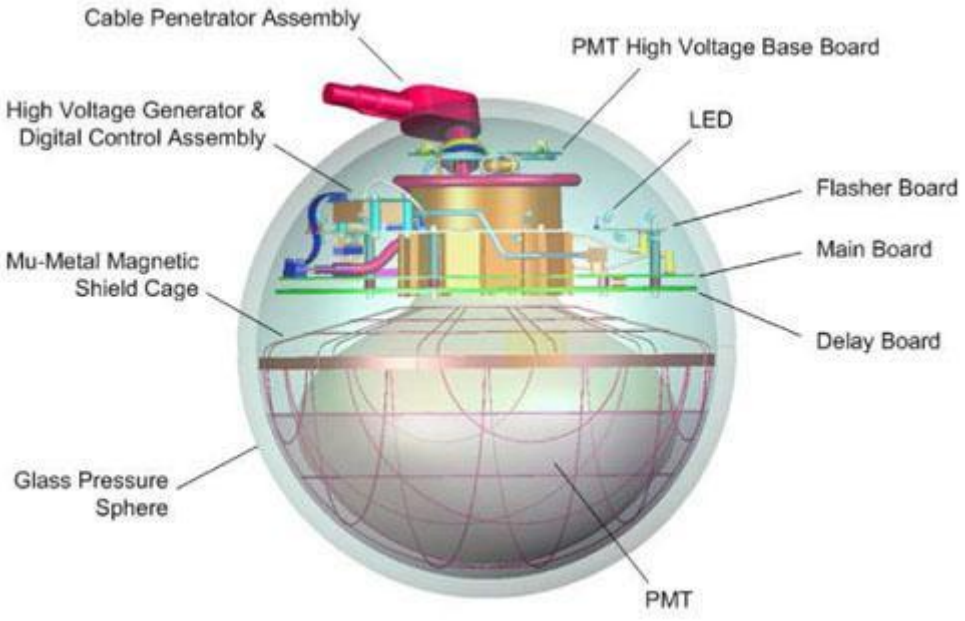

FIGURE 2.5: Schematic view of a DOM [113].

2.3.2 Photomultiplier tubes

PMTs are devices which convert a collected light signal into an electrical signal by means of the photoelectric effect. The created electrical signal is then multiplied using an internal multiplication stage, to provide useful electrical output signals.

Figure 2.6 sketches the working principle of a PMT. Photons enter the vacuum tube through a glass window[5] and strike a thin photocathode, coated on the inside of the PMT window. At low enough energies (below ∼100 keV, corresponding to wavelengths above

[4] Light-emitting diode.

[5] Depending on the wavelength range of interest, different window materials are used. Borosilicate glass is opaque for photons with $\lambda \lesssim 270$ nm. This UV cut-off is lowered to 115 nm by using a magnesium fluoride window.

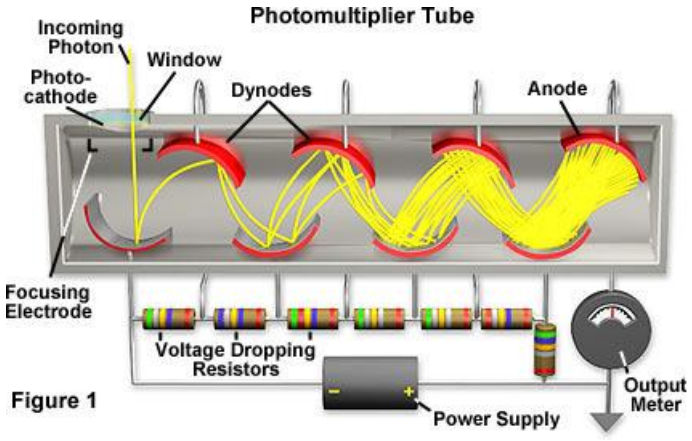

FIGURE 2.6: Basic configuration of a photomultiplier: conversion of a light signal into an electrical signal using a photocathode and multiplication dynodes [118].

$\sim$0.01 nm[6]) the photons interact with the cathode through the photoelectric effect [82]. They transmit their energy to electrons (e.g. 3 eV for blue photons), which then lose part of this energy in collisions with other electrons in the cathode. Arriving at the cathode surface they may escape if they still have sufficient energy to overcome the work function[7] W

$$E_{e^-}^{\text{esc}} = h\nu - W - \Delta E_{\text{coll}}, \tag{2.1}$$

where $E_{e^-}^{\text{esc}}$ is the escape energy of the photoelectron, $h\nu$ is the energy of the photon, and ΔE_{coll} is the energy loss due to collisions. This work function causes a low-energy cut-off (high wavelength cut-off), typically in the red to near-infrared part of the spectrum. The probability for a photon with wavelength λ to eject an electron, also called a photoelectron, at the photocathode is given by the quantum efficiency $QE(\lambda)$.

$$QE = \frac{\text{number of photoelectrons emitted}}{\text{number of incident photons}}. \tag{2.2}$$

It is typically around 20%, but depends highly on the cathode thickness due to two competing processes. Increasing the photocathode thickness increases the photon capture probability, but decreases the fraction of electrons reaching and escaping the surface. A uniform cathode surface thickness is thus very important for large cathodes.

The photoelectrons leave the cathode with an energy of 1 eV or less and are accelerated towards an electrode at higher voltage V_{d1}, the first dynode. During this acceleration they gain an energy of $\Delta E = e\Delta V = e(V_{d1} - V_c)$, where V_c is the cathode voltage. To increase the number of photoelectrons hitting the first dynode, independently of the

[6] As mentioned in Section 1.3.2, the Cherenkov spectrum is situated in the visible part of the electromagnetic spectrum and is thus seen by a PMT photocathode.

[7] The energy needed to remove an electron from the bulk of the material to a point located immediately outside the material on the size scale of the solid, but far away at an atomic scale.

position of emission at the cathode, and to limit the spread in time between those electrons emerging from different points of the cathode surface, a specially designed electrode configuration is used in this first stage of the phototube. Striking the surface of this dynode, the energy of the photoelectron is absorbed in a similar fashion to the photon absorption in the photocathode, but now each electron may release several secondary electrons. Every photoelectron creates approximately $e\Delta V/(E_g + E_{e^-}^{\text{esc}})$ secondary electrons in the dynode, where E_g is the bandgap energy of the dynode material. However, just like in the cathode, many of those electrons will not reach the dynode surface, let alone escape from it. The secondary electrons that do escape are then accelerated towards a second dynode at voltage $V_{d2} = 2V_{d1}$, causing a further increase of the number of electrons. This multiplication process continues until the last dynode, the anode, where the electrons are collected and an output pulse is generated. As shown in Figure 2.6, the dynode voltages are derived from one high voltage using a resistor dynode chain. The vacuum inside the tube ensures an efficient acceleration and furthermore prevents contamination of the photocathode.

The overall multiplication factor δ for a single dynode is given by

$$\delta = \frac{\text{number of secondary electrons emitted}}{\text{primary incident electrons}}. \tag{2.3}$$

Incident electrons with a high energy may create more secondary electrons, but also have a longer penetration depth in the dynode, causing the secondary electrons to lose more energy on their way out of the dynode. Low-energy electrons have smaller penetration depths, but create less electrons. Note that this energy dependence thus implies a voltage dependence for δ.

The overall gain G of a PMT with N dynodes can be written as

$$G = \alpha\delta^N, \tag{2.4}$$

where α is the fraction of photoelectrons collected by the multiplier structure. A good designed first stage of the PMT should give α close to 1. Typical PMTs have around 10 stages and a multiplication factor δ of 5, thus giving rise to a gain $G \approx 10^7$. The overall gain highly depends on the applied high voltage through its proportionality to δ^N.

The emission of the secondary electrons is a statistical process. The multiplication factor δ fluctuates around a mean value. This implies that output signals originating from one photoelectron at the cathode do not always have the same amplitude. The variation in the number of produced secondary electrons becomes less important further in the multiplication stage, as those dynodes are struck by many electrons such that the variations will average out. The gain variation at the first dynode may vary considerably

since the number of photoelectrons emitted by the cathode can be very small[8]. There is no universally applicable statistical description of the fluctuation in δ, but a simple picture follows from assuming a Poisson distribution around the average yield n for a dynode

$$P(m;n) = \frac{n^m e^{-n}}{m!}, \tag{2.5}$$

where m is the number of secondary electrons. The relative standard deviation, given by $\sigma_n/n = \sqrt{n}/n = 1/\sqrt{n}$, decreases with increasing n. As a consequence, a PMT with a high gain first dynode may show different peaks in its pulse height spectrum[9] corresponding to 1, 2, etc. photoelectrons produced at the first dynode. This is illustrated in Figure 2.7(a). The single photoelectron (SPE) peak is clearly distinguishable from the other peaks, most importantly from the noise peak. The noise peak represents the dark current, i.e. the signal produced at the anode when no light input is present at the cathode. Thermionic emission is an important contributor to the noise. Because of the low work functions for the PMT electrode materials, thermal excitations can occur. When this happens at the dynodes, they will generate an output signal which is smaller than a SPE signal. If thermionic emission happens at the photocathode, the created signal will be indistinguishable from a real SPE signal. In experiments where one is only interested in large signals, the dark noise peak can be easily cut-off by setting a voltage threshold. If the SPE peak is important one cannot carelessly use a voltage threshold to get rid of the noise, as this might also cut away part of the SPE peak. Other measures, like choosing the appropriate cathode material, reducing the cathode surface, and cooling the cathode may be applied. At room temperature, thermionic emission rates are of the order 100 electrons per cm^2 per s. Examples of other contributors to the dark current are radioactivity of the PMT materials, cosmic ray particles hitting the PMT electrodes (typically high PE signals, but at a low rate), and electrons escaping from the electrodes through quantum tunnelling[10].

The individual photoelectrons and secondary electrons travel along slightly different paths between the dynodes, causing a small spread in time of the order of 20 ns between the arrival of the first electron and the last electron at the anode. This transit time spread is the most important timing characteristic for a PMT. The average transit time (typically 20-80 ns) only causes a fixed delay, and the process of photoemission in the cathode and secondary emission in the dynodes takes only a fraction of the transit time ($\sim$0.1 ns). A typical output pulse of a PMT is shown in Figure 2.7(b). The output pulse is characterized by three parameters:

[8] This is especially true for Cherenkov counting, where a typical Cherenkov signal only gives rise to a few photoelectrons.

[9] This is obtained by integrating the output pulses. See also Chapter 5.

[10] The electron tunnels through the energy barrier rather than surpassing it through thermal excitation.

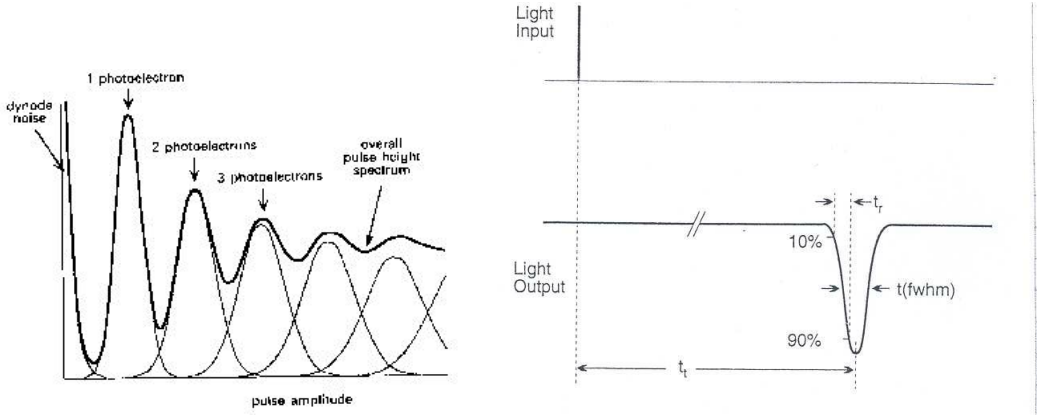

(a) (b)

FIGURE 2.7: (a) Pulse height spectrum for input signals causing different numbers of photoelectrons. The first dynode has a gain of 25 [119]. (b) Timing properties of a PMT signal [120].

- The rise time t_r corresponding to the time needed for the pulse to go from 10% to 90% of its amplitude.
- The time t(FWHM) corresponding to the full pulse width at half maximum.
- The transit time t_t corresponding to the time between the impact of the photon signal on the photocathode and the time at which the pulse reaches its maximum height.

Characteristics of the IceCube PMT

The PMTs used in the IceCube DOMs are of the type R7081-02, manufactured by Hamamatsu Photonics [121]. It is a 10-stage PMT with a bialkali photocathode. The PMT window is made of borosilicate glass. The quantum efficiency of the R7081-02 is displayed in Figure 2.8. A maximum QE of approximately 25% is reached at 420 nm. The R7081-02 has an anode pulse rise time of 4.2 ns, an electron transit time of 60 ns, and a spread on this transit time of 3.2 ns.

2.4 PINGU

In order to increase the sensitivity of the IceCube detector in the low GeV energy regime, a further increase in module density of the central region of the IceCube array is proposed, called the Precision IceCube Next Generation Upgrade (PINGU). The preparations for this upgrade are still in a very early stage, and one aims to complete

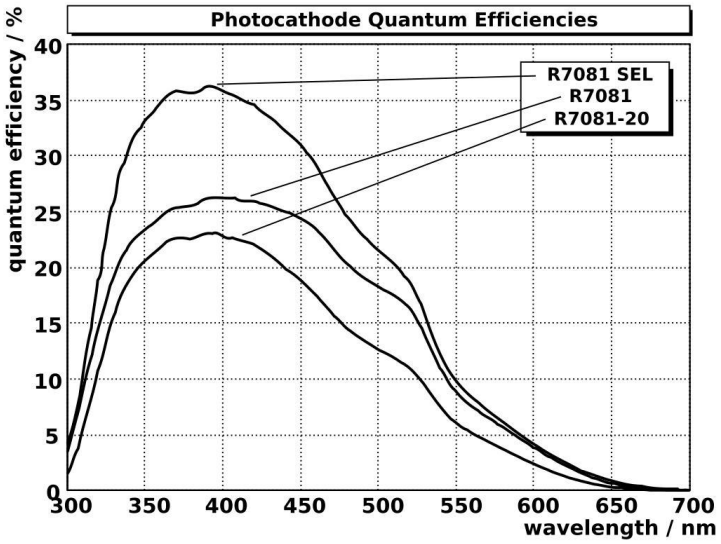

FIGURE 2.8: Quantum efficiency curve of the R7081-02 PMT used in the IceCube DOMs (middle curve) [122].

the detector upgrade by early 2018. Several distinct detector geometries with either 20 or 40 additional strings of optical sensors are currently being investigated. Similar to IceCube acting as a veto for DeepCore, both IceCube and DeepCore will act as a veto for PINGU.

The physics goals of PINGU include the determination of the neutrino mass hierarchy by looking at atmospheric neutrino oscillations in the 5-15 GeV region, observing tau neutrino appearance (see Section 1.1.4.2), and a search for low-mass dark matter particles (WIMPS, see Section 1.2.2.2). PINGU will also be used for the R&D of a possible subsequent detector upgrade, MICA (Multi-megaton Ice Cherenkov Array), for which the energy threshold will be lowered to a few tens of MeV by further increasing the module density. Low-energy neutrinos from supernovae should then also become visible for the IceCube Neutrino Observatory.

PINGU R&D: Wavelength-shifting Optical Module

An optical sensor for low-energy neutrino detection ($\sim$ 1 GeV) in the Antarctic ice should satisfy two very important requirements:

- A large photosensitive area, in order to detect as many Cherenkov photons as possible (smaller signals).
- A low noise rate, to get the lowest possible energy threshold and a good energy resolution.

Just like a DOM, such a module needs to be robust against the high pressures ($\sim$ kbar) and low temperatures ($\sim$-30°C) present in the ice.

One of the proposals for a new Cherenkov detector module is the Wavelength-shifting Optical Module or WOM[11]. A WOM uses a wavelength shifter (WLS) as the active part for the photon collection. A WLS absorbs the Cherenkov light photons and isotropically re-emits photons with a shorter wavelength. By choosing the appropriate WLS geometry, it can efficiently guide the re-emitted photons to a readout surface through the process of total internal reflection, where a conventional PMT converts the light into an electrical signal. Separating the light-collection process from the light-conversion process allows to use much smaller PMT photocathodes than the ones used in the IceCube DOM. This could lower the noise rate significantly. Downside of this approach is that the light-guiding between WLS light-collection and PMT light-conversion provides an additional source of losses not present in the IceCube DOM.

The physics of a WLS and its possible use for Cherenkov light detection is the topic of the subsequent chapters of this thesis.

[11] Proposed by Sebastian Böser, Marek Kowalski, Lukas Schulte, and Markus Voge from the Physikalisches Institut, Universität Bonn, and Lutz Köpke from ETAP, Universität Mainz [123].

Chapter 3

Detecting Cherenkov light using a WLS

The goal of this master thesis research was to design and construct a working experimental setup to test the feasibility of using wavelength shifting materials as the active part of a Cherenkov detector. This is part of the R&D for PINGU and future extensions of the IceCube detector.

In the first subsection of Section 3.1, the detection principle of the constructed Cherenkov detector is discussed in general, while the subsequent subsections deal with the physics happening in the different parts of the detector. Section 3.1.4 discusses the choice of detector parts and materials used in this experiment.

The readout of the detector is explained in Section 3.2. In the final section, the measurements that were done are listed briefly. Chapter 5 addresses these measurements in more detail together with the results.

3.1 Experimental setup

3.1.1 Detection principle

Figure 3.1 shows the detector together with its readout electronics. A drawing of the setup is displayed in Figure 3.2. The detector has two major parts: the muon trigger and the water tank, in which a wavelength shifter (WLS) is placed. The muon trigger consists of two planes, located above and below the water tank respectively, which register the atmospheric muon flux that causes the Cherenkov light production in the water. Each trigger plane has 8 plastic scintillators read out by a PMT. The principle of using

scintillators together with PMTs to count particles is called scintillation counting (see Section 3.1.2). The wavelength shifter serves as the active component of the detector, catching the Cherenkov photons and guiding them to the readout PMTs W1 and W2 (see Section 3.1.3). The passage of a muon through the setup, causing a WLS signal (firing of PMT W1, W2, or both) together with the firing of the muon trigger, is what we call a signal event.

FIGURE 3.1: Picture of the Cherenkov detector (on the left) together with the readout electronics (on the right). The water tank is empty and opened to show the positioning of the wavelength shifter inside. Two bins containing the trigger scintillation counters are placed above and below the watertank.

3.1.2 Muon trigger

Figure 3.3(a) shows two individual scintillators. Each scintillator has 4 equidistant grooves along its length, in which optical fibers are glued. The scintillators are then separately wrapped in a reflective foil in order to limit light losses at their surface, thus increasing the sensitivity of the trigger at lower muon energies. They are placed next to each other in the trigger bin, where they are each connected to a PMT. The 4 fibers are bent such that they converge at the cathode of the PMT (Figures 3.3(b) and 3.3(c)). Where needed, the two trigger bins were taped to ensure they are lightproof. A drawing of the top view of a trigger plane is given in Figure 3.3(d).

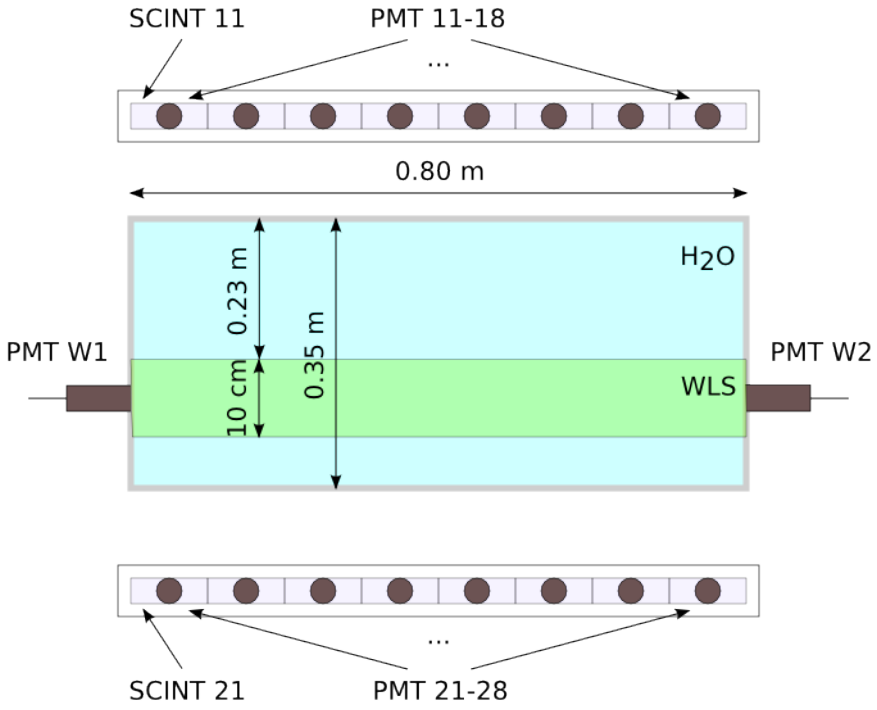

(a)

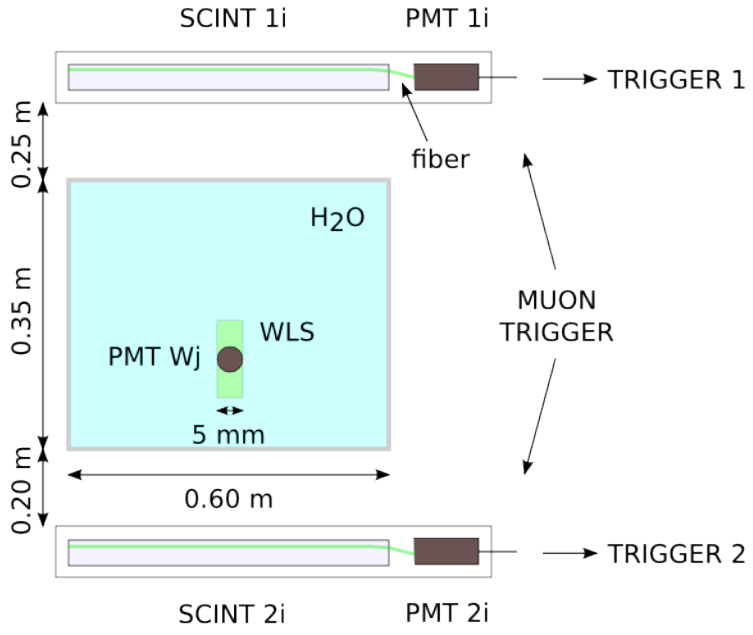

(b)

FIGURE 3.2: (a) Front view of the experimental setup. (b) Side view of the experimental setup. These figures are not drawn to scale. $i = 1$ to 8 refers to the index of the scintillators and PMTs in the trigger planes. $j = 1, 2$ refers to the index of the WLS PMTs.

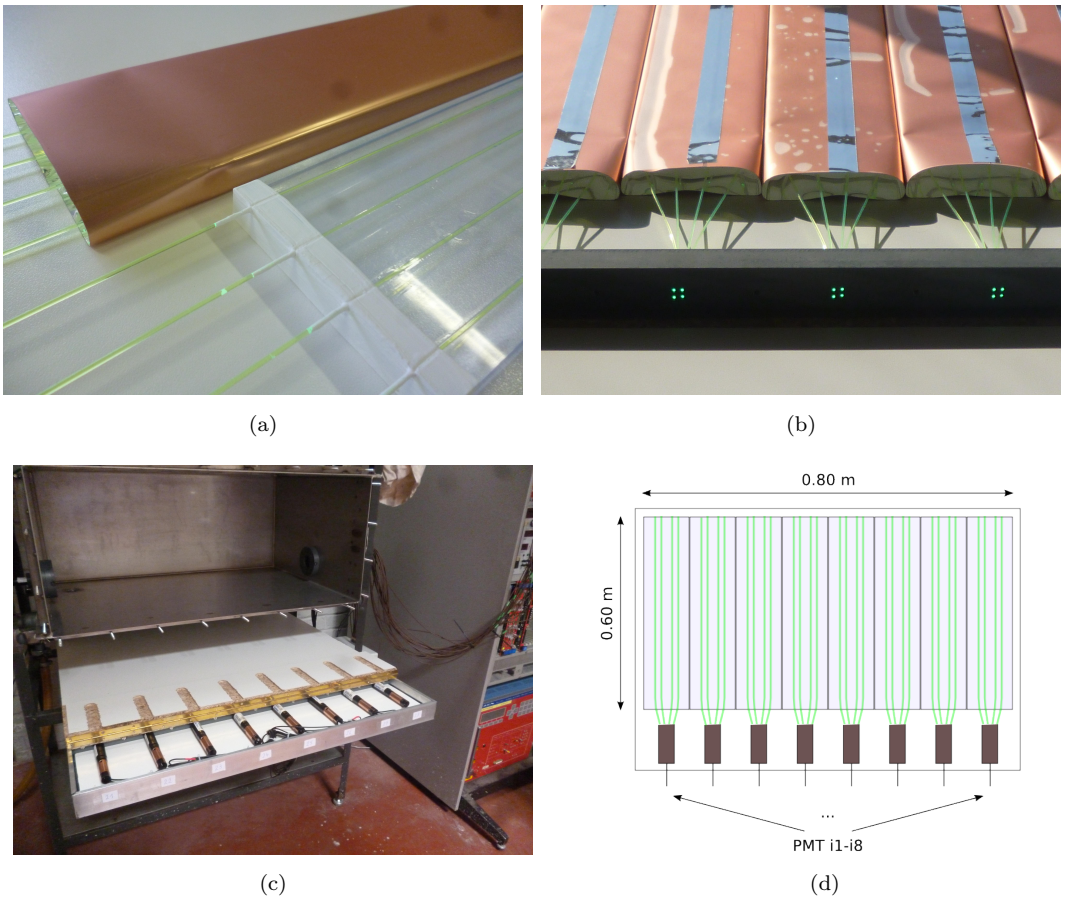

FIGURE 3.3: (a) Scintillator of type BC-482A, with light guides incorporated. (b) The light guides are bent together such that they direct the scintillation light on the PMT cathode. (c) PMTs in the lowest muon trigger plane. (d) Drawing of the top view of a muon trigger plane. $i = 1, 2$ refers to the index of the trigger plane.

3.1.2.1 Scintillation counting

Figure 3.4 shows the basic assembly of a scintillation counter. A scintillator converts particle energy into a light signal which is then collected and guided by a light guide to the photomultiplier, which converts the light signal into an electrical signal.

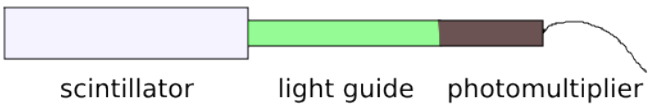

FIGURE 3.4: Basic assembly of a scintillation counter. Based on drawing from [119].

Scintillators

Scintillation light is a collective term for fast light pulses emitted by atoms or molecules of a medium decaying back to a lower energy state after being excited by the passage of an ionizing particle. These ionizing particles are mostly charged particles, but could also be neutral ones, such as photons, if they are energetic enough. There are however many competing non-radiative processes to release the excess energy, which thus decreases the scintillation efficiency of the medium. Examples of such de-excitation processes are lattice vibrations for atoms in a crystal lattice, and vibrational or rotational excitations for atoms in molecules. Scintillation is also referred to as prompt or fast fluorescence.

A scintillator is mainly characterized by [119, 124]:

- the light yield: this is the fraction of the absorbed energy converted into photon energy. This should be as high as possible. Noble gasses are an example of a medium with very high light yield. Excitation only happens at the atomic level, such that in the end (even if energy is exchanged between atoms due to collisions) the excess energy is emitted again by radiative decay.
- the absorption and emission spectrum: the overlap between both spectra should be as small as possible in order to limit self-absorption (see Figure 3.5(a)). This immediately eliminates noble gasses as practical scintillators as they need to be fairly dilute in order to be transparent for their own scintillation light. However, this also means that only few charged particles will cause excitation and thus scintillation. An ideal scintillator has no self-absorption, which is the basic property of wavelength shifters (see Section 3.1.3). Note that the emission is isotropic.
- the signal linearity: this is important in calorimeters where scintillators are used to completely stop the ionizing particles. The light output should then be proportional to the energy loss in the scintillator (described by Birks' rule [125]).
- the pulse shape: fast rise and decay times are typically important in scintillation counters, in order to have small dead-times and thus high counting efficiency. The pulse shape is shown in Figure 3.5(b) and is described by

$$I(t) = I_0 \left(e^{-\frac{t}{\tau_f}} - e^{-\frac{t}{\tau_r}} \right), \tag{3.1}$$

  where τ_r and τ_f are the rise and fall (or decay) time respectively. Typical decay times are of the order of a few nanoseconds to a few microseconds.

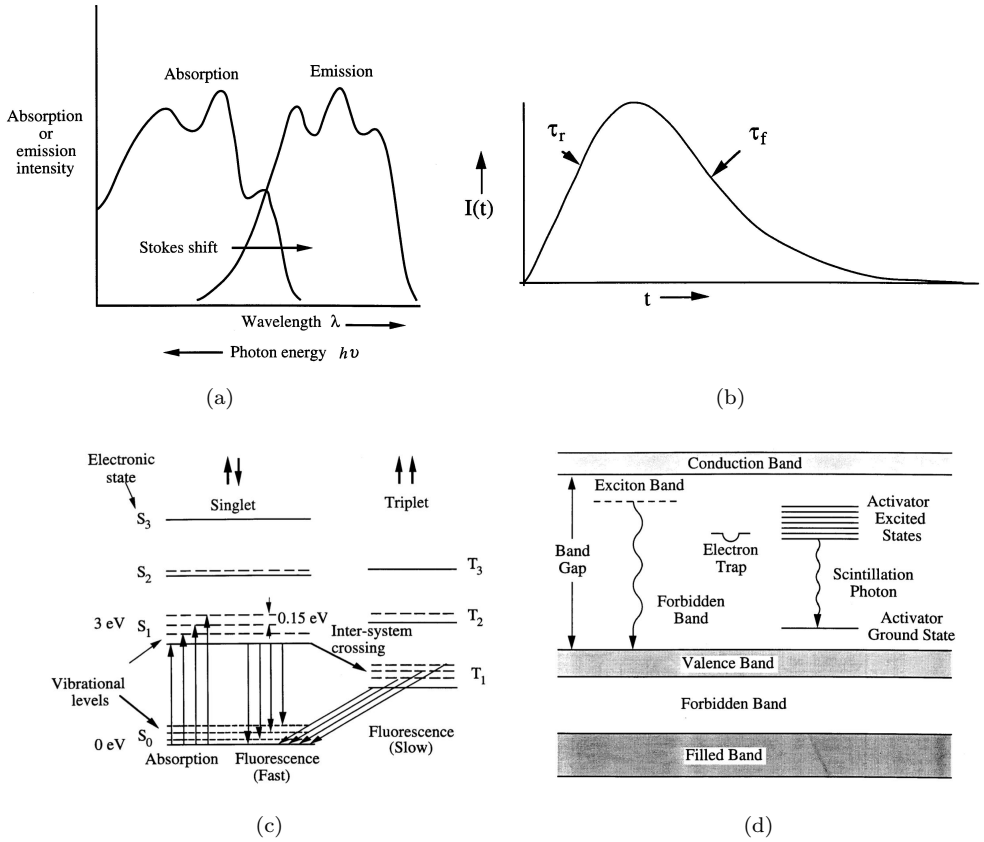

FIGURE 3.5: (a) Pulse shape of scintillation light [124]. (b) Stoke shift for a scintillator [124]. (c) De-excitation in an organic molecule causing scintillation light [126]. (d) De-excitation in an inorganic crystal causing scintillation light [126].

In practice, there are two types of scintillators: organic and inorganic phosphors.

In *organic phosphors*, scintillation is caused by excitation and de-excitation of molecular energy levels (Figure 3.5(c)). In the scintillation process of organic materials, also non-radiative processes are involved causing the energy of the emitted scintillation light to be lower than the absorbed energy (Stokes' shift). This means that their is only little self-absorption. Many scintillation counters make use of plastic scintillators, which are made of scintillating organic molecules.

In *inorganic phosphors* the scintillation process is a consequence of the interaction with the crystal as a whole (Figure 3.5(d)). By adding the appropriate impurities to the material, and hereby causing energy levels in the forbidden zone between valence and conduction band, the excited electrons may be captured by one of these levels. Scintillation occurs if the subsequent transition from the impurity level to the valence band happens by photon emission. Such impurity levels are called luminescence centres. Because the photon energy is typically much lower than the band gap energy, self-absorption by electron-hole production is very low.

If the impurity is metastable, it will capture the electron for a while, causing delayed scintillation (if the transition happens radiatively). Quenching centres are those impurities that cause non-radiative de-excitations.

Organic scintillators are typically faster than inorganic ones. The inorganic scintillators generally have higher yields and better linearity.

For the scintillation counters in trigger 1 and 2 (16 in total) we used organic scintillators of the type IHEP_SC-201, manufactured by SRC IHEP, with dimensions of 10 cm × 60 cm × 2 cm. They have a light yield of about 50%, a decay time of approximately 2.4 ns, an attenuation length[1] of 2 m, and a maximum emission wavelength of 420 nm [127].

Photomultiplier tubes

The light output signals of the scintillators need to be converted into electrical signals such that they can be registered electronically. This is done by photomultiplier tubes (see Sect 2.3.2).

The PMTs used in this experiment are of the type XP1911/UV, manufactured by Photonis [128]. UV refers to the ultraviolet sensitivity of the PMT. It is a 10-stage PMT with a bialkali photocathode with a diameter of 15 mm. The anode pulses have a rise time of 2.3 ns and a FWHM value of 3.5 ns. The transit-time spread is 1 ns. The radiant sensitivity Sk_e of the cathode and the gain curve of this PMT are displayed in Figure 3.6. The cathode radiant sensitivity is the photocathode current produced in response to a given incident light power at a certain wavelength. It is related to the quantum efficiency QE by

$$QE[\%] = \frac{124}{\lambda\,[nm]} \times Sk_e \left[\frac{mA}{W}\right]. \tag{3.2}$$

Light guides

Because the emission process in the scintillator happens isotropically, a lot of the photons will not be caught by the photomultiplier, as PMTs typically do not cover the whole scintillator surface, or cannot be coupled directly to the scintillator because of practical reasons. In order to guide the scintillation light to the PMT cathode optical fibers are typically used. These are parallel-sided blocks of transparent materials (plastic)

[1] Mean distance travelled by a photon in the scintillator after which the probability has dropped to 1/e that it has not been absorbed.

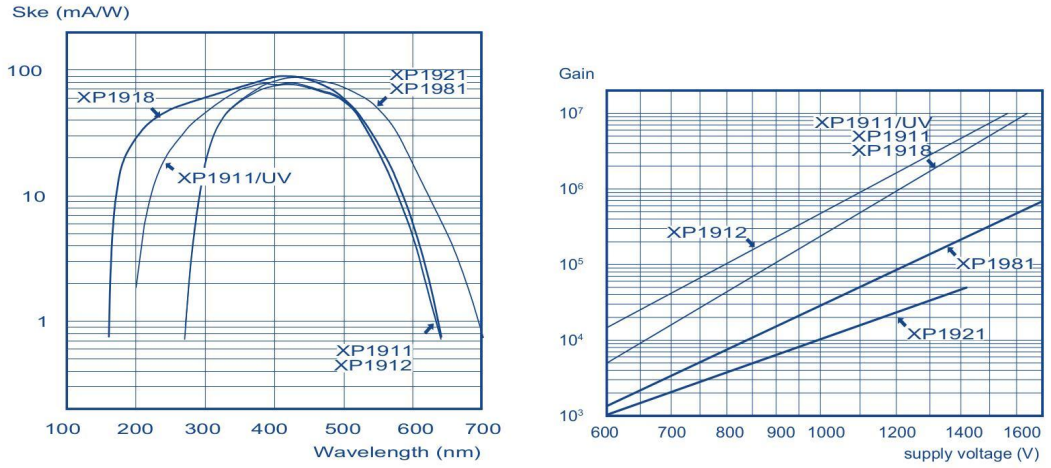

(a) (b)

FIGURE 3.6: (a) Radiant sensitivity of the XP1911/UV photocathode [128]. (b) Gain curve of the XP1911/UV PMT [128].

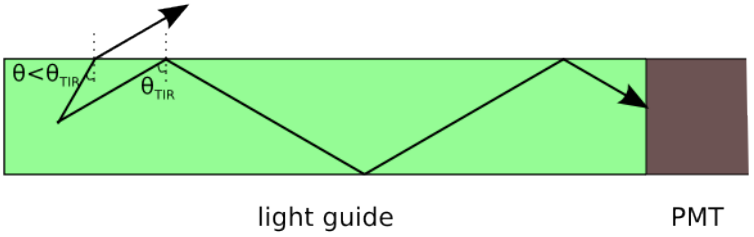

FIGURE 3.7: Principle of total internal reflection. Based on drawing from [119].

which rely on total internal reflection to transport the photons towards the PMTs (see Figure 3.7). The condition for total internal reflection is that the angle of incidence θ for the photons is larger than the critical angle θ_{TIR} for which

$$\sin\theta_{\mathrm{TIR}} = \frac{n_2}{n_1}, \tag{3.3}$$

where n_1 and n_2 are the refractive index of the optical fiber material and external medium respectively. Photons which do not satisfy this condition will eventually escape the optical fiber.

The optical fibers used in this setup are of the type BCF-91A, produced by Saint-Gobain Crystals [129].

3.1.3 Wavelength shifter

A wavelength shifting bar or wavelength shifter is a plastic scintillator doped with specific organic wavelength shifting molecules. The difference with a plain scintillator is that

the overlap between absorption and emission curve is much smaller, hereby lowering self-absorption and thus increasing the light-collection efficiency. The light yield (or quantum efficiency of the re-emission process) depends on the amount of doping. Just like for a plain scintillator, the light emission is isotropic.

The two major advantages of using a WLS as the active component of a Cherenkov detector are the following:

- Its ability to shift the absorbed Cherenkov photons to a higher wavelength better suited for PMT readout.
- Using the WLS as the light collector separates the light-collection process from the light-conversion process, opposed to the situation in an IceCube DOM where both of this is done by the photocathode (see Section 2.3). Because a WLS can be made in different sizes and shapes, this allows to couple to PMTs with small photocathodes, and hence limit the noise rates[2]. This is a very important feature for low-energy neutrino detection.

  Note that a larger active surface does not necessarily imply a higher collecting efficiency, as the photons still need to reach the PMT for readout after they have been collected. Refraction losses at the surfaces (when the condition for total internal reflection in the WLS is not fulfilled), decrease the efficiency. A reflective coating on the non-readout surfaces of the WLS and/or an appropriate WLS geometry could limit those losses.

  Separating light-collection and light-conversion also allows to design a module which is sensitivity to the full 4π solid angle, opposed to the 2π solid angle for the current DOMs used in IceCube.

The wavelength shifter used in this setup is of the type BC-482A with dimensions 10 cm $\times$ 0.5 cm $\times$ 80 cm, produced by Saint-Gobain Crystals [130][3]. The decay time provided by Saint-Gobain is 12 ns. The people from the Physikalishes Institut in Bonn measured a decay time of 8.5 ns for a EJ-280 WLS, which is equivalent to the BC-482A WLS. A ray tracing simulation of the photons inside the WLS showed that the timing resolution of the BC-482A is mostly dominated by the fluorescence emission process [123]. The absorption and emission spectrum as specified by the manufacturer are given in Figure 3.8[4].

[2]The noise rate for a DOM is of the order of 500 Hz at -30°C, which could be reduced to a noise rate of the order of 1 Hz per kg WLS material by using a WLS as light-collector [123].

[3]Borrowed from the Physikalisches Institut, Universität Bonn.

[4]Note that this WLS is made of the same material as the optical fibers.

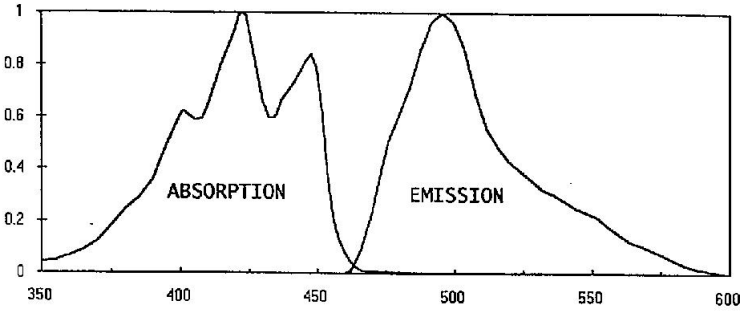

FIGURE 3.8: Absorption and emission spectrum as specified by Saint-Gobain Crystals [130]. The horizontal axis shows the wavelength in nm, while the vertical axis is expressed in arbitrary units.

The fluorescence re-emission photons of the WLS reach the two PMTs, PMTW1 and PMTW2, placed at both ends of the WLS bar (see Figure 3.2), through total internal reflection. No measures are taken in this setup to limit the refraction losses at the WLS surface.

The two WLS PMTs only cover 1/10th of the readout surfaces of the WLS. They are seperated from the WLS by a perspex window to avoid direct contact of the PMTs with the water in the water tank. To optimize the light coupling between WLS, perspex window, and PMT an optical coupling gel is used. The WLS readout surface has a thickness of only 5 mm, while the PMTs have a photocathode diameter of 15 mm. To avoid direct excitation of the photocathode by Cherenkov light, the free photocathode surfaces can be shielded from the water. This is depicted in Figure 3.9.

The WLS can be rotated over 360° around the symmetry axis parallel to its length.

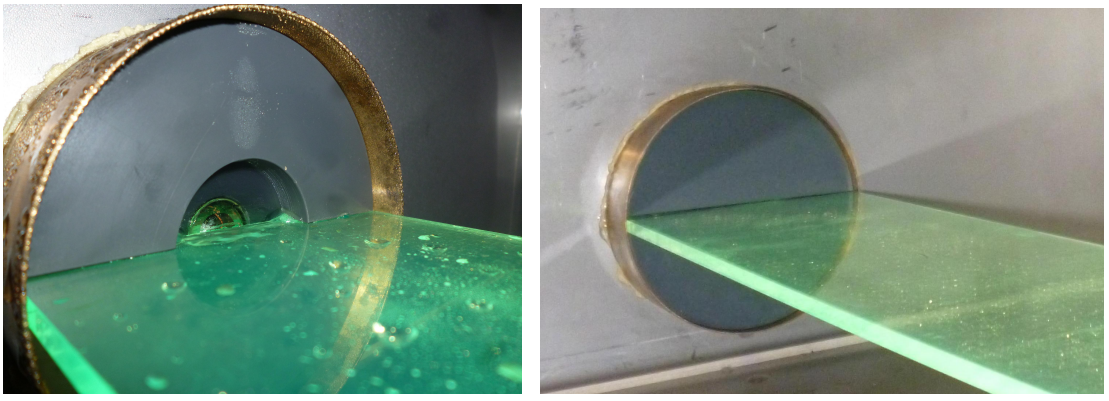

(a) (b)

FIGURE 3.9: (a) PMT window at one of the WLS readout surfaces just after the tank was emptied. (b) Same PMT window, but with added photocathode shielding to exclude direct detection of Cherenkov light.

3.1.4 Choice of detector parts and materials

The goal for this thesis is to detect Cherenkov light using a WLS. A careful choice of the WLS material and the PMTs should allow a maximal signal detection efficiency.

The WLS should be chosen such that its absorption spectrum lies in the middle UV-part[5]/blue part of the electromagnetic spectrum[6]. The *QE* of the PMT should overlap as much as possible with the WLS emission spectrum. Evidently, the WLS must show little self-absorption.

Being the very first stage of the detector development, it was decided to borrow a WLS from Universität Bonn, and use PMTs that were already available in Ghent. Figure 3.10 shows the Cherenkov-light distribution (Equation 1.33), together with the XP1911/UV *QE* curve, and the capture efficiency and emission spectrum of the WLS BC-482A. In absolute numbers, the capture efficiency reaches a maximal value of approximately 17% at 425 nm, if the WLS is read out along the full area on both ends [123]. As mentioned in the previous section, only 1/10th of these readout surfaces is coupled to a PMT. As a conservative assumption, the capture efficiency therefore decreases by a factor of 10.

It is clear from this figure that the PMT XP1911/UV is not perfectly suited to use together with the BC-428A WLS. The WLS shifts the absorbed Cherenkov photons away from the *QE* peak. Nevertheless, we opted to work with the materials at hand[7].

3.2 Readout electronics

Figure 3.11 shows a schematic representation of the electronic readout system used for this experiment. The CAEN SY527 [131] module provides the high voltage supply for all the PMTs. The type of signals (PMT signal, positive block pulse (TTL) or negative block pulse (NIM) are shown in red at each stage of the readout. The green lines represent a connection with the computer through the controller [132]. The dashed line represents a veto signal, provided by the computer to prevent date storage in the QDC (charge-to-digital-converter [133]) buffer when the detector is on[8] but no measurement has started yet.

[5] 200-300 nm.

[6] See Section 1.3.2.

[7] The WLS BC-480, with minimal detectable wavelength at 260 nm and an emission peak at 425 nm was also present at Bonn and could have been a better option. However its dimensions did not agree with the dimensions of the water tank. To speed up things, the water tank was constructed using an already existing tank, hence limiting the dimensional options for the WLS.

[8] Which means that all the PMTs are at high voltage.

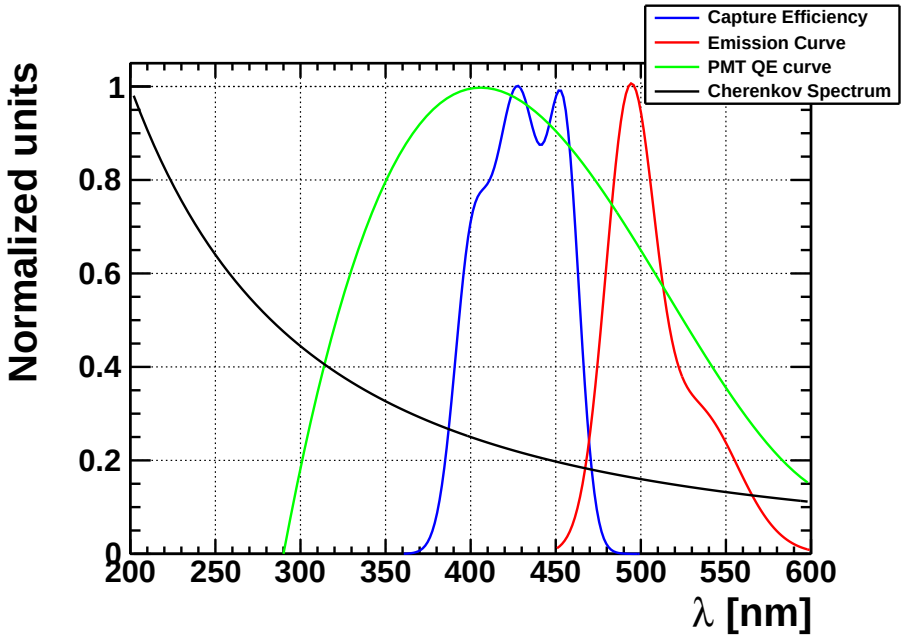

FIGURE 3.10: Comparison of the wavelength windows of the capture efficiency curve and emission curve of the WLS BC-482A, the *QE* curve of the PMT XP1911 (which agrees with the *QE* curve of the XP1911/UV for λ >300 nm; see Figure 3.6(a)), and the $1/\lambda^2$ Cherenkov spectrum. The vertical axis is in normalized units.

Both trigger planes are treated separately before they are tested for coincidence. For each trigger the 8 PMT outputs are fed to a constant fraction discriminator (CFD 1 and CFD 2 of the type CAEN V812 [134]) which converts the PMT pulses in block pulses if they pass a certain voltage threshold. CFD 1, CFD 2, and coincidence unit COINC 1 [135] together act like an exclusive OR gate: a COINC 1 output signal is only produced if there is a coincidence between trigger 1 and trigger 2, where the signal of each trigger is a consequence of one PMT only. This eliminates a lot of possible background trigger signals. The OR output provides a NIM pulse when at least one of the input signals passed the threshold, while the MAJ output also provides a NIM pulse if more than one input signal passed the discriminator threshold. The OR and MAJ outputs of CFD 1 and CFD 2 are fed to COINC 1. An output signal is provided (a TTL pulse for the trigger counter and a NIM pulse for the next coincidence unit COINC 2 [135]) if the two OR outputs overlap in time[9] and simultaneously no MAJ outputs are seen[10]. This output signal represents a muon which passed through the setup and was seen by the trigger.

The outputs of both WLS PMTs are added together using the linear fan LIN FAN. This signal is then converted to a block pulse if it satisfies the threshold condition of

[9]The coincidence window is thus determined by the sum of the output widths of CFD 1 and CFD 2.
[10]Meaning that the OR signals are tested for coincidence with each other and for anticoincidence with the MAJ signals.

the constant fraction discriminator CFD ORTEC 935 [136][11]. One output of the CFD is used to count the WLS signals, while the other output is tested for coincidence with the trigger signal (after an appropriate delay Δt_{D1} was installed, see also Section 5.2). If both signals overlap in time, a block pulse is sent by COINC 2 to both a counter and the gate of the QDC.

The QDC integrates the delayed output signal of LIN FAN during the time span of the gate signal. An appropriate delay Δt_{D2} between the linear fan output and the QDC input is needed to make sure that the WLS pulse is integrated completely. The QDC converts the charge of the WLS pulse into a digital number, channel number n_{CH}, which is then stored in a ROOT tree on the computer.

CFD 1, CFD 2, QDC, and the controller are programmed in C++. Two types of measurements can be done: one with a prefixed amount of signal events and one with a prefixed measuring time. The time stamp (resolution of 1 s) and QDC value n_{CH} of each event are stored. The trigger rate and WLS rate[12] are not stored on the computer and need to be read off the counters.

3.3 Measurements

Due to a problems with the absolute calibration and because of the limited available time, only two types of measurements were done: a measurement in air and a measurement in water. These can then be compared to check the significance of Cherenkov light detection in water with a WLS.

3.3.1 Calibration

First attempt: absolute calibration

An attempt was made to do an absolute calibration of a reference PMT using a 405 nm, 5 mW violet laser diode module of the type STAR405F, fabricated by Roithner LaserTechnik [137]. The laser was placed in one of the holders for the WLS PMTs (see Figure 3.2), facing the reference PMT placed in the opposite holder. 4 optical density filters[13], two with a transmission factor $T = 10^{-2}$ and two with $T = 10^{-4}$ at 405 nm, were available to decrease the intensity of the laser output, such that the SPE spectrum of

[11] This constant fraction discriminator is not steered by the computer.

[12] Or more precisely the number of trigger and WLS events seen during the duration of the measurement.

[13] Produced by Präzisions Glas & Optik [138].

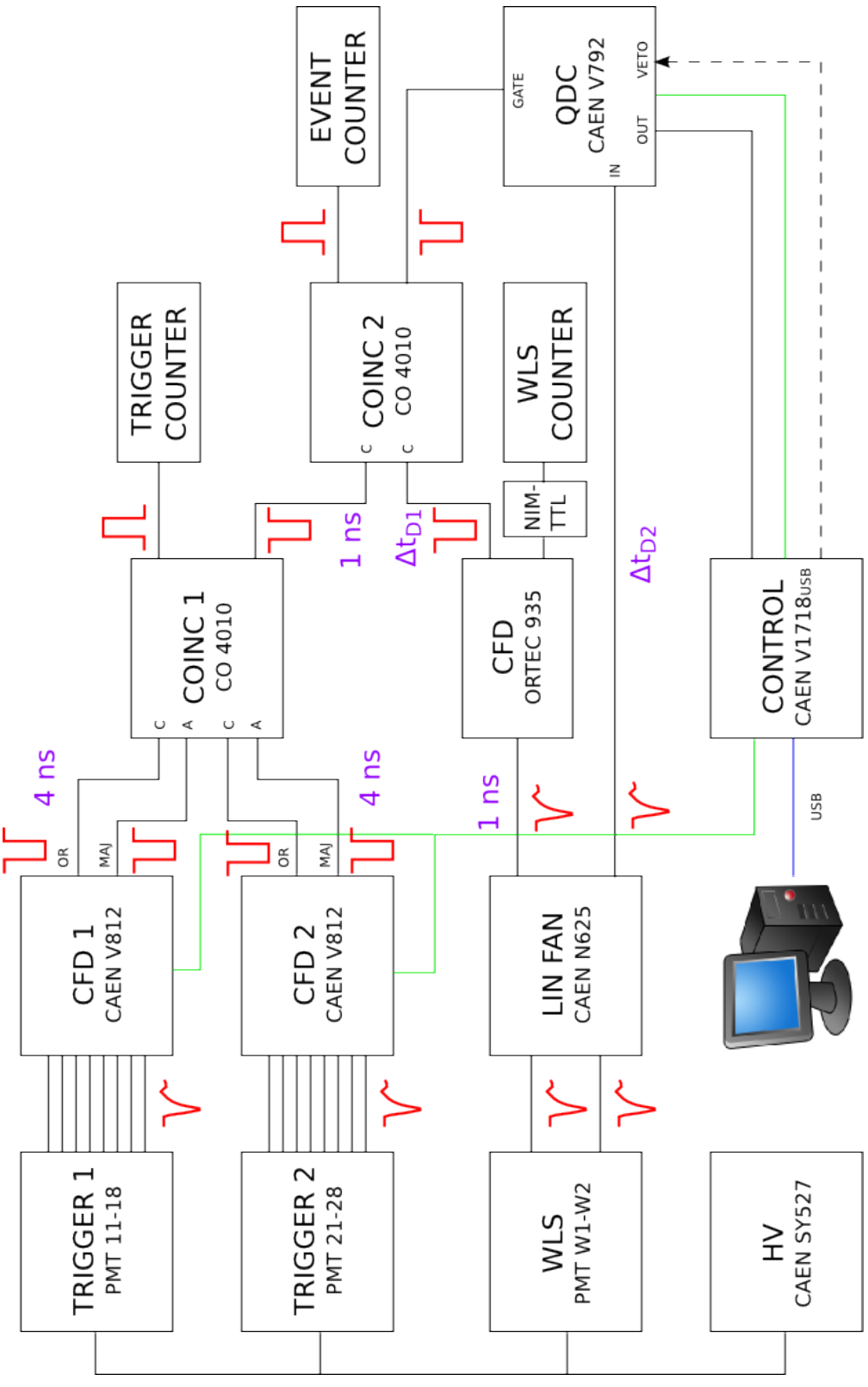

FIGURE 3.11: Schematic representation of the electronic readout for the setup. Where it was relevant, the delays due to cables are given. Δt_{D1} and Δt_{D1} are determined using a persistence check (see Section 5.2). They depend on the delays induced by the cabling and the modules, and on the delays induced by the physics of the whole detection process (decay times of the scintillator and WLS, and the travel times of the photons).

the laser could be measured. The QDC value of the SPE peak, together with the gain of the PMT, and a pedestal measurement[14] allow a conversion from QDC channel numbers to electric charge. Once the SPE peak position and width is known, it is possible to estimate the position and width of the 2PE, 3PE, ... peaks using Equation (2.5). After calibrating the reference PMT, the voltages of the other PMTs can be adjusted such that they show the desired behavior.

The measurements were done in an empty tank, without wavelength shifter. Unexpected results (see Chapter 5) and a limited available time, forced us to do a relative calibration.

Second attempt: relative calibration

Without the identification of the SPE peak it is still possible to do a relative calibration. This is achieved by demanding that all the PMTs respond similarly to a certain input signal. The scintillation counting rate and QDC spectrum was measured for a reference PMT coupled to one of the trigger scintillators. The high voltage and CFD threshold settings are chosen such that the PMT operates in its linear zone (linear relation between input and output of the PMT) and that little or no noise passes the threshold of the CFD. Once this behavior is established for the reference PMT, the high voltages of the other PMTs are tweaked such that these PMTs have similar counting rates and QDC spectra for scintillation measurements[15]. Note that this relative calibration is more than sufficient for the trigger PMTs, because the combination of a high threshold value together with the trigger coincidence check gives a very good muon identifier. However, the threshold for the WLS signals used in the actual Cherenkov measurement should be as low as possible, because these signals are expected to be small. An absolute calibration allows to verify whether this threshold gives a cut-off before or after the SPE peak. A relative calibration does not allow this.

3.3.2 Looking for the Cherenkov effect

To test whether the WLS can be used to detect Cherenkov light, both a measurement with a full water tank (distilled water) and with an empty water tank were done. If carried out under the exact same circumstances and provided that the muon input flux

[14] A zero-signal or pedestal measurement is needed to determine the full relation between QDC channel number n_{CH} and the electric charge Q: $Q_{\langle SPE\rangle} = n_{CH}^{ped} + S * n_{CH}^{\langle SPE\rangle}$, where S is the unknown slope of the linear relation. The pedestal value corresponds to the charge required to operate the QDC during the gate interval. The PMT is calibrated if the slope value S is determined.

[15] Assuming that the atmospheric muon flux does not vary considerably between the different measurements.

is similar, both measurements should give the same background contribution[16], as well as a similar contribution from Cherenkov light created in the WLS itself. Hence, if subtracting both results from each other gives a rate significantly different from zero, this must be attributed to the presence/absence of the water. This provides a quick and easy way to check the feasibility of Cherenkov light detection with a WLS.

[16] Assuming that the Cherenkov effect in air is negligible (see Chapter 4)

Chapter 4

Monte Carlo Simulation

A Monte Carlo (MC) simulation of the experiment was carried out in C++ to get a rough idea of the efficiency of the detector. The results are discussed in this chapter. Some results suggest that there is still a bug present in the code. They are presented nevertheless, because the code or parts of it can be used for the continuation of this project.

4.1 MC program

4.1.1 General structure

The MC main program uses four classes to simulate the physics processes in the detector:

- The trigger, water tank, and WLS are all represented by objects of the class *BOX*. Such an object is defined by its geometrical properties (dimensions and positioning in space) and its physical properties (refractive index n). Figure 4.1 shows the geometrical properties of a box. Table 4.1 lists all the box properties of the trigger, water tank, and WLS for the actual setup. The two different positions of the WLS used in the simulations are displayed in Figure 4.2. Note that the trigger box has refractive index 0, because it is not used[1].

  The difference in physical properties between the media in the water tank (water or air) and the WLS box (i.e. the WLS material itself) is only expressed by the refractive index. The media are assumed to be non-dispersive. This is a

[1]The watertank is made light tight during the measurements (with a dark cover), such that we can assume that no external light (Cherenkov, daylight, ...) enters the water tank.

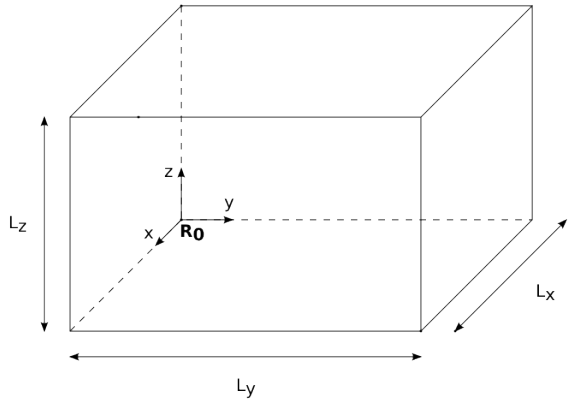

FIGURE 4.1: Geometrical properties of a box.

TABLE 4.1: Geometrical and physical properties of the trigger, water tank, and WLS used in the simulations. The geometry values correspond to the real values for the setup. The refraction index of water (air) is 1.34 (1.000277) [139].

Geometry	Box	Geometrical properties						Medium
		L_x $[m]$	L_y $[m]$	L_z $[m]$	X_0 $[m]$	Y_0 $[m]$	Z_0 $[m]$	n
Horizontal	Trigger	0.57	0.81	0.80	0	0	0	0
	Tank	0.575	0.817	0.345	-0.0025	-0.0035	0.18	1.34 (1.000277)
	WLS	0.10	0.797	0.005	0.235	0.0065	0.25	1.59
Vertical	Trigger	0.57	0.81	0.80	0	0	0	0
	Tank	0.575	0.817	0.345	-0.0025	-0.0035	0.18	1.34 (1.000277)
	WLS	0.005	0.797	0.10	0.285	0.0065	0.20	1.59

valid assumption in the relevant wavelength windows (the visible part of the electromagnetic spectrum). For the tank medium, other characteristics, such as the absorption length and scatter length, are ignored (see Section 4.1.2). Absorption and re-emission by the WLS is specified by a capture efficiency and an emission curve (see next section).

– A muon is simulated as an object of the class *MUON*, which is a subclass of the class *PARTICLE*. The *PARTICLE* class keeps track of the position and direction vector of its objects, throughout the whole setup. A *MUON* object is specified by its mass and initial energy. The Cherenkov threshold energies in the different media, the distances travelled in the detector, together with the number of Cherenkov photons initially created, and the numbers of photons that survive each different stage (hitting the WLS, WLS capture, PMT capture,...) of the detector are also stored.

– A photon is simulated as an object of the class *PHOTON*, which is a subclass of the class *PARTICLE*. Apart from the *PARTICLE* properties, a *PHOTON* object also stores the Cherenkov angle for the water tank medium, and the absorption,

emission, and transmission properties for the different media encountered by the photon in the setup.

The input parameters of the main program are given in Table 4.2.

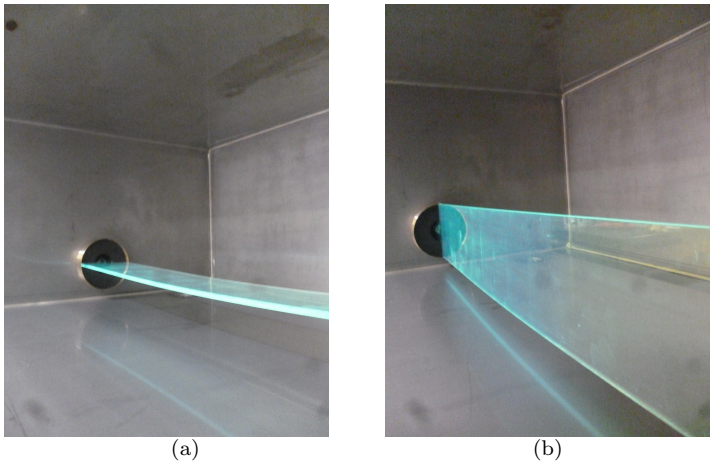

(a) (b)

FIGURE 4.2: (a) Horizontal WLS position. (b) Vertical WLS position.

TABLE 4.2: The MC main program input parameters.

Input parameter	Description
N_{MC}	Number of MC simulations carried out
$N_{trigger}$	Number of trigger muons simulated in a MC simulation
waterLevel	Water level in the tank
$[E_1, E_2]$	Energy range for the muon flux
D_{step}	Distance between consecutive Cherenkov emission points along the muon track in the tank medium

4.1.2 A closer look at the main program

Let us follow a muon through the setup to explain the main program. We look at the special case where the muon passes through the WLS, and thus also generates Cherenkov light in the WLS medium. The origin of the reference system is defined as the zero point of the trigger box, with the z-axis pointing upwards.

1. Muon impact position and direction

   The muon impact position is uniformly generated in the top trigger plane. The zenith angle θ, where $\theta = 0$ corresponds to the positive z-axis, is generated between $\pi/2$ and π according to a $\cos^2\theta$ distribution (Equation (1.20)). The azimuthal angle ϕ is drawn from a uniform distribution between 0 and 2π. If the generated muon does not cross the second trigger surface, a new zenith and azimuthal angle are generated. The impact position distribution on the top plane of the water tank for a MC simulation with $N_{trigger} = 10000$ is shown in Figure 4.3(a). The non-uniformity is a consequence of the angular distribution, depicted in Figure 4.3(b) and the geometry of the trigger (which also alters the ϕ distribution).

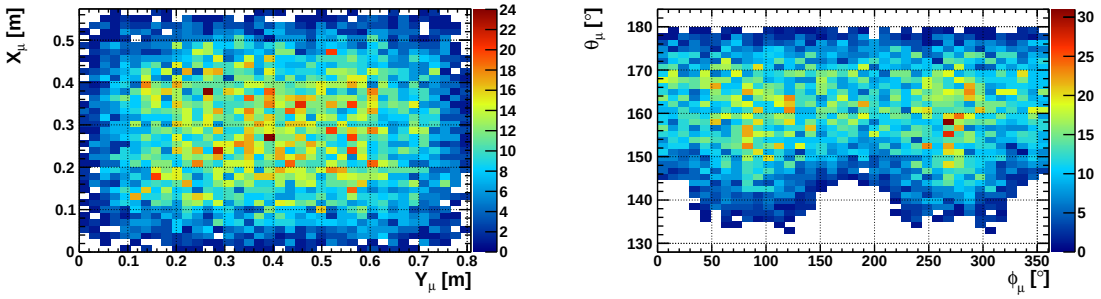

(a) (b)

FIGURE 4.3: (a) Muon impact position distribution on the top plane of the water tank for 10000 trigger muons. (b) Zenith versus azimuthal angle for the same trigger muons as in (a) (see Table 4.1).

2. Muon energy

   The energy of the muon is generated between $E_1 = 0.5$ GeV and $E_2 = 15$ GeV using a $1/E$ distribution (see Figure 1.7(a)). Conveniently, this energy window allows to safely ignore muon energy losses during the passage through the setup (see Figure 1.8(a)). Using Equation (1.30), an expression for the Cherenkov energy threshold can be derived

$$E_{th} = \frac{m_\mu}{\sqrt{1 - \frac{1}{n^2}}}. \tag{4.1}$$

E_{th} is equal to 0.136 GeV, 0.159 GeV, and 4.49 GeV for WLS, water, and air respectively.

3. Muon propagation

   The different intersections of the forward muon track with the setup are calculated using the impact position and direction of the muon, and the coordinates of the planes of the different boxes. In this specific case, the muon track has two intersections with the water tank and two intersections with the WLS. Using the coordinates of these intersection points, the different muon distances within the setup, listed in Table 4.3, are calculated.

   TABLE 4.3: The different distances traversed by the muon in the setup.

Distance	Description
D_{tr}	Distance between the trigger planes
D_{ta}	Distance in the tank
D_{w1}	Distance between water level and first intersection with the WLS
D_{wls}	Distance in the WLS
D_{w2}	Distance between second intersection with the WLS and second intersection with the tank
D_{w}	Distance in water ($D_w = D_{w1} + D_{w2}$ if the muon passes through the WLS)

4. Photon emission position and direction

   The expected number of Cherenkov photons is calculated in each part of the setup using Equation (1.33). Note that we assumed a constant refractive index and that β is constant because energy loss is ignored. The wavelength window is determined by the capture efficiency $\epsilon_{WLS}(\lambda)$ of the WLS (Figure 3.10). $\epsilon_{WLS}(\lambda)$ gives the efficiency for a photon entering the WLS, to be absorbed by the WLS, then shifted to a larger wavelength, and finally propagate to either end of the WLS bar where

it is available for PMT readout. It was calculated by Lukas Schulte[2], based on measurements with this specific BC-428A WLS bar, assuming that the WLS is read out over the full front area on both ends [123]. In the current setup, only 1/10th of each readout side is covered by a PMT photocathode. As a conservative assumption, the capture efficiency curve was rescaled by a factor of 10 for usage in the MC simulations.

In each part within the tank, the Cherenkov photons are emitted at equidistant emission vertices along the muon track. As we will see in Section 4.2, the contribution of Cherenkov photons created in air to the detector efficiency (see *Detector efficiency*) is very small compared to the contribution of Cherenkov photons created in water. Hence, above the water level the Cherenkov effect is ignored in the simulations. The distance D_{step} between two consecutive emission vertices should be chosen as small as possible such that typically only one photon is emitted at each vertex. The number of photons at each vertex within a certain part in the tank is drawn from a Poisson distribution with expectation value $\langle N \rangle = N_{Cher}/N_{vert}$, where $N_{vert} = D_{part}/D_{step}$ is the number of vertices in that specific part of the tank. Within the WLS, photon propagation is not simulated (see *Photon propagation*) and thus the total number of Cherenkov photons is directly drawn from a Poisson distribution with $\langle N \rangle$ equal to the expected number of photons provided by Equation (1.33)[3].

For the emission direction of a photon at an emission vertex, a uniform azimuthal angle ϕ is generated and a zenith angle $\theta = \pi - \theta_C$ is calculated using Equation (1.32). Note that these angles are defined in the muon reference frame, which is displayed in Figure 4.9. The z_μ axis points along the positive direction of the muon track. The y_μ axis is perpendicular to the plane defined by the z_{tr} axis and muon track, in which also the x_μ axis . The muon reference frame is related to the trigger box reference frame through two consecutive rotations: a rotation around the y_μ axis over an angle θ_μ, followed by a rotation around the $z'_\mu = z_\mu$ axis over an angle $\pi - \phi_\mu$[4].

Figure 4.5(a) shows the Cherenkov cone projection on the horizontally positioned WLS for a 1 GeV muon crossing the setup perpendicularly through its center. The ring structure is obtained by only reading out the hit positions on the WLS for those photons that are emitted in a small layer of water 5 cm above the WLS. Using Equation (1.32), one can calculate the expected diameter of the Cherenkov ring to be 8.9 cm. Figure 4.5(b) shows the same situation but for readout along the complete muon track in the 5 cm water layer.

[2] Physikalisches Institut, Universität Bonn.
[3] For $\langle N \rangle > 20$, a Gaussian distribution with mean value $\langle N \rangle$ and standard deviation $\sqrt{\langle N \rangle}$ is used.
[4] Remember that a (counter)clockwise rotation corresponds to a negative (positive) rotation angle.

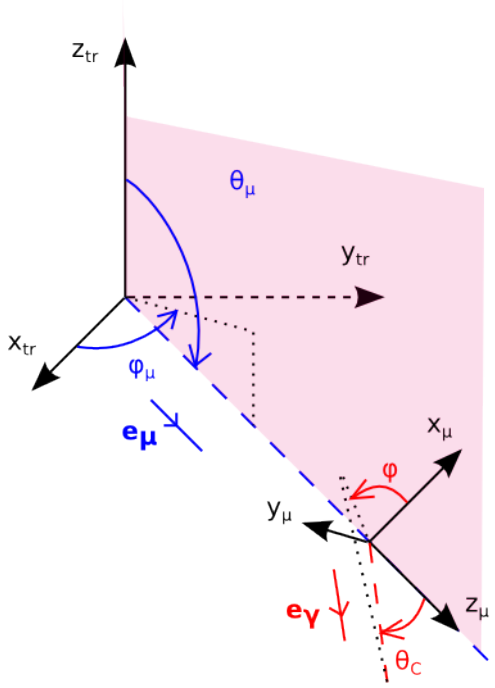

FIGURE 4.4: Definition of the muon frame and the angles of the Cherenkov photon in this frame. The muon track and muon coordinates (θ_μ, ϕ_μ) are indicated in blue, while the photon track and photon coordinates $(\theta_\gamma, \phi_\gamma)$ are indicated in red.

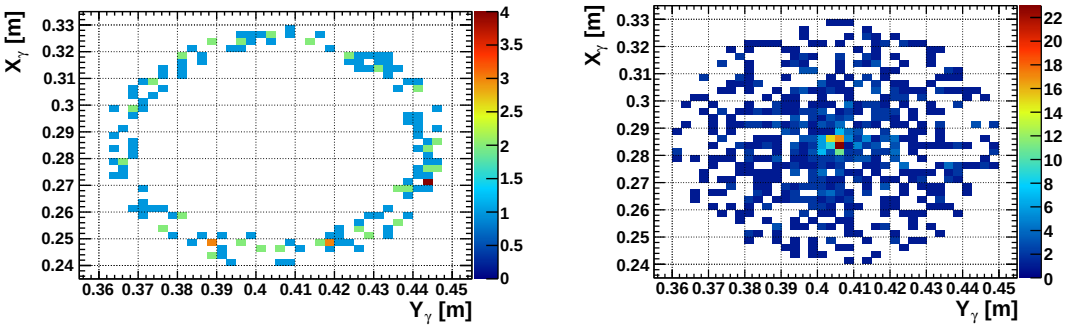

(a) (b)

FIGURE 4.5: (a) Cherenkov cone projection on the horizontally positioned WLS for a 1 GeV, $\theta = \pi$ muon crossing a small layer of water at 5 cm above the WLS. (b) Identical situation as in (a), but for a water layer of 5 cm above the WLS (see Table 4.1).

5. Photon propagation

   The photon propagation is identical to the muon propagation. For photons we only look for direct crossings of the forward photon track with any of the WLS surfaces. If a photon hits the WLS, the probability for transmission from the tank medium to the WLS is calculated. Note that this probability is wavelength-independent (as the media are assumed to be non-dispersive) and close to 1.

   Reflections at the walls of the tank, as well as photon scattering and absorption in the tank medium are ignored for simplicity reasons. The latter two could be incorporated by using an effective attenuation factor (which is wavelength dependent in the worst case scenario), based on absorption measurements for the water in the water tank. Depending on the value of this experimental attenuation length one can decide whether reflections at the walls should be incorporated or not.

6. Photon absorption and re-emission in the WLS

   If a photon enters the WLS, a Cherenkov wavelength is generated according to a $1/\lambda^2$ distribution (see Equation (1.33)). Note again that the assumption of constant refractive indices allows to generate a Cherenkov photon wavelength at this stage of the simulation and not earlier. The wavelengths are only generated between 360 nm and 500 nm, where the capture efficiency of BC-482A is non-negligible[5]. As mentioned earlier, the capture efficiency curve is an effective parameter also containing the photon propagation process inside the WLS towards the PMT cathode surfaces. It is thus not necessary to explicitly follow the photon movement inside the WLS.

   Because the photon capture both incorporates photon absorption and propagation to the readout PMTs, only for those photons that are captured an emission wavelength needs to be generated. This is done between 460 nm and 600 nm, where the WLS emission spectrum is non-negligible (see Figure 3.10). Note that the absorption and emission wavelength are assumed to be uncorrelated and that possible self-absorption in the overlap-window [460 nm, 500 nm] is ignored.

7. Photon capture by the PMT photocathode

   Before the photon enters the photocathode, transmission from WLS to a perspex window through an intermediate optical gel layer, followed by transmission from the perspex window to the PMT through another intermediate optical gel

[5]Photons with wavelengths outside this window, could still directly reach the photocathode of the WLS PMTs, as for those photons the WLS just acts as a transparent medium with a different refraction index. This effect is ignored in the simulations.

layer needs to be checked[6]. The *QE* efficiency curve of the PMT then determines whether the photon creates a photoelectron in the photocathode or not[7].

8. Detector efficiency

   The absolute detector efficiency ϵ_{abs} is defined as

$$\epsilon_{abs} \pm \sigma_{\epsilon_{abs}} = \frac{N_{\mu}^{det}}{N_{trigger}} \pm \sqrt{\frac{(1-\epsilon_{abs})\epsilon_{abs}}{N_{trigger}}}, \tag{4.2}$$

   where N_{μ}^{det} is the number of muons detected through the Cherenkov effect and the error is a binomial error. In the simulations, a muon is considered as detected if at least one photon created a PMT photoelectron. Note that this quantity can be compared directly with the corresponding measured quantity.

   Dividing ϵ_{abs} by the active surface of the WLS gives the efficiency per unit WLS surface. Both geometries listed in Table 4.1 have the same active WLS surface $S = 2 \times (L_{WLS}^{x} L_{WLS}^{y} + L_{WLS}^{y} L_{WLS}^{z}) = 0.167$ m^2.

   This efficiency still depends on the geometry of the water volume relative to the geometry of the WLS. An easy way to check this dependence is to lower the water level in the tank step by step. Note that this is also a nice experimental check.

4.2 Results

Determining the WLS positioning for the experimental setup

The MC simulations were used to determine the best WLS position of the two listed in Table 4.1 in the case of a full water tank.

A MC simulation with 10000 muons was carried out for both the horizontal and vertical WLS geometry. Figure 4.6 shows the number of Cherenkov photons that reached the final stage of the simulation, i.e. those which create a photoelectron escaping the photocathode . For the horizontal WLS geometry an absolute detection efficiency $\epsilon_{abs} = (59.30 \pm 0.49)$ % is found, while this is (43.20 ± 0.50) % for the vertical WLS geometry. Note that this is as expected: from the trigger and water tank geometry relative to the WLS geometry, and from the muon angular distribution, it is clear that for the vertical WLS geometry less Cherenkov cones overlap partially or completely with the side planes of the WLS compared to the case for the top plane of the horizontal WLS geometry.

[6]Since the photon propagation inside the WLS is not explicitly calculated, a simple estimate for the two transmission factors is made. They are both assumed to by 0.95.

[7]The transmission probability through the PMT glass is assumed to be 1.

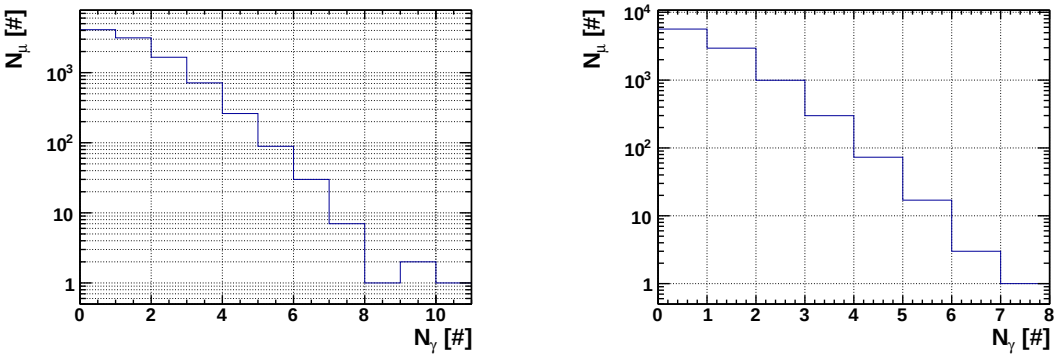

(a) (b)

FIGURE 4.6: Number of muons as a function of the number of photons per muon reaching the final stage of the MC simulation. MC simulation with 10000 $E_\mu \in [0.5, 15]$ GeV muons for (a) the horizontal WLS geometry and for (b) the vertical WLS geometry (see Table 4.1).

Looking at the photon position distribution on the planes of the WLS presented in Figure 4.7, it is expected that there is still a bug present in the code. In Figure 4.7(a) a symmetry is observed as expected, with most photons hitting the center of the top plane of the WLS. An asymmetry is observed in Figure 4.7(b), which is unexpected from geometrical arguments. A closer look at the z-coordinate of the photon position on the WLS in Figure 4.8 suggests that a bug is present in the code which only manifests itself significantly for the vertical WLS geometry. The two peaks at $Z_\gamma = 0.250$ m and $Z_\gamma = 0.255$ m in Figure 4.8(a) are due to hits on the top and bottom plane. In Figure 4.8(b) the peak at $Z_\gamma = 0.3$ has a similar origin. Just below this peak an unexpected decrease in hits is observed which seems to agree with the increase in hits just above $Z_\gamma = 0.2$.

The generation of the Cherenkov photon directions is assumed to be correct after several successful tests. Hence, the bug is assumed to be present in the calculation of the intersection with the side planes of the WLS for those photons which are created in the water region next to the WLS. Since this region is very small in the case of the horizontal WLS geometry, this might be the reason why we do not see an unexpected result there. The bug has not been found yet, but is assumed to be irrelevant for the case of the horizontal WLS geometry. A good next step would be to assume an infinitely thin WLS, such that only one plane needs to be checked for crossings, rather than six.

Dependence of the setup on the water volume

For the horizontal geometry, the dependency on the water volume was checked by running MC simulations for different water levels. As expected, the absolute efficiency

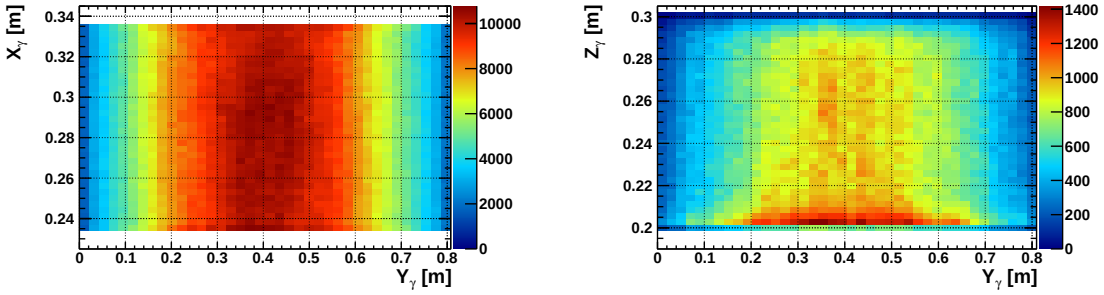

(a) (b)

FIGURE 4.7: Photon position distribution on the WLS for a MC simulation with 10000 $E_\mu \in [0.5, 15]$ GeV muons. (a) Top plane in the case of the horizontal WLS geometry (b) Side planes in the case of the vertical WLS geometry (see Table 4.1).

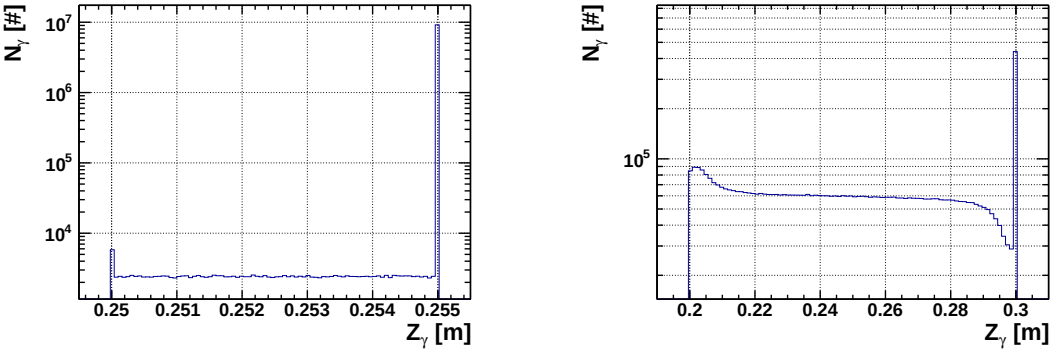

(a) (b)

FIGURE 4.8: Photon z-coordinate distribution on the WLS for a MC simulation with 10000 $E_\mu \in [0.5, 15]$ GeV muons. (a) Horizontal WLS geometry (b) Vertical WLS geometry (see Table 4.1).

decreases with the water level and goes to zero when the water level is at the same height as the top plane of the WLS. A second order polynomial $\epsilon_{abs} = p_0 + p_1 z + p_2 z^2$ is fitted to the MC data points, where $z = Z_{water} - Z_{WLS,top}$ is the level of the water above the top plane of the WLS.

A MC simulation with 10000 muons in air for the horizontal WLS geometry showed that the Cherenkov detection in air can be safely neglected for this setup ($\epsilon_{abs} \approx 0.01\%$).

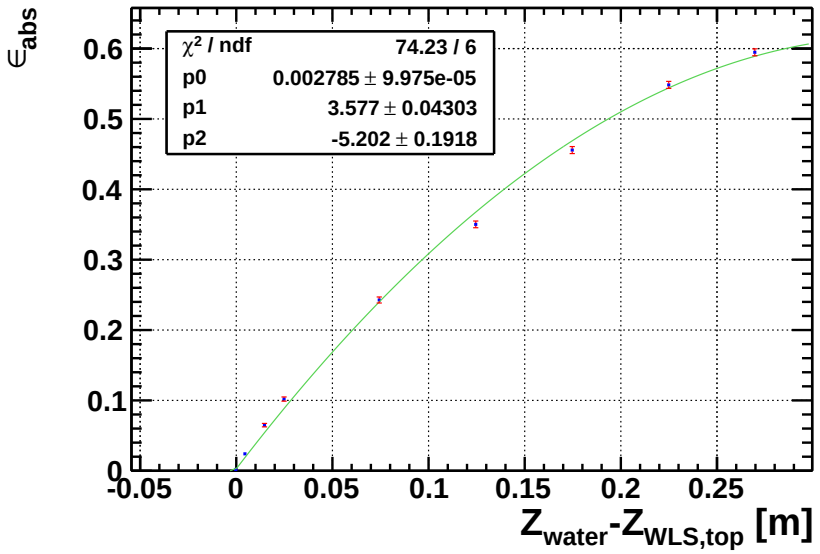

FIGURE 4.9: Absolute efficiency ϵ_{abs} as a function of the water level above the top WLS plane for the horizontal WLS geometry (see Table 4.1). The simulations were carried out with 10000 $E_\mu \in [0.5, 15]$ GeV muons.

Chapter 5

Measurements and results

Four measurements were done to test the feasibility of using a WLS coupled to a PMT as a Cherenkov light detector. The results are presented in Section 5.2. An outlook on these experiments is given in Chapter 6. First, we start with a discussion on the calibration of the detector.

5.1 Detector calibration

The setup is designed such that a Cherenkov counting measurement can be done. The counting experiment is based on temporal coincidence between trigger signals and signals from the PMTs mounted to the WLS readout planes (see Section 3.2). The light signals in the trigger (scintillation pulses, see Section 3.1.2.1) and in the WLS (luminescence pulses, see Section 3.1.3) are transformed to electrical signals by PMTs before they are tested for coincidence. For a given light signal, this transformation should always be the same in order to obtain a uniform behavior of the detector. The transformation behavior of a PMT, i.e. the gain and linearity of the multiplication process, depends on the high voltage of the PMT (Section 2.3.2). Setting the high voltages of the PMTs such that they all respond similarly to a given input is called a relative calibration.

The setup also allows to integrate over the charge signals from the WLS PMTs which satisfied the temporal coincidence condition. An interpretation of the thus obtained pulse-height or QDC spectrum requires an absolute calibration. For a PMT at a certain voltage, the relation between the QDC output of a signal and the number of photoelectrons of that same signal can be determined by measuring the QDC spectrum of a well-known source, for which the SPE peak can be identified. Typically, lasers are used to do such an absolute calibration.

5.1.1 Absolute calibration

Laser output

The STAR40F5 violet laser diode module was modulated using TTL pulses with a minimal width of 20 ns. The average number of photons N_γ emitted by the laser in a pulse of Δt_{pulse}, is given by the relation

$$N_\gamma = \frac{P_{laser}[J] \times \Delta t_{pulse}[s]}{E_\gamma[J]} \approx 10^7 \times \Delta t_{pulse}[ns], \tag{5.1}$$

where $P_{laser} = 5$ mW is the power of the laser and $E_\gamma[J] = 1.24/\lambda[\mu m] \times 1.6 \times 10^{-19} = 5 \times 10^{-19}$ is the energy of a photon with wavelength $\lambda = 405$ nm. For a minimal obtainable pulse width of 20 ns this requires a filter with transmission factor $T \approx 10^{-8}$ to have approximately one photon per laser pulse on average. Note that the flux received by the PMT placed at the other side of the empty water tank, facing the laser diode module, might be lower due to losses caused by a finite laser beam width. Several filter factors can be obtained with the two $T = 10^{-2}$ filters and the two $T = 10^{-4}$ filters (both at 405 nm).

Calibration with a laser

The goal of the absolute calibration is to find the relation between the QDC channel number N and the actual integrated charge Q. To obtain a SPE spectrum with the laser, we want to have as little as possible higher PE signals. E.g. if we want to limit the probability for a 2PE laser signal to 10%, the average number of photons n per laser pulse is set by the condition $P(2, n) = 0.01$ (see Equation (2.5)). Depending on the strength of the filter placed in front of the laser, this condition allows to determine the duration of the TTL modulation pulse.

Figure 5.1 displays the readout scheme used for the absolute calibration measurement. In the ideal case the QDC gate signal is constructed using the modulation pulse of the laser. However, setting the appropriate delay for the gate signal turned out to be problematic and we opted to construct the gate signal using the PMT output signal. This has the disadvantage that a gate signal is only produced after the CFD, and an unwanted threshold comes into the game. Unexpected results were obtained in this manner. This is believed to be due both to a poor understanding of the QDC pedestal behavior and an unexpected pulse shape of the laser signal. Even for $T = 10^{-12}$ and pulse widths of 20 ns, afterpulses where observed on an oscilloscope. These afterpulses

both influence the coincidence rate and the QDC spectrum, making a clear interpretation of the obtained results difficult.

Because of these unexpected results and because of the limited available time, it was decided to only do a relative calibration of the detector. For these measurements, as well as for the final measurements, the QDC spectrum was still measured, as this happens independently from the counting experiment (see Figure 3.11). A linearity test of the QDC, using block pulses of variable heights as input signals, did show that the QDC responds linearly to its input. In the following, the QDC behavior is considered as trustworthy up to that level.

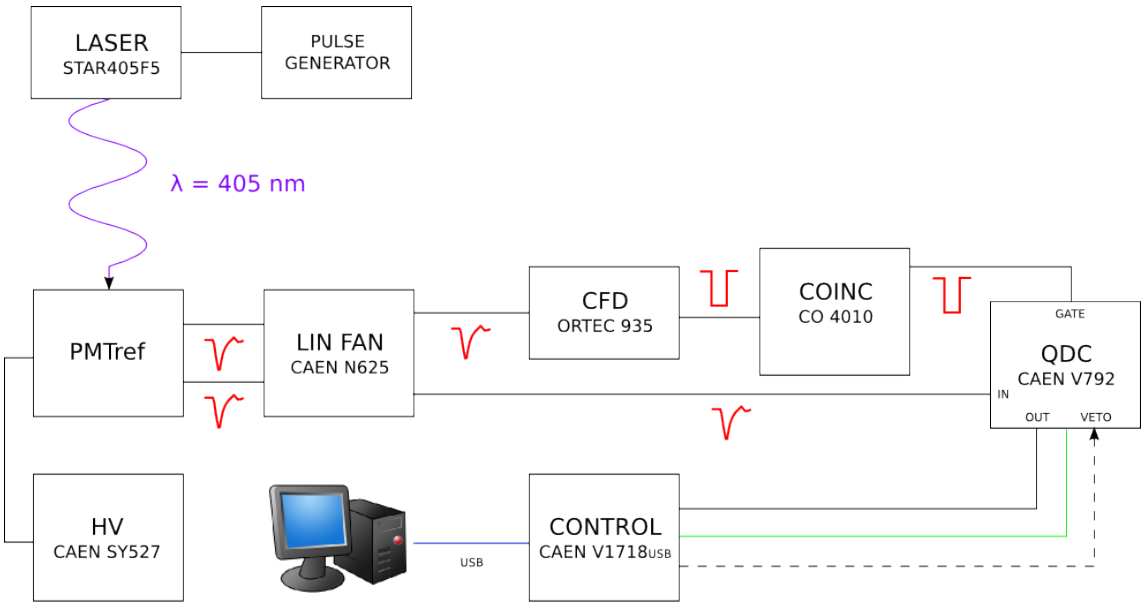

FIGURE 5.1: Schematic representation of the electronic readout for the absolute calibration measurement.

5.1.2 Relative calibration

Scintillation counting measurements (see Section 3.1.2.1) were done for the relative calibration of the PMTs. Each PMT was coupled to its respective scintillation bar in the trigger, as depicted in Figure 3.3(d). The WLS PMTs, PMT W1 and PMT W2, were coupled to scintillator SCINT 11 and SCINT 28 respectively for their calibration measurement.

Figure 5.2 shows the QDC spectrum of the reference PMT (PMT 11) for a scintillation counting measurement of 10 minutes. The PMT voltage was set to 1300 V, in order to operate in the safe zone of the PMT, where a linear relation holds between the input and output signal of the PMT. A peak is observed around channel number $n_{CH} = 400$. The

readout scheme for this measurement is similar to the one displayed in Figure 5.1, but with the PMT coupled to scintillation light rather than laser light. The CFD threshold value was set such that 50 mV is the minimum voltage satisfying the threshold condition for block pulses with a width of 40 ns. This is believed to be the reason for the cut-off in the QDC spectrum at $n_{CH} \approx 250$[1].

Figure 5.2(b) shows that the scintillation rate of PMT 11 is approximately uniform in time. The counting rate is (106.0 ± 3.3) min^{-1}, roughly 6 times less than the typical expected rate corresponding to the cosmic ray muon flux through a horizontal detector of similar dimensions (see Section 1.2.2.1). This serves as a good check to make sure that the CFD threshold is set high enough[2] such that noise pulses are eliminated. The threshold also throws away real muon signals, causing a decrease in the muon trigger rate. This implies that longer measurements will be needed to obtain the same statistics for a certain measurement. However, lowering the scintillation rate also decreases the random coincidence rate (see *Muon flux through the calibrated trigger*).

Each trigger bin has a high voltage divider circuit which allows to install 6 different high voltages for the 8 trigger PMTs and for one WLS PMT. Table 5.1 lists the high voltages applied to the PMTs, together with the threshold values of the corresponding CFD channels, and the measured scintillation rates. Appendix **??** shows the QDC spectra for all the PMTs after the relative calibration. These spectra indicate that the calibrated trigger response is approximately position and time independent.

Muon flux through the calibrated trigger

The muon flux seen by the calibrated trigger is (20.87 ± 0.21) min^{-1} or (347.8 ± 3.5) mHz. This was measured for an empty water tank during 8 hours. No delay was installed between both trigger plane signals, since a persistence test on the oscilloscope[3] showed that this was not necessary[4]. The QDC spectrum of this measurement is shown in Figure 5.3. There was no input for the QDC during this measurement, such that this can serve as the pedestal measurement for QDC channel 0.

[1] Note that an absolute calibration would allow a physical interpretation of this CFD threshold and of the peak value.

[2] For the given PMT high voltage.

[3] Visual check of the temporal overlap between the block pulses of both trigger planes. The widths of these block pulses was set to 70 ns.

[4] This is expected, as on average the time difference between a top and bottom trigger plane signal (being the consequence of the same muon) is given by the average transit-time of the muon between both trigger planes. This of the order of a few nanoseconds, which is negligible compared to the 70 ns width of the block pulses. Since both signals undergo the exact same operations in the readout circuit, no extra delay is necessary.

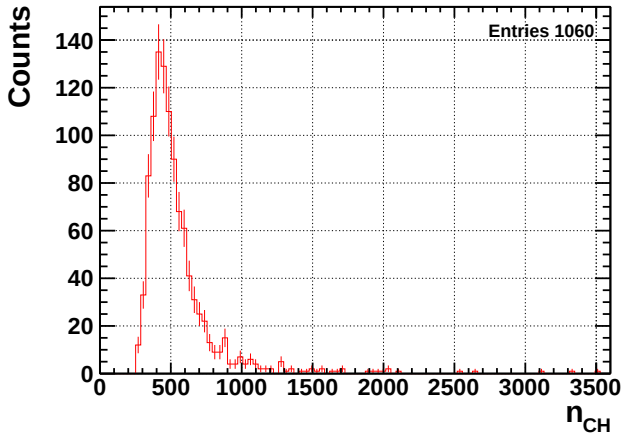

(a)

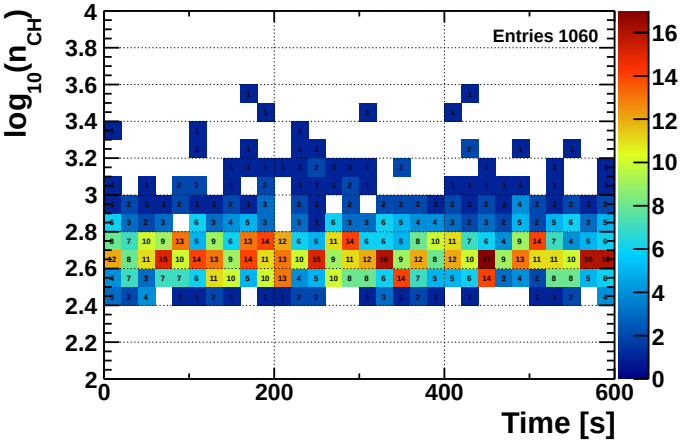

(b)

FIGURE 5.2: (a) QDC spectrum of the reference PMT (PMT 11). (b) Time dependence of the QDC spectrum of the reference PMT.

The random trigger coincidence rate can be estimated using the formula

$$r_{rand} \pm \sigma_{r_{rand}} = r_1 r_2 \Delta t_{res} \pm \sqrt{(r_2 \Delta t_{res} \sigma_{r_1})^2 + (r_1 \Delta t_{res} \sigma_{r_2})^2 + (r_1 r_2 \sigma_{\Delta t_{res}})^2}, \qquad (5.2)$$

where r_1 (r_2) is in this case the rate of trigger 1 (trigger 2) and Δt_{res} is the resolving time of the coincidence. Δt_{res} is approximately given by the sum of the widths of the block pulses used to do the coincidence check and is thus 140 ns for the trigger coincidence. The error on the width of every block pulse is estimated to be 10 ns. The rates of the separate trigger planes were not measured, but can be estimated using the values in Table 5.1. As a conservative assumption, we take 8 times the mean rate of the 8 scintillation counters in each trigger plane as the rate for each trigger plane. This gives $r_1 = 8 \times (116.7 \pm 1.2)$ min^{-1} $= (933.6 \pm 3.4)$ min^{-1} and $r_2 = 8 \times (111.3 \pm 1.2)$ min^{-1} $=$

TABLE 5.1: PMT calibration parameters for each PMT. The high voltage (HV) is expressed in kV. For PMT 11-PMT 28, the CFD modules are of the CAEN V812 type. The threshold value (CFD Thr.) corresponds to a 40 ns, 50 mV negative block pulse (at 100 Hz). The signals of PMT W1 and PMT W2 are converted into block pulses using the ORTEC 935 CFD module. For this CFD, a threshold setting of -192.4 mV on a multimeter corresponds to a 40 ns block pulse of 13 mV.

PMT	HV [kV]	CFD mod.-ch.	CFD Thr.	counts/600 s	rate $[\text{min}^{-1}]$
11	1.300	1-0	41	1060	106.0 ± 3.3
12	1.405	1-1	40	1240	124.0 ± 3.5
13	1.345	1-2	40	1173	117.3 ± 3.4
14	1.470	1-3	42	1085	108.5 ± 3.3
15	1.375	1-4	40	1178	117.8 ± 3.4
16	1.345	1-5	41	1334	133.4 ± 3.7
17	1.365	1-6	40	1027	102.7 ± 3.2
18	1.300	1-7	41	1239	123.9 ± 3.5
21	1.400	2-0	42	1267	126.7 ± 3.6
22	1.340	2-1	41	1123	112.3 ± 3.4
23	1.380	2-2	40	1230	123.0 ± 3.5
24	1.345	2-3	41	1080	108.0 ± 3.3
25	1.330	2-4	39	1083	108.3 ± 3.3
26	1.400	2-5	43	1011	101.1 ± 3.2
27	1.350	2-6	41	1106	110.6 ± 3.3
28	1.380	2-7	41	1006	100.6 ± 3.2
W1	1.400	Ortec	-192.4 mV	1198	119.8 ± 3.5
W2	1.350	Ortec	-192.4 mV	1082	112.3 ± 3.3

(890.4 ± 3.4) min^{-1}, leading to a random coincidence trigger rate $r^{\mu}_{rand} = (32.3 \pm 3.2)$ μHz, which is negligible compared to the total muon trigger rate.

5.2 Results

All the measurements were carried out with the WLS in the horizontal position (see Table 4.1). The readout scheme displayed in Figure 3.11 was used. The threshold for the WLS CFD was set to the lowest possible value in order to avoid throwing away weak WLS signals (see Table 5.1). Note again that the physical meaning of this threshold is not known. The output pulse of the WLS CFD has a width of 100 ns and is tested for temporal coincidence with the 100 ns trigger coincidence block pulse (output pulse of COINC 1 in Figure 3.11). The settings for the trigger are as mentioned in the previous section. The pulse widths were chosen such that the spread in time due to variations in light paths (both in the scintillators and in the WLS) is small compared to the coincidence window. Furthermore, the low trigger and WLS rates ensure that the random coincidence rate between both is very low, despite a 200 ns resolving time. Based on the results of a persistence check, the delay t_{D1} between the WLS block pulse

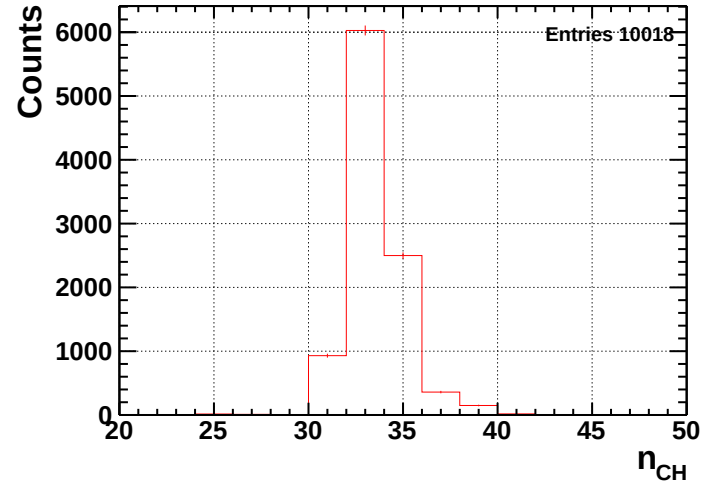

(a)

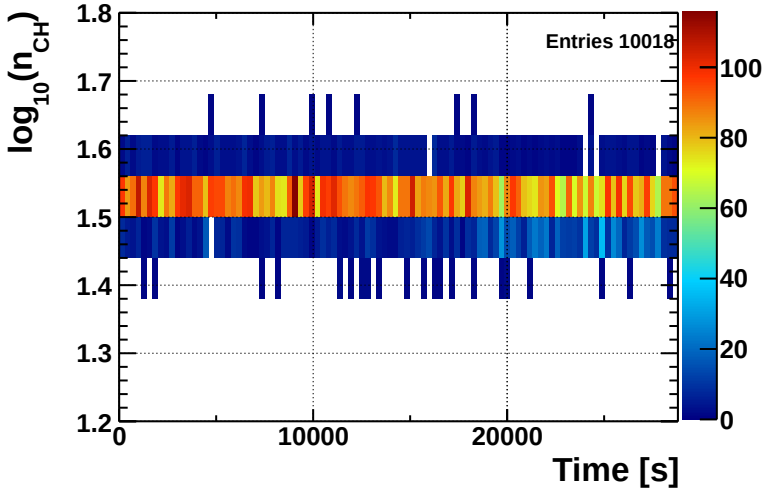

(b)

FIGURE 5.3: (a) QDC spectrum of the trigger measured during 8 hours. The measured values correspond to the pedestal value of QDC input channel 0, as no input was provided for this channel during the gate caused by the trigger signal. (b) Time dependence of the QDC spectrum of the trigger.

and trigger block pulse was set to 37 ns. The width of the coincidence block pulse of the WLS and the trigger (output of COINC 2 in Figure 3.11) determines the width of the QDC gate pulse and was set to 100 ns. A delay t_{D2} of 105 ns was installed between the original WLS signal (which is the sum of PMT W1 and PMT W2 signal) and the QDC input, such that the WLS signal enters QDC channel 0 when the gate is open.

5.2.1 Measurements

Two types of measurements are discussed in this section:

- Light detection via both the WLS and the partially uncovered PMT cathode surfaces (see Figure 3.9(a)). Hence, from the point of view of this thesis, both direct (D) and indirect (I) Cherenkov light detection is possible. A 48 hour measurement was done in air and water. Initially, it was not noticed that parts of the WLS PMT cathodes were directly disposed to the water, thus compromising the measurement. Nevertheless, we included the results of these measurements for the purpose of a consistency check.
- Light detection through the WLS only, i.e. Cherenkov light created in the water can only reach the PMT cathode indirectly. This is established by covering up the free WLS PMT cathode surfaces. A 12 hour measurement was done in air and water.

Table 5.2 lists the counting rates for all these measurements. The random coincidence rate between the trigger signal and the WLS signal, i.e. the random event rate, is also calculated.

Direct and indirect Cherenkov light detection

Figure 5.4 compares the QDC spectra of measurement 1 and 2, while Figure 5.5 shows their time dependence. Both measurements peak at $n_{CH} \approx 90$. Notice that a few events correspond to $n_{CH} \approx 1000$, well above the peak value of the scintillation measurement shown in Figure 5.2(a).In both cases the spectrum shows uniform behavior in time, suggesting that the detector is stable over a long period and that results of the experiment are not heavily influenced by the time of the day. The expected number of observed random coincidence events is smaller than one in both measurements.

Apart from a different medium in the tank, both measurements were carried out under the exact same conditions. This means that background rates from the PMTs

TABLE 5.2: Results for the measurements in water and air, in the case of uncovered (D&I) and covered (I) WLS PMT photocathodes. The number of counts and the rate is given for the trigger, the WLS, and for the signal events. The random coincidence rate is also estimated. If we ignore the low random coincidence rates, the absolute detection efficiency of the detector is given by $\epsilon_\mu = r_{event}/r_\mu$.

	Measurement 1	Measurement 2	Measurement 3	Measurement 4
Type	D&I	D&I	I	I
Medium	water	air	water	air
Δt	48 hr 0 min 16 s	48 hr 16 min 59 s	12 hr 1 min 23 s	12 hr 13 min 15 s
N_μ	48,126 ± 219	60,490 ± 246	11,417 ± 107	14,970 ± 122
r_μ [mHz]	278.5 ± 1.3	348.0 ± 1.4	263.8 ± 2.5	340.3 ± 2.8
N_{WLS}	12,656,652 ± 3,558	11,501,227 ± 3,391	2,410,000 ± 1,552	2,799,458 ± 1,673
r_{WLS} [Hz]	73.238 ± 0.021	66.168 ± 0.020	55.680 ± 0.036	63.631 ± 0.038
N_{event}	2470 ± 50	154 ± 12	289 ± 17	46 ± 7
r_{event} [mHz]	14.29 ± 0.29	0.886 ± 0.071	6.68 ± 0.39	1.05 ± 0.15
N_{event}^{rand}	0.7050 ± 0.0035	0.8004 ± 0.0035	0.1272 ± 0.0013	0.1905 ± 0.0017
r_{event}^{rand} [μHz]	4.08 ± 0.29	4.61 ± 0.32	2.94 ± 0.21	4.33 ± 0.31
ϵ_μ [%]	5.131 ± 0.107	0.2456 ± 0.0204	2.53 ± 0.15	0.309 ± 0.044

(see *Photomultiplier tubes* in Section 3.1.2.1) and any light production inside the WLS are the same in the air and water measurement[5]. Subtraction of the rates gives the signal rate r_{Cher} due to Cherenkov light production in the water

$$r_{Cher} = (r_{water} - r_{water,rand}) - (r_{air} - r_{air,rand})_{rescaled}, \tag{5.3}$$

where the rates in air are rescaled to account for the significantly different muon flux in both cases: $scale\ factor = r_{\mu,air}/r_{\mu,water}$. This rescaling is only an approximation because it does not account for the lower energies of the muons in water due to energy losses. The scale factor for measurement 1 and 2 is 1.250 ± 0.014. This gives $r_{Cher} = (13.58 \pm 0.30)$ mHz. The photons were detected either directly by one of the WLS PMTs or indirectly through the absorption and re-emission of the WLS. In this case, the wavelength sensitivity of the setup is determined by the *QE* of the PMT. Figure 3.6(a)

[5]We ignore the Cherenkov effect in air in this argument. Furthermore, the Cherenkov effect inside the WLS is assumed to be identical for the measurement in water and air, despite the lowering influence of the water on the energy spectrum of the muons causing the Cherenkov light in the WLS.

shows that the QE for the XP1911/UV is non-negligible between 200 nm and 600 nm. This window encloses the absorption curve of the WLS, which is non-negligible between 300 nm and 500 nm (see Figure 3.8).

An absolute detection efficiency can be calculated as

$$\epsilon_{abs} = \frac{r_{Cher}}{r_{\mu}} = (4.88 \pm 0.11)\%, \tag{5.4}$$

where the correlation between both rates was ignored in the error calculation.

It is very unlikely that the detected Cherenkov rate is a consequence of other radiative processes than the Cherenkov effect. The radiative processes discussed in Section 1.2.2.1 only become relevant at high muon energies, above 500 GeV. Looking back at Figure 1.7(a), it is clear that the majority of the muons at sea level have an energy of the order of 1 GeV. At 100 GeV, the muon flux has already decreased by a factor of 1000. For the observed number of trigger counts in this measurement, we can thus safely ignore the contribution of $E_{\mu} > 500$ GeV muons. Even if this contribution is not negligible, the above conclusion would still hold. The radiative processes produce light with a much higher energy than the Cherenkov light, which is either not seen by the WLS or by the PMT photocathode (wrong wavelength), or it is converted into many low-energy Cherenkov photons though a cascade (see Section 1.3.2). It is thus safe to conclude that Cherenkov light was detected by the setup.

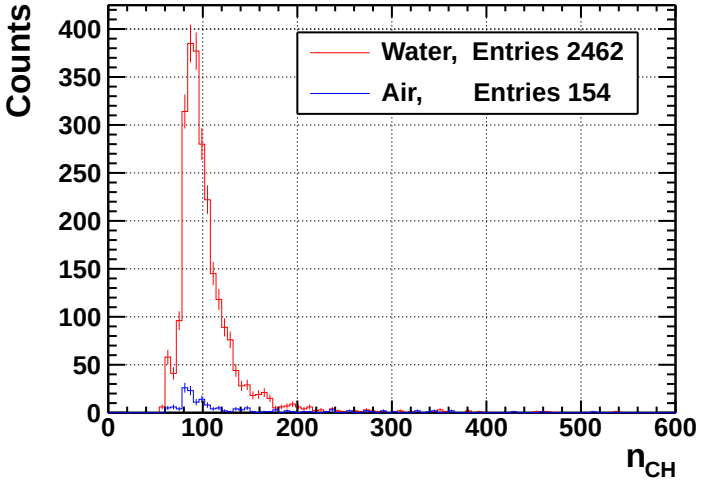

FIGURE 5.4: QDC spectrum for measurement 1 and 2 (see Table 5.2). The horizontal axis is cut off at $n_{CH} = 600$, causing a few events to be omitted from the spectrum.

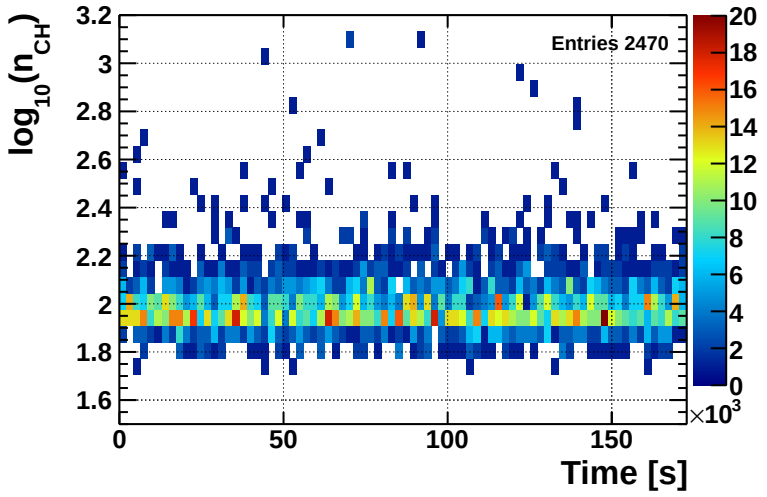

(a)

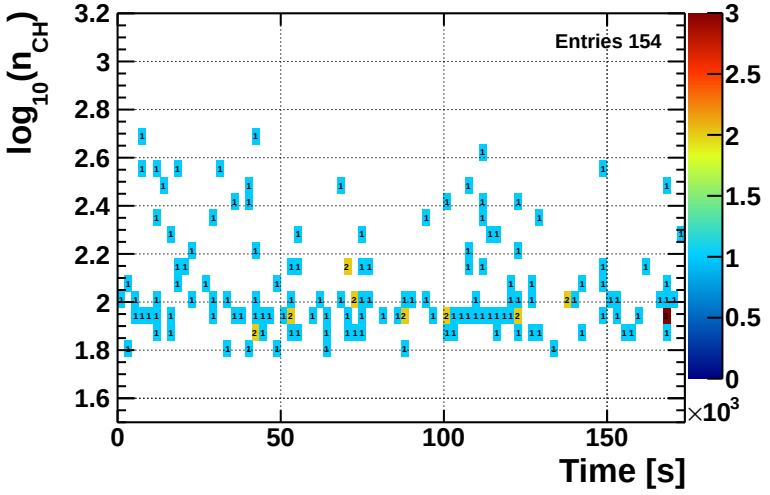

(b)

FIGURE 5.5: (a) Time dependence of the QDC spectrum for measurement 1 (see Table 5.2). (b) Time dependence of the QDC spectrum for measurement 2 (see Table 5.2). In both (a) and (b), parts of the PMT cathodes are also directly disposed to the water, allowing direct detection of Cherenkov light.

Cherenkov light detection through the WLS

With the free PMT cathode surfaces covered up, the setup is only sensitive to photon wavelengths in the absorption window of the WLS. Measurement 3 and 4 were carried out under the same conditions as measurement 1 and 2.

Figure 5.6 shows the QDC spectra for measurement 3 and 4. Figure 5.7 shows the time dependence of these QDC spectra. A peak value is observed at $n_{CH} \approx 90$ for both

measurements. The Cherenkov rate is now given by $r_{Cher} = (5.87 \pm 0.41)$ mHz[6]. This corresponds to an absolute detection efficiency

$$\epsilon_{abs} = \frac{r_{Cher}}{r_{\mu}} = (2.23 \pm 0.16)\%. \tag{5.5}$$

Comparison with ϵ_{abs} of measurement 1 (ignoring a rescaling factor of 1.05), shows that the efficiency has decreased approximately by a factor of 2. Removing the WLS from the tank and detecting Cherenkov light directly with the two PMTs allows to compare the efficiency of the Cherenkov light detection with and without WLS for this specific setup. Unfortunately, there was no time left to do such a measurement. Nevertheless, the present efficiency comparison indicates that Cherenkov light detection through the WLS goes very inefficiently in the current setup. This is most likely due to waveguide losses at the WLS surfaces, and to the fact that the WLS emission spectrum and the PMT *QE* are not adjusted to each other (see Figure 3.10).

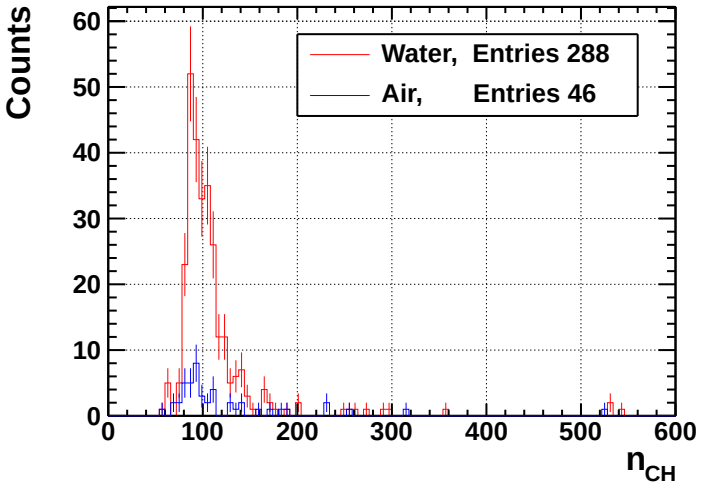

FIGURE 5.6: QDC spectrum for measurement 3 and 4 (see Table 5.2). The horizontal axis is cut off at $n_{CH} = 600$, causing one event to be omitted from the spectrum.

Consistency check

A few consistency checks can be done by comparing the different measurements:

– The muon fluxes listed in Table 5.2 show consistency. The two measurements in water have comparable muon rates, as do the two measurements in air. Note that the muon flux for the measurements in air is significantly larger than the muon flux in water. This is most likely due to the muon energy losses in the water, causing less muons to be detected by the lower trigger plane.

[6]The scale factor for measurement 3 and 4 is 1.290 ± 0.016.

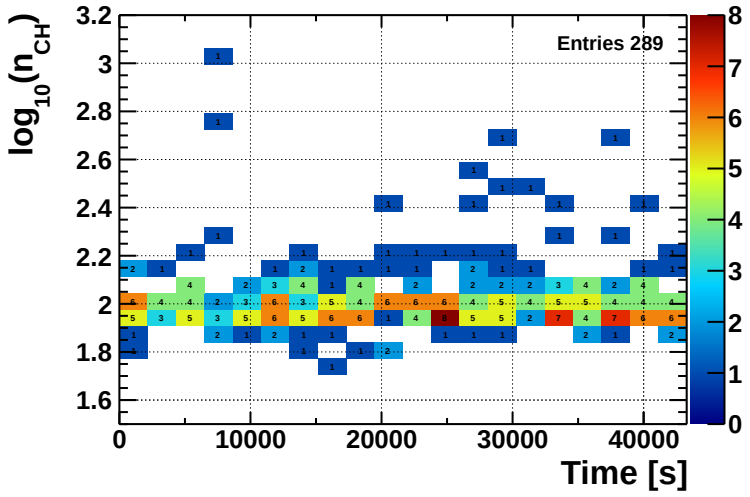

(a)

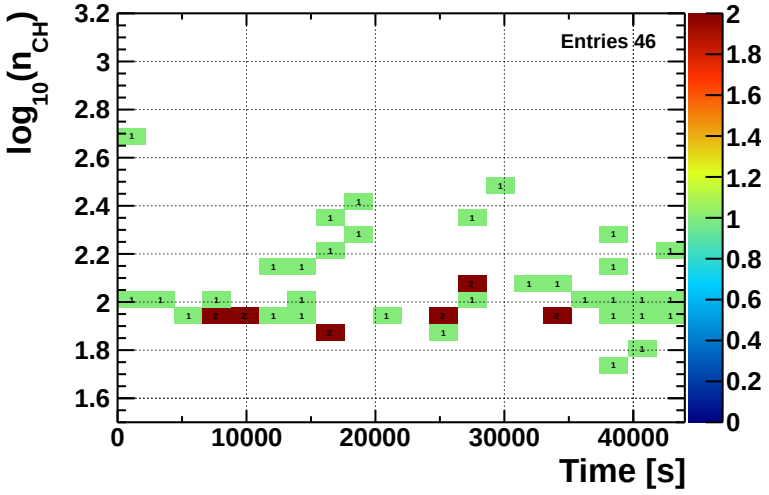

(b)

FIGURE 5.7: (a) Time dependence of the QDC spectrum for measurement 3 (see Table 5.2). (b) Time dependence of the QDC spectrum for measurement 2 (see Table 5.2). Only Cherenkov light detection through the WLS is possible in (a) and (b).

– The WLS rates in air are consistent. The WLS rate in water is higher for measurement 1 than for measurement 3. This is most likely due to shielding of the WLS PMT cathodes from direct Cherenkov light. In measurement 1, approximately half of the rate is accounted for by direct detection. This direct Cherenkov detection contribution is not present in measurement 3.

  The WLS rates of measurement 3 and 4 are inconsistent. It is unexpected to have a lower WLS activity in water than in air.

– Figure 5.8 shows QDC spectra of the first 12 hours of measurement 1 and 2.

These figures can be compared with the ones presented in Figure 5.7. Notice that the numbers in each bin have gone up by approximately a factor of 2 for the measurements in water, while this is not the case for the measurement in air. Figure 5.9(a) directly compares the QDC spectrum of both measurements on a logarithmic scale. These spectra are rescaled (divided by their surface) in Figure 5.9(b) to compare their shapes. These are in agreement, suggesting that the directly detected photons and indirectly detected photons cause similar signals in the WLS PMTs.

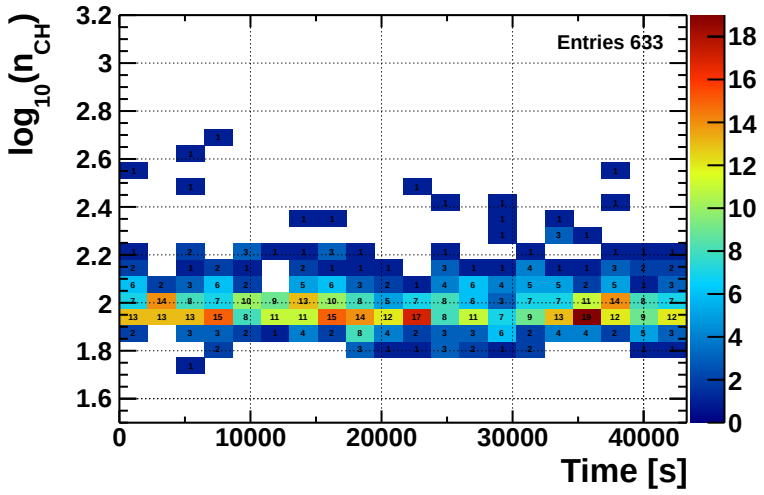

(a)

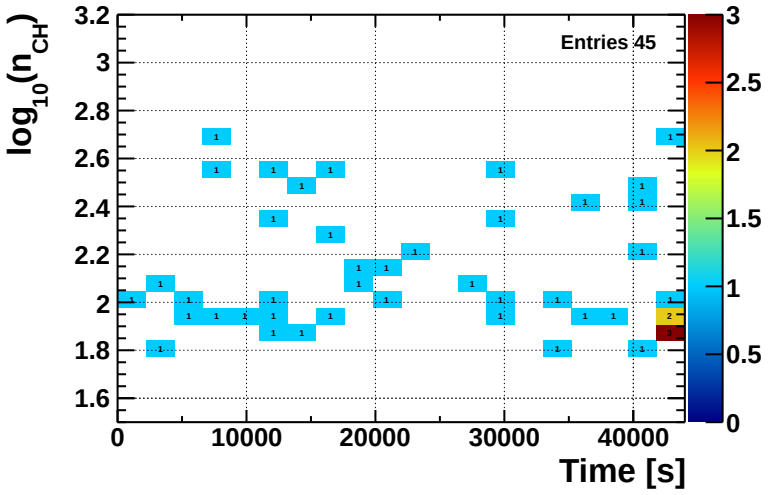

(b)

FIGURE 5.8: (a) Time dependence of the QDC spectrum during the first 12 hours of measurement 1 (see Table 5.2). (b) Time dependence of the QDC spectrum during the first 12 hours of measurement 2 (see Table 5.2).

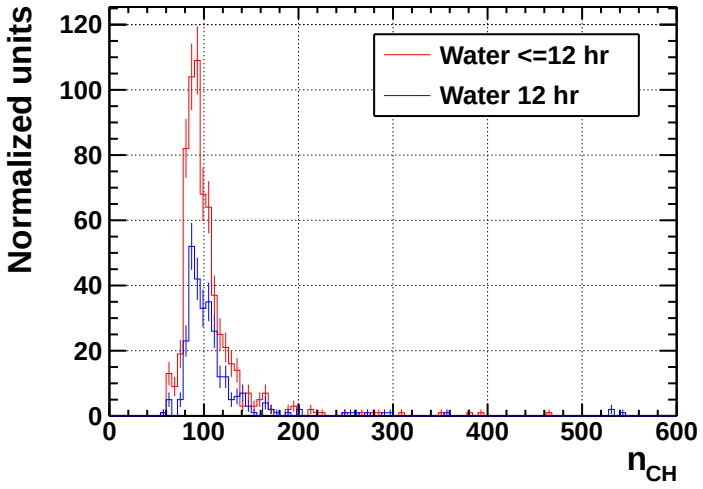

(a)

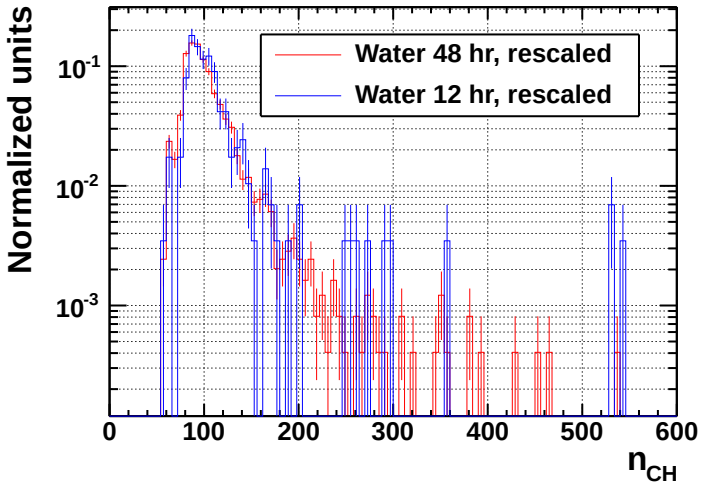

(b)

FIGURE 5.9: (a) Comparison of the QDC spectrum for measurement 1 (first 12 hours) and measurement 3 (see Table 5.2). (b) Comparison of the QDC spectrum for measurement 1 (first 12 hours) and measurement 3 through rescaling.

Chapter 6

Conclusions and outlook

The IceCube Neutrino Observatory is a giant neutrino telescope embedded in the Antarctic ice at the geographical South Pole, detecting atmospheric and extraterrestrial neutrinos through the Cherenkov effect. Cherenkov light is detected by optical sensors called Digital Optical Modules, mounted on strings in a one cubic kilometer grid structure in the ice. The light-collection and light-conversion to an electrical signal is done by 25 cm diameter photomultipliers. IceCube studies neutrinos with energies of the order of 100 GeV up to several PeV. DeepCore, a denser region of optical sensors in the centre of IceCube, lowers this energy threshold down to 10 GeV.

A further increase in optical sensor density allows to lower the IceCube energy threshold even more. The Precision IceCube Next Generation Upgrade (PINGU) will allow the detection of neutrinos with energies down to a few GeV. One of the main physics goals of PINGU is to do precision atmospheric neutrino oscillation measurements in the 5-20 GeV range, providing sensitivity to the still unknown neutrino mass hierarchy.

New concepts for optical sensors are being investigated as part of the R&D for PINGU and possible future upgrades of the IceCube detector. The goal of this master thesis research was to design and construct a working experimental setup to test the feasibility of using wavelength shifting materials (WLS) as the active part of a Cherenkov detector.

A WLS is a plastic scintillator doped with specific organic wavelength shifting molecules. It absorbs light of a certain wavelength and re-emits it at a higher wavelength in a random direction. Together with a PMT, a WLS can be used to detect Cherenkov light.

An optical sensor based on a WLS has two major advantages:

– Using the WLS as the light collector separates the light-collection process from the light-conversion process, opposed to the situation in an IceCube DOM where both

of this is done by the photocathode. This allows to couple to PMTs with small photocathodes, and hence limit the noise rate. This is a very important feature for low-energy neutrino detection. Between the collection and conversion process, the WLS also acts as a waveguide. Refraction losses at the edges of the WLS should be taken care of, as they lower the overall detection efficiency.

– If made from the appropriate material, the WLS can shift the absorbed Cherenkov photons to a higher wavelength better suited for PMT readout.

The constructed setup consists of a water tank filled with distilled water, in which a WLS bar of the type BC-482A with dimensions 10 cm × 0.5 cm × 80 cm is mounted. The WLS bar is read out by two XP1911/UV PMTs with a photocathode diameter of 15 mm. A trigger, consisting of a scintillator plate above and below the watertank, registers the atmospheric muons causing the Cherenkov light inside the detector. A temporal coincidence check of trigger signals and WLS signals makes it possible to test the Cherenkov detection efficiency of the WLS-PMT combination. A MC simulation was carried out to determine the best WLS position[1] inside the water tank.

Measurements were done both in air and water, where the former served as a background measurement for the latter, assuming from results of the simulations that no Cherenkov light is detected in air with the current setup. Comparing the results from a 12 hour measurement in water and air, it was concluded that Cherenkov light was detected through the WLS with an absolute detector efficiency of (2.23 ± 0.16) %. From a 48 hour measurement with the WLS in water and air, but in which parts of the photocathodes were directly disposed to the medium in the tank, an absolute detector efficiency of (4.88 ± 0.11) % was found. This increase by a factor of two, suggests that in the current setup two photocathodes directly disposed to the water[2] are as efficient as the WLS coupled to the same two PMT cathodes[3]. Hence, there is still a long way to go before a definite design of an efficient optical module based on a WLS (a WOM) is achieved. It must be noted that the physical and geometrical properties of the WLS bar and PMTs used for the current measurements were not perfectly adjusted to each other. The WLS shifts the absorbed photons away from the PMT *QE* peak, the bar-shape of the WLS allows refraction losses at four surfaces, and the PMTs are coupled to only 1/10th of the readout surfaces.

Now that Cherenkov light detection in water through a WLS is established, further research must be done. The first task before proceeding with new measurements is to

[1] Of those positions allowed by the design.
[2] More precisely about 90 % of the area of the two photocathodes.
[3] More precisely coupled to the remaining 10 % of the photocathode areas.

do an absolute calibration of the setup, such that the QDC can be used to its full extent and an unambiguous interpretation of the measured spectra becomes possible.

A few interesting measurements would be:

- The influence of the water volume can be checked by lowering the water level in the tank step by step and finding the relation between detector efficiency and water level. This relation can then be compared with the MC predictions.
- Currently, both WLS PMT signals are added together before they are tested for coincidence with the trigger signal. An extension of the readout system consist in treating both WLS signals separately in the readout chain, thus allowing to check the uniformity of the WLS response.
- The effect of the wavelength-shifting process could be checked by comparing the response of a WLS to that of a plain scintillator made up from the same organic material as the WLS. The WLS and scintillator samples can each be coupled to one of the readout PMTs, such that their QDC spectra are directly comparable.
- Readout over the whole WLS end surface, rather than only 1/10th of the surface could significantly increase the detection efficiency. As one of the key features of a WLS optical sensor is the possibility to limit the photocathode surface and consequent noise rate, it is important to look for an efficient light guide coupling between the WLS bar and the PMT surface rather than using more PMTs for readout.
- Different WLS geometries could be studied. Particularly, a hollow tube geometry has the interesting feature that it acts as a good waveguide and mainly shows refraction losses at the two end surfaces, which should evidently be used as the PMT readout surfaces. Additionally, reflective coatings could further limit waveguide losses.

The MC simulation could be used to check the feasibility of using other WLS-PMT combinations to detect Cherenkov light. It might also be interesting to do an absorption measurement of the water, to allow a decoupling of the WLS detection efficiency from the properties of the distilled water.

Appendix A

Relative calibration

The QDC spectra as a function of time for the PMT calibration measurements discussed in Section 5.1.2.

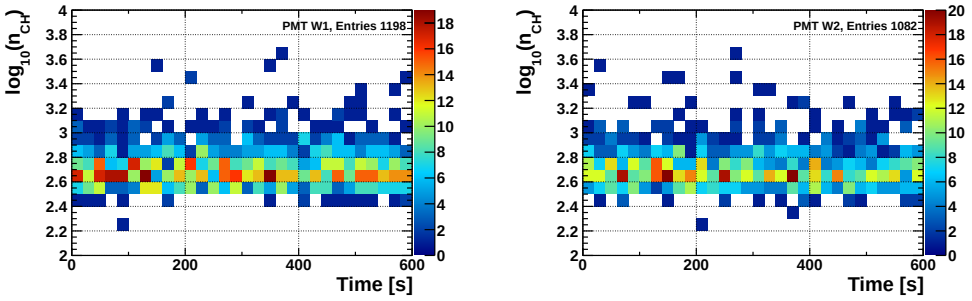

(a) (b)

FIGURE A.1: Time dependence of the QDC spectra of the PMTs used for the WLS readout: PMT W1-W2. The corresponding high voltages and CFD thresholds can be found in Table 5.1.

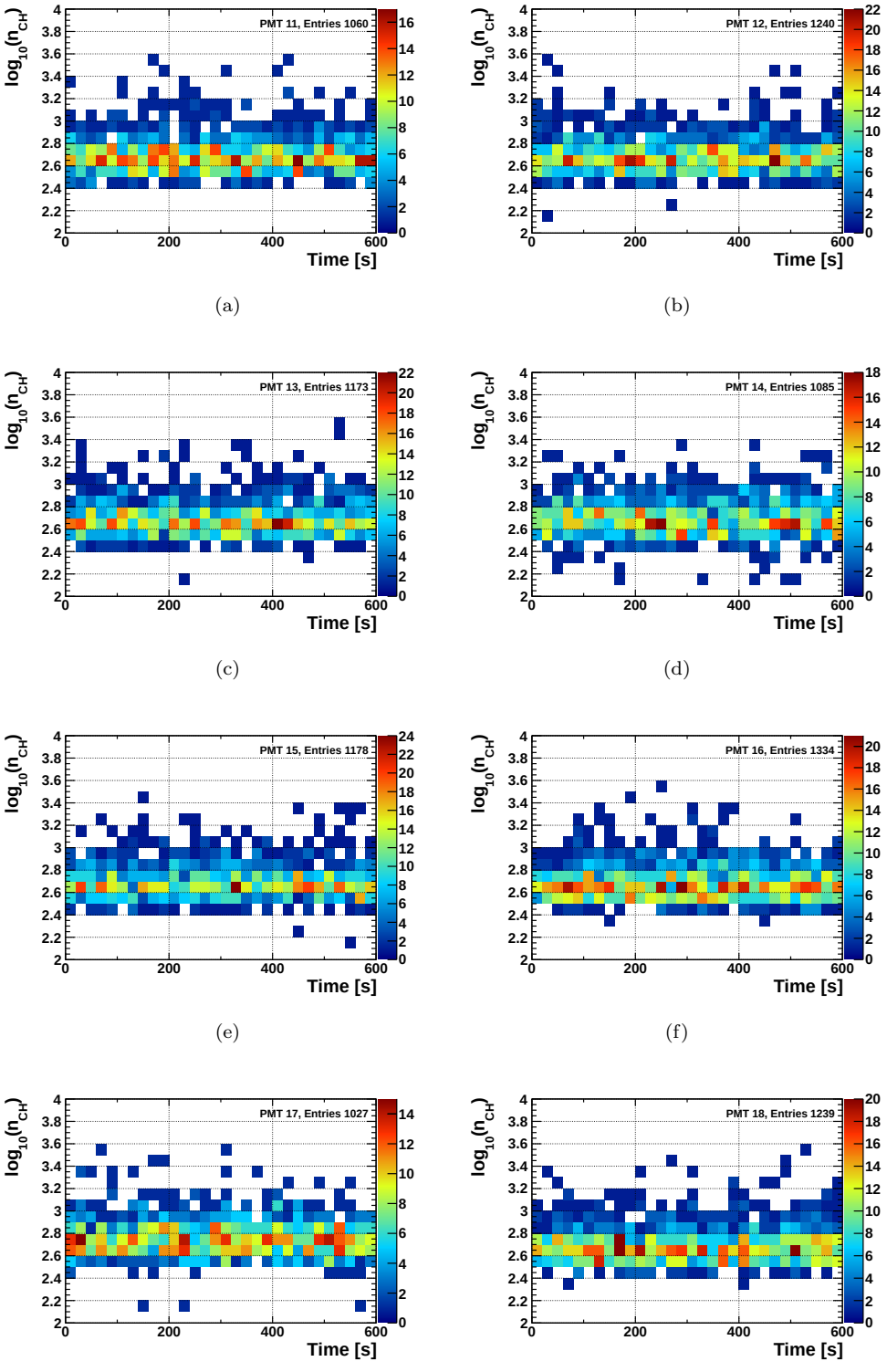

(a) (b) (c) (d) (e) (f) (g) (h)

FIGURE A.2: Time dependence of the QDC spectra of the PMTs used in trigger 1: PMT 11-18. The corresponding high voltages and CFD thresholds can be found in Table 5.1.

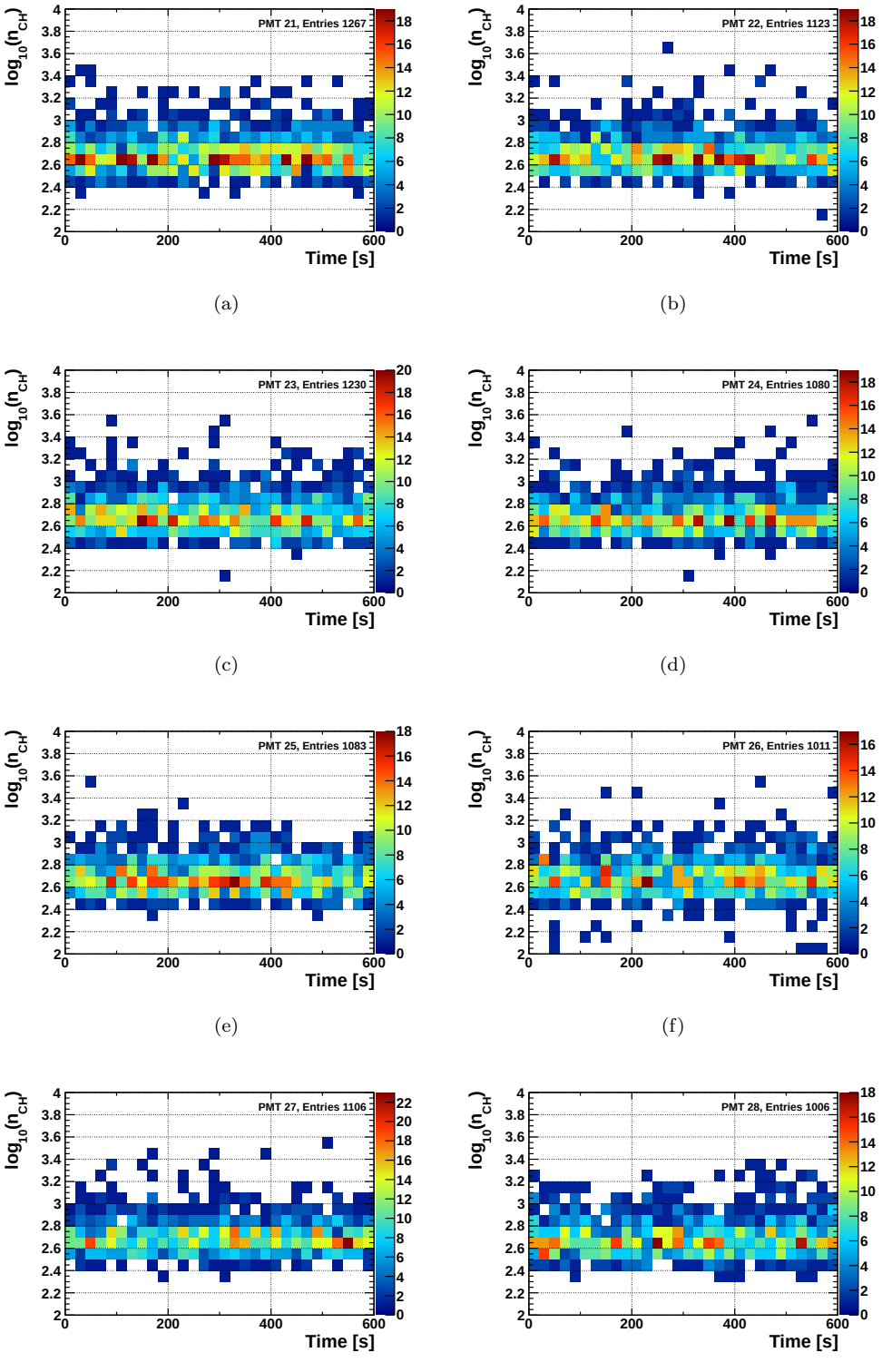

FIGURE A.3: Time dependence of the QDC spectra of the PMTs used in trigger 2: PMT 21-28. The corresponding high voltages and CFD thresholds can be found in Table 5.1.

Bibliography

[1] J.J. Thomson. Cathode Rays. *Philosophical Magazine*, 3(44):293–316, 1897. URL http://web.ihep.su/dbserv/compas/src/thomson97/eng.pdf.

[2] A. Einstein. Uber einen die Erzeugung und Verwandlung des Lichtes betreffenden heuristischen Gesichtspunkt. *Annalen der Physik*, 6(17):132–148, 1905. URL http://www.physik.uni-augsburg.de/annalen/history/einstein-papers/1905_17_132-148.pdf.

[3] A. Einstein. Uber die von der molekularkinetischen Theorie der Wärme geforderte Bewegung von in ruhenden Flüssigkeiten suspendierten Teilchen. *Annalen der Physik*, 8(17):549–560, 1905. URL http://www.physik.uni-augsburg.de/annalen/history/einstein-papers/1905_17_549-560.pdf.

[4] A. Einstein. Zur Elektrodynamik bewegter Körper. *Annalen der Physik*, 10(17): 891–921, 1905. URL http://onlinelibrary.wiley.com/doi/10.1002/andp.19053221004/pdf.

[5] A. Einstein. Ist die Trägheit eines Körpers von seinem Energieinhalt abhängig? *Annalen der Physik*, 13(18):639–641, 1905. URL http://www.physik.uni-augsburg.de/annalen/history/einstein-papers/1905_18_639-641.pdf.

[6] L. Hoddeson, L. Brown, M. Riordan, and M. Dresden, editors. *The Rise of The Standard Model*. Cambridge University Press, Cambridge, 1979.

[7] E. Rutherford. The scattering of α and β particles and the structure of the atom. *Philosophical Magazine*, 21(6):669–688, 1911.

[8] E. Rutherford. Collision of α Particles with Light Atoms IV. An Anomalous Effect in Nitrogen. *Philosophical Magazine*, 37:581, 1919. URL http://cds.cern.ch/record/262759.

[9] J. Chadwick. Possible Existence of a Neutron. *Nature*, 129(3252):312, 1932. URL http://web.mit.edu/22.54/resources/Chadwick.pdf.

[10] L.M. Brown. The idea of the neutrino. *Physics Today*, pages 23–28, 1978. URL http://ddd.uab.cat/pub/ppascual/ppascualapu/ppascualapu_41_001@benasque.pdf.

[11] E. Fermi. Fermi's Theory of Beta Decay (English translation by Fred L. Wilson, 1968). *American Journal of Physics*, 36(12):1150–1161, 1934. URL http://microboone-docdb.fnal.gov/cgi-bin/RetrieveFile?docid=953;filename=FermiBetaDecay1934.pdf;version=1.

[12] C.L. Cowan, F. Reines, F.B. Harrison, H.W. Kruse, and A.D. McGuire. Detection of the Free Neutrino: a Confirmation. *Science*, 124(3212):103–104, July 1956. URL http://www.sciencemag.org/content/124/3212/103.

[13] C. D. Anderson. The Positive Electron. *Physical Review*, 43(6):491–494, 1933. URL http://prola.aps.org/pdf/PR/v43/i6/p491_1.

[14] P.A.M. Dirac. The Quantum Theory of the Electron. *Proceedings of the Royal Society A*, 117(778):610–624, 1928. URL http://rspa.royalsocietypublishing.org/content/117/778/610.

[15] O. Chamberlain, E. Segrè, C. Wiegand, and T. Ypsilantis. Observation of Antiprotons. *Physical Review*, 100(3):947–950, 1955. URL http://prola.aps.org/pdf/PR/v100/i3/p947_1.

[16] S.H. Neddermeyer and C.D. Anderson. Note on the Nature of Cosmic-Ray Particles. *Physical Review*, 51(10):884–886, 1937. URL http://prola.aps.org/pdf/PR/v51/i10/p884_1.

[17] C.F. Powell, G.P.S. Occhialini, H. Muirhead, and C.M.G. Latter. Processes Involving Charged Mesons. *Nature*, 159:694–697, 1947. URL http://www.nature.com/nature/journal/v159/n4047/pdf/159694a0.pdf.

[18] G.D. Rochester and C.C. Butler. Evidence for the Existence of New Unstable Elementary Particles. *Nature*, 160:855–857, 1947. URL http://www.nature.com/nature/journal/v160/n4077/pdf/160855a0.pdf.

[19] T.S. Needels and C.E. Nielsen. A Continuously Sensitive Cloud Chamber. *Review of Scientific Instruments*, 21(12):976–977, 1950. URL http://rsi.aip.org/resource/1/rsinak/v21/i12/p976_s1.

[20] D.A. Glaser. Some Effects of Ionizing Radiation on the Formation of Bubbles in Liquids. *Physical Review*, 87(4):665, 1952. URL http://prola.aps.org/pdf/PR/v87/i4/p665_1.

[21] R. Hofstadter and R.W. McAllister. Electron Scattering from the Proton. *Physical Review*, 98:217, 1955. URL http://www.nobelprize.org/nobel_prizes/physics/laureates/1961/hofstadter-lecture.pdf.

[22] M. Gell-Mann. The Eightfold Way: A theory of strong interaction symmetry. *Synchroton Laboratory Report CTSL-20, CALTECH (unpublished)*, page 52, 1961. URL http://www.osti.gov/accomplishments/documents/fullText/ACC0113.pdf.

[23] Y. Ne'eman. Derivation of Strong Interactions from a Gauge Invariance. *Nuclear Physics*, 26(2):222–229, 1961. URL http://www.sciencedirect.com/science/article/pii/0029558261901341.

[24] V.E. Barnes *et al.* Observation of a Hyperon with Strangeness Minus Three. *Physics Review Letters*, 12(8):204–206, 1964. URL http://prl.aps.org/pdf/PRL/v12/i8/p204_1.

[25] M. Gell-Mann. A Schematic Model of Baryons and Mesons. *Physics Letters*, 8(3):214–215, 1964. URL http://www.sciencedirect.com/science/article/pii/S0031916364920013.

[26] G. Zweig. An SU(3) Model for Strong Interaction and its Breaking. *CERN Report No.8182/TH.401*, 1964. URL http://cds.cern.ch/record/352337/files/CM-P00042883.pdf.

[27] E.D. Bloom *et al.* High-Energy Inelastic ep Scattering at 6 degrees and 10 degrees. *Physical Review Letters*, 23(16):930–934, 1969. URL http://prl.aps.org/pdf/PRL/v23/i16/p930_1.

[28] M. Breidenbach *et al.* Observed Behavior of Highly Inelastic Electron-Proton Scattering. *Physical Review Letters*, 23(16):935–939, 1969. URL http://prl.aps.org/pdf/PRL/v23/i16/p935_1.

[29] O.W. Greenberg. Spin and Unitary-Spin Independence in a Paraquark Model of Baryons and Mesons. *Physical Review Letters*, 13(20):598–602, 1964. URL http://prl.aps.org/pdf/PRL/v13/i20/p598_1.

[30] O.W. Greenberg. A Theory of the Fundamental Interactions. *Annals of Physics*, 2(5):407–434, 1957. URL http://www.sciencedirect.com/science/article/pii/00034916579001552.

[31] C.S. Wu, E. Ambler, R.W. Hayward, D.D. Hoppes, and R.P. Hudson. Experimental Test of Parity Conservation in Beta Decay. *Physical Review*, 105(4):1413–1415, 1957. URL http://prola.aps.org/pdf/PR/v105/i4/p1413_1.

[32] T.D. Lee and C.N. Yang. Question of Parity Conservation in Weak Interactions. *Physical Review*, 104(1):254–258, 1957. URL http://prola.aps.org/pdf/PR/v104/i1/p254_1.

[33] G. Danby, J.-M. Gaillard, K. Goulianos, L.M. Lederman, N. Mistry, M. Schwartz, and J. Steinberger. Observation of High-Energy Neutrino Reactions and the Existence of Two Kinds of Neutrinos. *Physical Review Letters*, 9(1):36–44, 1962. URL http://prl.aps.org/pdf/PRL/v9/i1/p36_1.

[34] N. Cabibbo. Unitary Symmetry and Leptonic Decays. *Physical Review Letters*, 10(12):531–533, 1963. URL http://prl.aps.org/pdf/PRL/v10/i12/p531_1.

[35] S. Glashow, J. Iliopolis, and L. Maiani. Weak Interactions with Lepton-Hadron Symmetry. *Physical Review D*, 2(7):1285–1292, 1970. URL http://prd.aps.org/pdf/PRD/v2/i7/p1285_1.

[36] S. Weinberg. A Model of Leptons. *Physical Review Letters*, 19(21):1264–1266, 1967. URL http://prl.aps.org/pdf/PRL/v19/i21/p1264_1.

[37] A. Salam. Weak and Electromagnetic Interactions. *Proceedings Of The Nobel Symposium, Lerum, Sweden*, pages 367–377, 1968. URL http://inspirehep.net/record/53083.

[38] F. Englert and R. Brout. Broken Symmetry and the Mass of Gauge Vector Mesons. *Physical Review Letters*, 13(9):321–323, 1964. URL http://prl.aps.org/pdf/PRL/v13/i9/p321_1.

[39] P. Higgs. Broken Symmetries and the Masses of Gauge Bosons. *Physical Review Letters*, 13(16):508–509, 1964. URL http://prl.aps.org/pdf/PRL/v13/i16/p508_1.

[40] G.S. Guralnik, C.R. Hagen, and T.W.B. Kibble. Global Conservation Laws and Massless Particles. *Physical Review Letters*, 13(20):585–587, 1964. URL http://prl.aps.org/pdf/PRL/v13/i20/p585_1.

[41] M. Kobayashi and T. Maskawa. CP-Violation in the Renormalizable Theory of Weak Interaction. *Progress of Theoretical Physics*, 49(2):652–657, 1973. URL http://ptp.oxfordjournals.org/content/49/2/652.full.pdf.

[42] G.H. Christenson, J.W. Cronin, V.L. Fitch, and R. Turlay. Evidence for the 2π Decay of the K_2^0 Meson. *Physical Review Letters*, 13(4):138–140, 1964. URL http://prl.aps.org/pdf/PRL/v13/i4/p138_1.

[43] K.G. Wilson. Confinement of quarks. *Physical Review D*, 10(8):2445–2459, 1974. URL http://prd.aps.org/pdf/PRD/v10/i8/p2445_1.

[44] D.J. Gross and F. Wilczek. Ultraviolet Behavior of Non-Abelian Gauge Theories. *Physical Review Letters*, 13(26):1343–1346, 1973. URL http://prl.aps.org/pdf/PRL/v30/i26/p1343_1.

[45] D.H. Politzer. Reliable Perturbative Results for Strong Interactions? *Physical Review Letters*, 13(26):1346–1349, 1973. URL http://prl.aps.org/pdf/PRL/v30/i26/p1346_1.

[46] J.-E. Augustin *et al.* Discovery of a Narrow Resonance in e^+e^- Annihilation. *Physical Review Letters*, 33(23):1406–1408, 1974. URL http://prl.aps.org/pdf/PRL/v33/i23/p1406_1.

[47] M.L. Perl *et al.* Evidence for Anomalous Lepton Production in e^+e^- Annihilation. *Physical Review Letters*, 35(22):1489–1492, 1975. URL http://prl.aps.org/pdf/PRL/v35/i22/p1489_1.

[48] S.W. Herb *et al.* Observation of a Dimuon Resonance at 9.5 GeV in 400-GeV Proton-Nucleus Collisions. *Physical Review Letters*, 39(5):255–257, 1977. URL http://prl.aps.org/pdf/PRL/v39/i5/p252_1.

[49] D.P. Barber *et al.* Discovery of Three-Jet Events and a Test of Quantum Chromodynamics at PETRA. *Physical Review Letters*, 43(12):830–833, 1979. URL http://prl.aps.org/pdf/PRL/v43/i12/p830_1.

[50] J.J. Aubert *et al.* The ratio of the nucleon structure functions F_2^N for iron and deuterium. *Physics Letters B*, 123(3–4):275–278, 1983. URL http://www.sciencedirect.com/science/article/pii/0370269383904379.

[51] G. Arnison *et al.* Experimental Observation of Lepton Pairs of Invariant Mass around 95 GeV/c^2 at the CERN SPS Collider. *Physics Letters B*, 126(5):398–410, 1983. URL http://www.sciencedirect.com/science/article/pii/0370269383901880.

[52] S. Abachi *et al.* Search for High Mass Top Quark Production in $\bar{p}p$ Collisions at $\sqrt{s} = 1.8$ TeV. *Physical Review Letters*, 74(13):2422–2426, 1995. URL http://prl.aps.org/pdf/PRL/v74/i13/p2422_1.

[53] F. Abe *et al.* Observation of Top Quark Production in $\bar{p}p$ Collisions with the Collider Detector at Fermilab. *Physical Review Letters*, 74(14):2626–2631, 1995. URL http://prl.aps.org/pdf/PRL/v74/i14/p2626_1.

[54] K. Kodama *et al.* Observation of Tau Neutrino Interactions. *Physics Letters B*, 504(3):218–224, 2001. URL http://www.sciencedirect.com/science/article/pii/S0370269301003070.

[55] ATLAS collaboration. Observation of a New Particle in the Search for the Standard Model Higgs Boson with the ATLAS Detector at the LHC. *Physics Letters B*, 716 (1):1–29, 2012. URL http://www.sciencedirect.com/science/article/pii/S037026931200857X.

[56] CMS collaboration. Observation of a New Boson at a Mass of 125 GeV with the CMS Experiment at the LHC. *Physics Letters B*, 716(1):30–61, 2012. URL http://www.sciencedirect.com/science/article/pii/S0370269312008581.

[57] Y. Fukuda *et al.* Evidence for Oscillation of Atmospheric Neutrinos. *Physical Review Letters*, 81(8):1562–1567, 1998. URL http://prl.aps.org/pdf/PRL/v81/i8/p1562_1.

[58] Q.R. Ahmad *et al.* Measurement of the Rate of $\nu_e + d \rightarrow p + p + e^-$ Interactions Produced by 8B Solar Neutrinos at the Sudbury Neutrino Observatory. *Physical Review Letters*, 87(7):071301–1–071301–6, 2001. URL http://prl.aps.org/pdf/PRL/v87/i7/e071301.

[59] P. Ramond. *Journeys Beyond The Standard Model*. Westview Press, Boulder, 2004.

[60] W. Gerlach and O. Stern. Das magnetische Moment des Silberatoms. *Zeitschrift für Physik*, 9(1):353–355, 1922. URL http://www.kip.uni-heidelberg.de/matterwaveoptics/teaching/archive/ws07-08/SternGerlach_orig2.pdf.

[61] Electron-Positron Annihilation: Feynman Diagram, 2006. URL http://en.wikipedia.org/wiki/File:Electron-positron-annihilation.svg. Visited on 2013-05-11.

[62] F. Mauger. β Decay: Feynman Diagram, 2004. URL http://nemo.in2p3.fr/physics/sm.php. Visited on 2013-05-11.

[63] Proton-Antiproton Collision: Feynman Diagram. URL http://teachers.web.cern.ch/teachers/archiv/HST2002/feynman/examples.htm#Example%2013. Visited on 2013-05-11.

[64] Higgs 4 Lepton Decay Channel: Feynman Diagram. URL http://www.guardian.co.uk/science/life-and-physics/2012/may/23/cern-lhc-sound. Visited on 2013-05-11.

[65] K. Winter. *Neutrino Physics, 2nd Ed.* Cambridge University Press, Cambridge, 2000.

[66] J. Baez. Renormalization Made Easy, 2009. URL http://math.ucr.edu/home/baez/renormalization.html. Visited on 2013-05-01.

[67] V.A. Kuzmin, V.A. Rubakov, and M.A. Shaposhnikov. On Anomalous Electroweak Baryon-Number Non-Conservation in the Early Universe. *Physics Letters B*, 155(1–2):36–42, 1985. URL http://www.sciencedirect.com/science/article/pii/0370269385910287.

[68] J. Schechter and J. Valle. Neutrino Decay and Spontaneous Violation of Lepton Number. *Physical Review D*, 25(3):774–783, 1982. URL http://prd.aps.org/pdf/PRD/v25/i3/p774_1.

[69] X. Sarazin. Review of Double Beta Experiments. *Available on arXiv:1210.7666v1 [physics.ins-det]*, 2012. URL http://arxiv.org/pdf/1210.7666v1.pdf.

[70] Collaboration ALEPH *et al.* Precision Electroweak Measurements on the Z Resonance. *Physics Reports*, 427(5–6):257–454, 2006. URL http://www.sciencedirect.com/science/article/pii/S0370157305005119.

[71] L. Wolfenstein. Neutrino Oscillations in Matter. *Physical Review D*, 17(9):2369–2374, 1978. URL http://prd.aps.org/pdf/PRD/v17/i9/p2369_1.

[72] S. Goswami *et al.* Global Analysis of Neutrino Oscillation. *Nuclear Physics B - Proceedings Supplements*, 143:121–128, 2005. URL http://www.sciencedirect.com/science/article/pii/S0920563205000988.

[73] Neutrino Mass Hierarchy. URL http://inspirehep.net/record/1114323/files/Neutrinos_figs_3nuspic.png. Visited on 2013-04-11.

[74] Electromagnetic Spectrum. URL http://epo.sonoma.edu/EposChronicles/?tag=spectrum. Visited on 2013-05-11.

[75] N. Whitehorn, C. Kopper, N. Neilson, J. van Santen, D. Gora, W. Weaver, L. Gerhardt, and C-H Ha. Evidence for High-Energy Extraterrestrial Neutrinos at the IceCube Detector. *Unpublished*, 2013.

[76] Status and Perspective of Astroparticle Physics in Europe. 2007. URL http://www.aspera-eu.org/images/stories/files/Roadmap.pdf.

[77] J.W. Cronin. Cosmic Rays: the Most Energetic Particles in the Universe. *Reviews of Modern Physics*, 71(2):S165–S172, 1999. URL http://rmp.aps.org/pdf/RMP/v71/i2/pS165_1.

[78] K. Greisen. End to the Cosmic-Ray Spectrum? *Physical Review Letters*, 16(17):748–750, 1966. URL http://prl.aps.org/pdf/PRL/v16/i17/p748_1.

[79] G.T. Zatsepin and V.A. Kuzmin. Upper Limit of the Spectrum of Cosmic Rays. *JETP Letters*, 4(3):78–80, 1966. URL http://www.jetpletters.ac.ru/ps/1624/article_24846.pdf.

[80] S. Swordy. Primary Cosmic Ray Energy Spectrum, 2002. URL http://physik.uibk.ac.at/hephy/lectures/seminar/2002ws/article2/. Visited on 2013-05-12.

[81] CERN. Cosmic Ray Air Shower, 2008. URL http://www.expeditions.udel.edu/antarctica08/blog-dec-12-2008.html. Visited on 2013-05-12.

[82] J. Beringer *et al.* (Particle Data Group). Review of Particle Physics. *Physical Review D*, 86(1):010001, 2012. URL http://prd.aps.org/pdf/PRD/v86/i1/e010001.

[83] O.C. Allkofer *et al.* The Absolute Cosmic Ray Spectrum at Sea Level. *Physics Letters B*, 36(4):425–427, 1971. URL http://www.sciencedirect.com/science/article/pii/0370269371907416.

[84] B.C. Rastin. A Study of the Muon Charge Ratio at Sea Level within the Momentum Range 4 to 2000 GeV/c. *Journal of Physics G: Nuclear Physics*, 10(11): 1629–1638, 1984. URL http://iopscience.iop.org/0305-4616/10/11/018/pdf/0305-4616_10_11_018.pdf.

[85] A. Astbury and D. Axen. Comparison of GEANT4 simulation of atmospheric cosmic rays with measured terrestrial muon and neutron spectra. *TRIUMF Publications Office*, 2006. URL http://publications.triumf.ca/publications/pub/arch06/pp-06-14.pdf.

[86] S. Cecchini and M. Spurio. Atmospheric Muons: Experimental Aspects. *Available on arXiv: arXiv:1208.1171v1 [astro-ph.EP]*, 2012. URL http://arxiv.org/pdf/1208.1171.pdf.

[87] J.N. Bahcall. Neutrinos from the Sun. *Scientific American*, 221 (1):28–37, 1969. URL http://www.sns.ias.edu/~jnb/Papers/Popular/Scientificamerican69/scientificamerican69.html.

[88] F. Sulehria. Proton-Proton Chain, 2005. URL http://www.novacelestia.com/images/stars_proton-proton_chain.html. Visited on 2013-05-12.

[89] J.N. Bahcall, A.M. Serenelli, and S. Basu. New Solar Opacities, Abundances, Helioseismology, and Neutrino Fluxes. *The Astrophysical Journal Letters*, 621(1): L85–L88, 2005. URL http://arxiv.org/pdf/astro-ph/0412440v3.pdf.

[90] Max Planck Institute for Astrophysics. Millenium Simulation Project, 2005. URL http://www.mpa-garching.mpg.de/galform/virgo/millennium/. Visited on 2013-05-12.

[91] D. Hubert and A. Davour. Search for Neutralino Dark Matter with the AMANDA Neutrino Telescope. *Proceedings of the 30th International Cosmic Ray Conference*, 4:709–712, 2007.

[92] N. Spooner. Direct and Indirect Searches for WIMP Dark Matter. *Unpublished*, 2001. URL http://www.slac.stanford.edu/econf/C010630/papers/P401.PDF.

[93] R. Gandhi, C. Quigg, M.H. Reno, and I. Sarcevic. Ultrahigh-Energy Neutrino Interactions. *Astroparticle Physics*, 5:81–110, 1996. URL http://homepages.ulb.ac.be/~khanson/particle-astrophysics/w09/GQRS-APP5.pdf.

[94] M. Bouwhuis. *Detection of Neutrinos form Gamma-Ray Bursts*. Unknown, Unknown, 2005.

[95] E. Blaufuss. GRB 130427A: High-Energy Neutrino Search. *GCN CIRCULAR*, 2013. URL http://gcn.gsfc.nasa.gov/gcn3/14520.gcn3.

[96] B.G. Marsden. Supernova 1987A in the Large Magellanic Cloud. *IAU CIRCULAR*, 1987. URL http://www.cbat.eps.harvard.edu/iauc/04300/04316.html.

[97] A. Bhattacharya, R. Gandhi, W. Rodejohann, and A. Watanabe. The Glashow resonance at IceCube: signatures, event rates and pp vs. pγ interactions. *Available on arXiv: arXiv:1108.3163v2 [astro-ph.HE]*, 2011. URL http://arxiv.org/pdf/1108.3163v2.pdf.

[98] M. Bouwhuis. *Detection of Neutrinos from Gamma-Ray Bursts*. PhD thesis, Universiteit van Amsterdam, May 2005.

[99] C. Grupen. *Particle Detectors*. Cambridge University Press, Cambridge, 1996.

[100] J. Fricke and T. Tillotson. Aerogels: Production, Characterization, and Applications, 1997. URL http://www.sciencedirect.com/science/article/pii/S0040609096094412. Visited on 2013-05-21.

[101] J.V. Jelley. *Cherenkov Radiation and its Applications*. Pergamon Press, London, 1958.

[102] Sudbury Neutrino Observatory. The Official SNO Home Page, 2013. URL http://www.sno.phy.queensu.ca/. Visited on 2013-05-22.

[103] Kamioka Observatory. The Official Super-Kamiokande Home Page, 2013. URL http://www-sk.icrr.u-tokyo.ac.jp/index-e.html. Visited on 2013-05-22.

[104] M.G. Aartsen *et al.* Measurement of Atmospheric Neutrino Oscillations with IceCube. *Available on arXiv: arXiv:1305.3909v1 [hep-ex]*, 2013. URL http://arxiv.org/pdf/1305.3909v1.pdf.

[105] F.P. An. *et al.* Improved Measurement of Electron Antineutrino Disappearance at Daya Bay. *Available on arXiv:1210.6327v2 [hep-ex]*, 2012. URL http://dayawane.ihep.ac.cn/docs/1210.6327v1.pdf.

[106] R.P. Litchfield. Direct Measurement of θ_{13}. *Available on arXiv:1209.3884 [hep-ex]*, 2012. URL http://arxiv.org/pdf/1209.3884v2.pdf.

[107] F.P. An. *et al.* Observation of a First ν_τ Candidate Event in the OPERA Experiment in the CNGS Beam. *Physics Letters B*, 691(3):138–145, 2010. URL http://www.sciencedirect.com/science/article/pii/S0370269310007537.

[108] T2K Collaboration. The Official T2K Home Page, 2013. URL http://t2k-experiment.org/. Visited on 2013-05-22.

[109] V.N. Aseev. *et al.* An Upper Limit on Electron Antineutrino Mass from Troitsk Experiment. *Physical Review D*, 84(11):112003–1–112003–9, 2011. URL http://prd.aps.org/pdf/PRD/v84/i11/e112003.

[110] KATRIN collaboration. The Official KATRIN Home Page, 2013. URL http://www.katrin.kit.edu/. Visited on 2013-05-22.

[111] SuperNemo. SuperNemo Group Page University of Manchester, 2013. URL http://www.hep.man.ac.uk/SuperNemo/. Visited on 2013-05-22.

[112] Majorana collaboration. Majorana Group Page University of Washington, 2013. URL http://www.npl.washington.edu/majorana/. Visited on 2013-05-22.

[113] F. Halzen and S. Klein. Invited Review Article: IceCube: An instrument for neutrino astronomy. *Review of Scientific Instruments*, 81:081101–1 – 081101–24, 2010. URL http://rsi.aip.org/resource/1/rsinak/v81/i8/p081101_s1.

[114] S.R. Klein. IceCube: A Cubic Kilometer Radiation Detector. *IEEE Transactions on Nuclear Science*, 56(3):1141–1147, 2009. URL http://ieeexplore.ieee.org/stamp/stamp.jsp?tp=&arnumber=5076089.

[115] R. Abbasi *et al.* IceTop: The surface component of IceCube. *Nuclear Instruments and Methods in Physics Research A*, 700:188–220, 2013.

[116] R. Abbasi *et al.* Measurement of the Anisotropy of Cosmic-Ray Arrival Directions With IceCube. *The Astrophysical Journal Letters*, 718(2):L194–L198, 2010. URL http://ieeexplore.ieee.org/stamp/stamp.jsp?tp=&arnumber=5076089.

[117] R. Abbasi *et al.* Calibration and Characterization of the IceCube Photomultiplier Tube. *Instrumentation and Methods for Astrophysics*, 618(2):139–152, 2010. URL http://arxiv.org/pdf/1002.2442v1.pdf.

[118] M. Abramowitz and Davidson M.W. Concepts in Digital Imaging Technology: Photomultiplier Tubes. URL http://learn.hamamatsu.com/articles/photomultipliers.html. Visited on 2013-05-26.

[119] R. Gilmore. *Single Particle Detection and Measurement*. Taylor & Francis, London, 1992.

[120] Electron Tubes Ltd. *Photomultipliers and Accessories*. 1996.

[121] R7081-02 Hamamatsu: data sheet. URL http://icecube.wisc.edu/~kitamura/NK/PMT/031112%20R7081-02%20data%20sheet.pdf. Visited on 2013-06-11.

[122] B. Herold *et al.* Characterisation of PMTs for KM3NeT. *Proceedings of the 31st ICRC*, 2009. URL http://icrc2009.uni.lodz.pl/proc/pdf/icrc0596.pdf.

[123] S. Böser *et al.* Introducing WOM: A Wavelength-shifting Optical Module. *Unpublished*, 2012.

[124] G.F. Knoll. *Radiation Detection and Measurement, 3rd edition*. John Wiley & Sons, Inc. New York, 2000.

[125] J.B. Birks. *Proceedings of the Physical Societies A*, 64:874–877, 1951.

[126] S.E. Derenzo. Scintillation counters, Photodetectors and Radiation Spectroscopy. *IEEE Short Course Radiation. Detection and Measurement, Nuclear Science Symposium*, 1997.

[127] D. Szam. Plastic Scintillators Production, 2013. URL http://www.ihep.ru/scint/bulk/product-e.htm. Visited on 2013-06-06.

[128] Photonis. Photonis PMTs. URL http://particle.korea.ac.kr/lab/cata$_$basic.pdf. Visited on 2013-06-06.

[129] Saint-Gobain Crystals. Scintillating Optical Fibers, . URL http://www.detectors.saint-gobain.com/uploadedFiles/SGdetectors/Documents/Brochures/Scintillating-Optical-Fibers-Brochure.pdf. Visited on 2013-06-06.

[130] Saint-Gobain Crystals. BC482-A and BC-484 Wavelength Shifting Bars, . URL http://www.detectors.saint-gobain.com/uploadedFiles/SGdetectors/Documents/Product_Data_Sheets/BC482A-484-Data-Sheet.pdf. Visited on 2013-06-06.

[131] CAEN MOD SY527 Technical Information Manual. URL http://rnc.lbl.gov/~jhthomas/public/SSD/caensy527.pdf. Visited on 2012-13-02.

[132] CAEN MOD V1718 Technical Information Manual. URL http://www.tunl.duke.edu/documents/public/electronics/CAEN/caen_v1718.pdf. Visited on 2012-13-02.

[133] CAEN MOD V792 Technical Information Manual. URL http://www-w2k.gsi.de/frs/technical/electronics/vme-manuals/v792_rev7.pdf. Visited on 2012-13-02.

[134] CAEN MOD V812 Technical Information Manual. URL http://www.cord.edu/dept/physics/mona/manuals/V812.pdf. Visited on 2012-13-02.

[135] CO4020 Quad 4-Input Logic Unit EG&G ORTEC. URL http://fy.chalmers.se/subatom/f2bmm/aep/CO4020.pdf. Visited on 2012-13-02.

[136] Quad 200-MHz Constant-Fraction Discriminator EG&G ORTEC. URL http://photon-science.desy.de/sites/site_photonscience/content/e62/e190204/e190208/e190212/e190216/e190217/infoboxContent190225/NIM-935_eng.pdf. Visited on 2012-13-02.

[137] Roithner LaserTechnik. STAR405F5, 2013. URL http://www.roithner-laser.com/datasheets/lasermodules/405/star405f5.pdf. Visited on 2013-04-06.

[138] Präzisions Glas & Optik, 2013. URL http://www.pgo-online.com/. Visited on 2013-04-05.

[139] M. Polyanskiy. Refractive Index Database, 2008–2012. URL http://refractiveindex.info/. Visited on 2012-12-05.